Magnetic Spectroscopy with Scintillation Detectors at the LUXE Experiment

John Andrew Hallford

for University College London (UCL)

June 2023

Submitted in accordance with requirements for the award of the degree of
Doctor of Philosophy

Abstract

The success of the physical model of quantum electrodynamics relies on the use of a small perturbation above a quantum vacuum solution. In the physically possible case of a strong electric field, defined as being near or greater than the Schwinger limit, the assumption underlying this perturbation theory approach becomes unviable. In this new regime lies unexplored phenomena and a chance at new physics.

The upcoming LUXE experiment at the Deutsches Elektronen-Synchrotron intends to reach new parameter-space for intensity of an electric field, and access the strong regime. This is performed in two modes, with a modern high-power laser firing intense pulses at either accelerated bunches of electrons from the EU.XFEL (e-laser mode), or high-energy photons produced from the same EU.XFEL electron bunches (γ-laser mode). This thesis includes analysis of high-energy Bremsstrahlung emission, with the goal of accurately describing the flux of high-energy photons within the interaction point at LUXE.

Presented here is the design and performance of operation of a magnetic spectrometer system, used to reconstruct the energy distributions of a flux of electrons, using a screen of scintillating material and optical cameras. This includes results from both simulation and using a prototype within test-beam.

The Bremsstrahlung-related test-beam measurement resulted in a reconstructed polar angle profile which gives a reduction of maximum photon flux of 63% compared to the accepted model, if one assumes all measured discrepancy is due to inaccuracy in the theory.

The suitability of the scintillator screen & camera system for LUXE is proven, in particular as the reconstruction of energy to $\pm 2\%$ on a

single-shot-basis is shown in simulation. The signal to noise ratio and dynamic range of the system, measured in test-beam, were included in the simulation.

Declaration

I, John Andrew Hallford, confirm that the work presented in my thesis is my own. Where information has been derived from other sources, I confirm that this has been indicated in the thesis.

[SIGNATURE REDACTED]

John Andrew Hallford

November 3, 2023

Impact Statement

Fundamental physics research has historically created some of the most transformative technologies the world has ever known. From the theory of the atom, the electron, and electromagnetism giving us the electrical-circuit-powered world we live in today, to particle accelerators used within medical treatment and diagnostic devices, to the almost incidental invention of the world-wide-web by CERN, even the most fundamental of research developments can quickly result in hugely beneficial technologies.

At LUXE the opportunity to make measurements into new parameter-space with superior statistical significance is present, giving a rare test of an edge case of the most fundamental theory of particle physics.

The majority of the work presented in this thesis represents the development of a detector for the experiment, namely the scintillation screen and camera system, intended for measurement of the energy spectra of electrons. Moreover, the work presented in this thesis is almost all the work completed in preparing this detector; that is to say, without this project the detector would not and will not be used in LUXE. The detector developed then provides a detailed blueprint for the use of similar detectors in experiments exhibiting similar requirements in the form of the energy reconstruction of intense fluxes of electrons.

LUXE aims to complete the highest-quality measurements yet of physics approaching the strong regime, which then has an impact of our understanding of phenomena in various other contexts. Strong magnetic fields are expected in interstellar objects such as magnetars, and strong electric fields will be created in the interaction points of any future high-energy lepton colliders; the phenomena of both must be understood. Looking into the nature of strong electric fields can also inform us indirectly of the

underlying mechanisms of strong fields in other contexts – most notably in the strong force, which is divergent at low energy scales.

Acknowledgements

First and foremost I should thank Matthew Wing for his mentorship, guidance, and patience through the last three-and-a-bit years. I also need to express gratitude to my LUXE colleagues at DESY, and I can confidently say this work and I myself have benefited from their expertise.

No small measure of my sanity was kept by sampling the various Hamburger restaurants at Friday Night Dinners with the DESY FTX students – so I have to thank them all, though there are too many to name (ok, just one, special thanks to Dasha).

I was particularly glad for to be part of a wholesome group of students of the same year at UCL HEP, (are we the fourth-order corrections now?) who helped settle me in. Thank you all. I benefited also from the support and advice from my family, including actually hosting me while I worked on the PhD remotely. Thanks to you all!

Contents

List of figures

List of tables

"Everyone now knows how to find the meaning of life within himself. But mankind wasn't always so lucky."

— Kurt Vonnegut, *The Sirens of Titan*

Chapter 1.

Introduction

Finding the breaking points of otherwise successful theories provides some of the best access to new phenomena, thereby better illuminating the deeper mysteries of the universe. The most successful way to push the Standard Model (SM) since its creation has been the energy frontier. This has allowed the discovery of many crucial elements, typically in the form of a new particle. Each successive particle forms an addition to the Standard Model of particle physics. The SM started with the model of quantum electrodynamics (QED), which governs electromagnetic interactions between charged particles, mediated by the photon.

Quantum electrodynamics' predictions have been tested to the point it can be called one of the most quantitatively accurate theories in the history of science. Yet the theory becomes divergent, that is to say observable quantities are incalculable, at high energy scales or in intense low-energy photon backgrounds. Experiments looking into this high-intensity regime not explained by our best theories, including QED, can offer the best chance of radical changes in our understanding of the universe.

The field of research of particle interactions in such extreme electric fields, strong-field quantum electrodynamics (SFQED), uses key assumptions to subvert some of the divergences of QED. LUXE is an experiment in development which intends to make an observation of phenomena resulting from processes in such a field. In LUXE a strong electric field will be created by inducing an intense low-energy photon background by colliding a high-energy electron beam with an intense laser pulse. The measurement comes in the form of analysis of the energy distributions and general production rates of particles interacting in the strong field.

Thesis Outline

This thesis, as is common in high-energy-physics experiments, represents some portion of a large collaborative effort between multiple researchers from multiple institutes. Summaries of each chapter and the respective elements of this thesis which represent work done by the author are indicated chapter-by-chapter below.

- Chapter 2 elucidates the theoretical background of strong-field QED as far as is relevant for the LUXE experiment, including brief descriptions of goals (and results, where relevant) of past, present and prospective strong-field QED experiments.
- Chapter 3 gives an overview of the LUXE experiment. The main contribution from the author to the LUXE experiment pertains to the scintillator & camera detector system, which is instead described in detail in Chapters 5, 6 & 7. The implementation of the Cherenkov detector within a GEANT4 simulation, described in this chapter, was completed by the author.
- Chapter 4 is the description of a test-beam experiment designed to measure the divergence of a photon beam generated via Bremsstrahlung. The design of the test-beam and its organisation was done by collaborators. The author contributed in the group effort of gathering of the data, and is responsible for the analysis presented.
- Chapter 5 is a description of the design of the scintillator screen & camera system. All of the material within this chapter and every chapter hereafter was produced by the author (excepting figures obtained from sources duly referenced). Some of the written content is shared with the relevant scintillation screen & camera detector section within published Ref. [1]. A great deal of this content will also be found in a scintillator screen & camera chapter within the LUXE Technical Design Report to be published in the future.
- Chapter 6 describes the creation of a reconstruction algorithm, a simulation / emulation of the scintillator screen & camera system, and the application of the reconstruction algorithm to simulation results. Analysis is made of the reconstructed electron energy spectra, including with respect to a particular kinematic feature, the Compton edge. A finite-impulse-response filter technique is applied to optimise results in a low-statistics case. Again a significant fraction of this content will be found in the LUXE Technical Design Report, soon to be published.

- Chapter 7 describes the setup and analysis of the assembled scintillator screen & camera system in a test-beam experiment, and recover an approximate calibration of the detector, which is applied to simulation. Much of the content in this chapter will also be found in the to-be-published LUXE Technical Design Report.
- Chapter 8, the conclusion, gives meditations on the work performed in the light of the upcoming full LUXE experiment.

Thereafter are three appendices which detail organisational details of the scintillator screen & camera system. They are not deemed to be interesting enough physics-wise to be included in the main text but are included for posterity and completeness.

Chapter 2.

Strong-Field Quantum Electrodynamics

2.1. Quantum Electrodynamics

Ever since its creation in the early 20^{th} century, Quantum Electrodynamics (QED) has proven to be one of the most quantitatively accurate theories in the history of physics. This is best exemplified in the measurement of the anomalous magnetic moment of the electron (and contained within, the fine-structure constant α). While the measurement of the same quantity of the muon has some discrepancy with respect to the Standard Model (SM) expectation [2], the electron's g-2 value has agreement between theory and experiment down to 0.56 parts in 1 trillion [3, 4]. QED forms one part of the wider Standard Model, in combination with the weak interaction, and the two are unified at higher energies in the electro-weak interaction. QED is the first discovered, best understood, and best-tested sector of the SM [5].

Referred to as "the jewel of physics" by Richard Feynman [6], QED has generally produced extremely accurate results; this is despite a number of approximations and assumptions in the long process of using the underlying theory to calculate any observable quantities. An example of a quick calculation, with the aim of finding a cross-section of some interaction, will be elucidated below. In particular we choose the Compton scattering process.

The Lagrangian for QED using natural units is defined as:

$$\mathcal{L} = \overline{\psi}(x)(i\partial\!\!\!/ - eA\!\!\!/ - m)\psi(x) - \frac{1}{4}F_{\mu\nu}F^{\mu\nu} \tag{2.1}$$

with the electromagnetic field A_μ contributing to:

$$F_{\mu\nu} = \partial_\mu A_\nu - \partial_\nu A_\mu \tag{2.2}$$

employing the Feynman slash notation $A\!\!\!/ = \gamma^\mu A_\mu$ with γ^μ the Dirac matrices. The values e and m represent the electric charge and mass of the electron. The solutions to the equation $\psi(\overline{\psi})$ are Dirac bispinors representing lepton fields. To calculate a cross-section of a scattering process (two incoming particles and two outgoing particles), the centre-of-mass form of σ may be used:

$$\begin{aligned}\sigma = \frac{1}{2E_p E_k |v_p - v_k|} \int |\mathcal{M}|^2 (2\pi)^4 \prod_{i=1}^{n} \frac{d^3 p_i}{(2\pi^3) 2E_i} \\ \times \delta\left(\sum_{i=1}^{n} E_i - E\right) \delta^3\left(\sum_{i=1}^{n} p_i - p\right)\end{aligned} \tag{2.3}$$

The energies, velocities and momenta of the incident particles are labelled E_p & E_k, v_p & v_k, and p_p & p_k respectively. The sums over index i are summing over each particle in the final state; the δ function denotes the Dirac-delta function. We can overlook the kinematics details here; the important part for this demonstration is that the cross-section, and so the interaction probability, depends on the square of the matrix element $|\mathcal{M}|^2$. Significantly speeding up our progress, we may analyse the matrix element for some interaction using the well-established Feynman rules [5] associated with Feynman diagrams; these rules are derived ultimately from the QED Lagrangian in Equation 2.1. For simplicity we can focus on the s-channel process shown in Figure 2.1.

Examining the Feynman rules, the matrix element can be calculated:

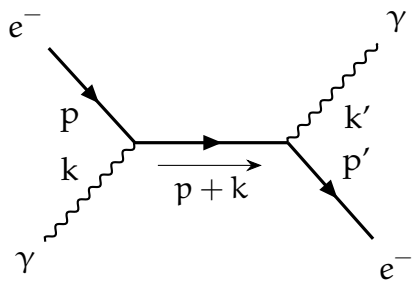

Figure 2.1.: The s-channel tree-level case of Compton scattering. Time progresses from left to right.

$$\begin{aligned}\mathcal{M} &= i\overline{u}(p)(ig_e\gamma^\mu)\epsilon^*_\mu(k)\frac{i(\not{p}+\not{k}+m)}{(p+k)^2-m^2+i\epsilon}(ig_e\gamma^\nu)\epsilon_\nu(k')u(p') \\ &= 4\pi\alpha\ \times\ \overline{u}(p)\gamma^\mu\epsilon^*_\mu(k)\frac{i(\not{p}+\not{k}+m)}{(p+k)^2-m^2}\gamma^\nu\epsilon_\nu(k')u(p')\end{aligned} \tag{2.4}$$

where $\overline{u}(p)$, $u(p')$ and $\epsilon^*_\mu(k)$, $\epsilon_\nu(k')$ are spinor and polarisation vectors for the electron and photon respectively. The initial and final state of each is noted by the momentum labels shown in Figure 2.1. Observe the fact that each vertex carries with it a factor of $ig_e\gamma^\mu$, where $g_e = \sqrt{4\pi\alpha}$, ultimately meaning the total diagram produces an α pre-factor. The ultimate cross-section is proportional to the absolute square of the matrix element as per Equation 2.3, and so:

$$\sigma \propto |\mathcal{M}|^2 \propto \alpha^2 \tag{2.5}$$

Each of the symmetric s,u-channel variants of diagram 2.1, since they carry the same number of vertices, have the same dependence on α^2. They each represent a tree-level diagram, and so it is important to realise that there exists more complex diagrams which produce the same initial and final states. Each of these further processes must be included, but they necessarily require more and more vertices attached.

One example is in Figure 2.2, where a completely internal photon propagator appears. This interaction, after applying the Feynman rules, produces the result below (simplifying uninteresting terms for our demonstration):

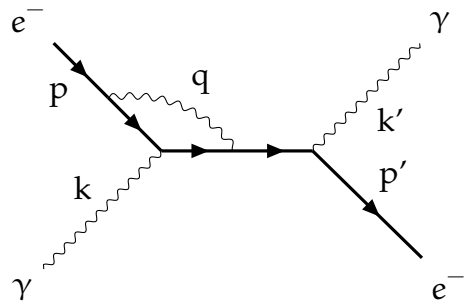

Figure 2.2.: A next-to-leading-order Feynman diagram of Compton scattering.

$$\begin{aligned}\mathcal{M} &= i\int \frac{d^4q}{(2\pi)^4}\,\overline{u}(p)(ig_e\gamma^\mu)\epsilon^*_\mu(k)(ig_e\gamma^\xi)\times\text{momenta terms}\times(ig_e\gamma^\chi)\epsilon_\nu(k')u(p')\\ &= 16\pi^2\alpha^2\int \frac{d^4q}{(2\pi)^4}\,\overline{u}(p)\gamma^\mu\epsilon^*_\mu(k)\times\text{momenta terms}\times\gamma^\nu\epsilon_\nu(k')u(p')\end{aligned} \tag{2.6}$$

With the increasing number of vertices, the factor of α is maintained and increases in power. There are naturally far more variations of the diagram with two added vertices, and so more terms of this order appear, compared to the leading order (minimal number vertices). We can generalise Equation 2.5 into a form below, where for leading-order interactions $n = 1$, for next-to-leading-order $n = 2$, and so on:

$$\sigma_n \propto |\mathcal{M}_n|^2 \propto \alpha^{2n} \tag{2.7}$$

This is a product of the fact that fundamentally QED applies perturbation theory, which uses an infinite series of terms to approximate the description of a particle system by adding a small perturbation to a known solution – in this case the no-interaction quantum vacuum state. The perturbation is expressed pictorially in Feynman diagrams with progressively more complex diagrams including more and more vertices which are (usually) increasingly unlikely; mathematically, they come to represent terms in the matrix element with the coupling constant(s) at higher and higher powers. Crucial to the convergence of the calculation is that the fine-structure constant α

is smaller than unity, and so these higher order terms become successively smaller. Fortunately for the theory of QED, this is true as $\alpha \approx 1/137$.

Yet this constant we know is not actually (effectively) constant. In the case of extremely energetic interactions, the charge-screening effect is reduced. The electron at low energy scales can be understood as a point-like charge surrounded by a cloud of virtual particle pairs, being produced and annihilated continuously, therefore limiting the 'bare' charge within. In high-energy – and therefore spatially-fine – contexts, the screening is probed deeper, the charge appears increased, and so a coupling constant which runs with increasing energy-scale is discovered, with an asymptote at probe-distance of zero. There is experimental evidence for this effect [7] and it is calculated to produce an effective $\alpha = 1/127$ at the 90 GeV (mass of Z boson) energy-scale.

As the coupling runs, more and more terms in the perturbative expansion must be included to make an accurate calculation, until the point that it reaches unity, at which point the sum is strictly divergent and the theory breaks down. The scale of energy at which this happens in QED, known as the Landau pole, lies at around 10^{286} eV; so there is no prospect of observing this in man-made or natural contexts[1].

But while reaching a point of the coupling being unity – i.e. a transition into the strong-field regime – through high-energy interactions is not possible, a magnified effective coupling can be induced in another way. In a low-energy but high-intensity photon background, for example with a probe electron, many small interactions with these low-energy photons can be summed into one effective vertex. As it represents many possible interactions there comes an effective coupling proportional to both the elementary charge (or fine-structure constant), but also the intensity of the background photons. The *effective* QED coupling is then inflated, and should it grow large enough terms in the expansion which are dependent on α must be included at all orders.

The point at which non-linearity starts to be seen, the Schwinger limit[2], is typically expressed in conventional electric or magnetic field strength: $1.32 \times 10^{18}\,\mathrm{Vm}^{-1}$ and $4.4 \times 10^{9}\,\mathrm{T}$ respectively. This is defined as the field strength required to deliver the equivalent energy of one electron's mass to a particle of elementary charge, over the reduced Compton wavelength of the electron ($\lambda_{\mathrm{Compt.}} = \hbar/m_e c$), which itself comes from the Heisenberg energy uncertainty relation . This gives $\mathcal{E}_{\mathrm{Schw.}} = m_e^2 c^3/e\hbar$ where

[1] Assuming a synchrotron with the beam and acceleration power of the Large Hadron Collider, to simply overcome losses from synchrotron radiation, a circular accelerator which reaches this energy would need to be 10^{522} times larger than the observable universe.

[2] So named despite being initially calculated by Sauter in 1931 [8].

m_e, e are the mass and charge of the electron respectively; c and $\hbar$ have their usual meanings. For clarity we use $\mathcal{E}$ to represent electric field magnitude and E for energy. The virtual electron-positron pairs which are continuously being produced and which self-annihilate in free space can then be pulled into reality, resulting in spontaneous electron-positron pair production in a process similar to Hawking radiation, around such high intensities of electromagnetic field[3].

Perturbative QED at this electric field scale no longer functions, and so a modified theory is needed. This is fortunately indeed possible, with some key assumptions in the electric field background needed; this is discussed in the next section.

2.2. Strong-Field QED

Instead of the typical treatment in QED, modelling the interactions between two or more quantised particles, one may instead model interactions of particles exclusively with an underlying field, when this field is composed of high-intensity low-energy photons. In this case, although the sum of the perturbative expansion is not strictly convergent, the Born approximation can be used [10], which is valid when a scattered 'field' is small compared to its scattering counterpart. This forms a method of calculating expectations for the cross-sections, energy and momentum distributions where the QED perturbative approach is not possible - with appropriate uncertainties due to the approximations and uncertainties in the model.

In the context of an intense field, the plane wave model may be used. With two key approximations, modelling the strong field as a plane wave provides calculable solutions for interactions with a probe particle. The requirements are: the intense background is unaffected and constant under the interaction of some low-energy photons with a probe particle; and the probe particle is highly relativistic. The known solution to the Dirac equation in a classical field is the Volkov solution [11]. This basis can be used to generate numerical simulations of Strong-Field QED (SFQED) processes, particularly of monochromatic fields larger than the scattering particle.

For the discussions following the definition of some parameters will be useful. Intense electric fields can be created from focussed laser light. A useful parameter to

[3] The purely magnetic case cannot produce the characteristic spontaneous pair production; instead this corresponds to the Landau electron level equal to the electron rest mass [9].

define when describing this is the dimensionless field magnitude parameter ξ. For an example of an electric field of sufficient magnitude $\mathcal{E}_L$ due to a laser of monochromatic light:

$$\xi = \frac{e\mathcal{E}_L}{\omega_L m_e c} = \frac{\mathcal{E}_L m_e c^2}{\mathcal{E}_{\text{Schw.}} \hbar \omega_L} \tag{2.8}$$

or $m_e \mathcal{E}_L / \omega_L \mathcal{E}_{\text{Schw.}}$, in natural units, where ω_L denotes the frequency of the laser light. Alternatively and complementarily one can construct a 'quantum' parameter describing the effects of, for example, an electron with gamma factor γ_e intercepting the laser spot:

$$\chi = 2\gamma_e \frac{\hbar \omega_L}{m_e c^2} \xi = 2\gamma_e \frac{\mathcal{E}_L}{\mathcal{E}_{\text{Schw.}}} = \frac{\mathcal{E}_*}{\mathcal{E}_{\text{Schw.}}} \tag{2.9}$$

where $\mathcal{E}_*$ is the enhanced field experienced in the rest frame of the massive probe particle. One can use an alternative definition $\chi_\gamma = 2E_\gamma \mathcal{E}_L / m_e c^2 \mathcal{E}_{\text{Schw.}}$ for the massless case, where E_γ is the energy of a probe photon. This parameter can be understood as the effect of the length contraction, and therefore magnitude amplification, of the electric field in the direction of travel of the particle / laser pulse – assuming a head-on collision. Since this is a relativistic effect there is no effective field magnification for particles moving orthogonal to the laser.

From the SFQED model, and the interaction rules of the Standard Model, we can examine some interactions and phenomena expected in intense electric fields. Among them are vacuum birefringence, where an ellipticity is seen in photons which pass through intense electric fields [12]. More relevant for this work are two specific interactions between a single particle 'scattering' off the background field: non-linear (inverse) Compton scattering and the multiphoton Breit-Wheeler process[4]. The diagrams of these are shown in Figure 2.3a & 2.3b (respectively). These two interactions are detailed in the next two subsections. The diagrams can be combined with one immediately succeeding the other, as shown in Figure 2.3c; this 'trident' process becomes part of a 'cascade' of QED interactions in sufficiently large and intense electric fields. In general, for equivalent ξ/χ parameter, the non-linear Compton process is much more probable to occur than pair production through the multiphoton Breit-Wheeler interaction.

[4] This is so called 'multiphoton' for differentiation against the 'pure' Breit-Wheeler process, where only two high-energy photons combine; this name is consistently used even, as shown later, the fields reached leave the 'multiphoton' regime and enter a non-linear regime.

Strong-field QED is not just a quirk of the theoretical world; such fields are expected to appear in nature and in future man-made scientific environments. Some real-world applications of the theory are:

- Future lepton colliders, such as the International Linear Collider or Future Circular Collider, will create short-lived strong electric fields and will need to be able to account for the phenomena observed due to this [13, 14].
- Understanding astrophysical objects such as magnetars which are expected to have intense magnetic fields far in excess of the critical field [15].
- In plasma physics, especially with the accompanied stimulation by intense lasers, extremely intense fields will be produced with the possibility of a stream of particles produced from a cascade of the interactions explained below [16].
- Within studies of the nuclei of atoms with high atomic numbers ($Z > 137$), strong electric fields are expected [17].
- Investigation into the true nature of strong fields in QED also gives valuable insight into how strong fields operate in other contexts, most notably the pertinently named strong force.

2.2.1. Non-Linear Compton Scattering

Non-linear Compton scattering is the radiation of one real photon by an electron in a strong electric field. The cross-section of the first-order interaction can be estimated by modifying the known Thomson scattering cross-section [18]. It is written so:

$$\sigma_{\text{Compton}} = \sigma_{\text{Thomson}}(1 - 2\eta - (2/5)\,\xi^2 + (14/5)\,\eta\xi^2 + ...) \tag{2.10}$$

and so the scattering rate is amplified with higher ξ. η is a dimensionless energy parameter associated with the initial probe particle, equivalent to:

$$\eta = (\hbar\omega_L E_e/m_e^2c^4)(1 + \beta\cos(\theta)) \tag{2.11}$$

where E_e is the probe electron energy, β is the electron velocity, and θ the angle between the particle and plane wave propagation. But an increase in total scattering

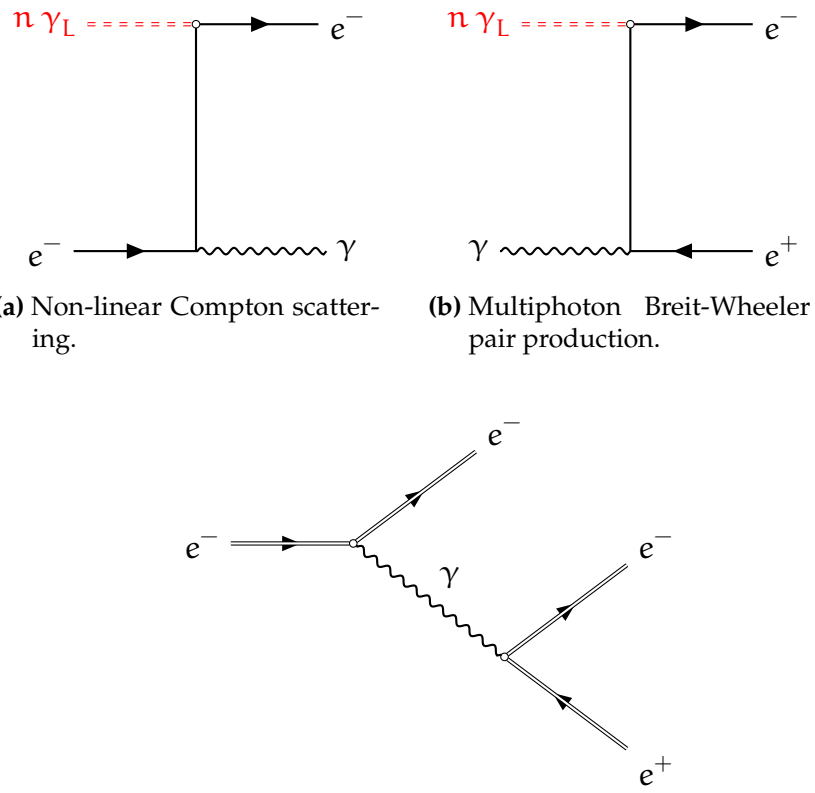

(a) Non-linear Compton scattering.

(b) Multiphoton Breit-Wheeler pair production.

(c) A trident process, essentially formed of the two diagrams above.

Figure 2.3.: Feynman diagrams of simple interactions possible for photons or electrons in a strong electric field. **(a)** and **(b)** show a red propagator, representing a number n of laser photons interacting with the charged particle(s). This is represented in an alternative fashion in diagram **(c)**, where the double-barrelled lines present 'laser-dressed' fermions.

is not the only non-linear effect changing ξ has upon the interaction. The differential cross-section of a non-linear Compton interaction of order n can be calculated [19,20] to be :

$$\frac{d\sigma_n}{dx} = 2\pi r_0^2 \frac{m_e^2}{s - m_e^2} \frac{1}{(1+x)^2} \sum_{n=1}^{\infty} \left[-\frac{4}{\xi^2} J_n^2(z_x) + \left(2 + \frac{x^2}{1+x}\right) \left(J_{n+1}^2(z_x) + J_{n-1}^2(z_x) - 2J_n^2(z_x)\right) \right] \tag{2.12}$$

where n denotes the number of incident laser photons participating in the interaction as per Figure 2.3a. This is derived in the case of circularly polarised laser photon background; r_0 is the classical electron radius defined as $e^2/(4\pi m_e \epsilon_0 c^2)$ and s denotes

the Mandelstam parameter, equal to the square of the total relativistic energy of all incident particles taking part in the interaction. The x parameter is a dimensionless Lorentz-invariant energy parameter, which can be effectively read as a fraction of the initial total energy carried by the emitted photon. The argument of the Bessel functions (J_n), z_x, is defined as:

$$z_x \equiv \frac{m_e^2 \xi \sqrt{1+\xi^2}}{k \cdot p} [x(x_n - x)]^{1/2}, \quad x_n \equiv \frac{2n(k \cdot p)}{m_e^2(1+\xi^2)} \tag{2.13}$$

for initial laser photon, electron momenta k, p. The denominator in the definition of x_n can be interpreted as (the square of) an effective mass: $m_* = m_e\sqrt{1+\xi^2}$. Therefore x_n represents the limit in the spectrum kinematically allowed for a given order n, the number of laser photons in the interaction. This forms a kinematic edge in the emitted photon energy spectrum, which transforms (shrinks) with increasing ξ. This is described in linear QED, with lightfront momentum parameter x, for some order of interaction n, thus:

$$x_n = \frac{2n\eta}{2n\eta + 1} \tag{2.14}$$

The non-linear approach to modelling the Compton edge in non-linear Compton scattering within a SFQED background is instead described as:

$$x_n = \frac{2n\eta}{2n\eta + 1 + \xi^2} \tag{2.15}$$

The edge position in the photon energy spectrum then transitions between two limits for ξ approaching 0 and ∞: at low ξ, this is the linear case given in Equation 2.14. For high ξ it approaches zero.

2.2.2. Multiphoton Breit-Wheeler

The spontaneous 'boiling of the vacuum' in the background of a plane-wave laser manifests in the form of the 'multiphoton' Breit-Wheeler interaction. A photon within

the field will often produce virtual electron-positron pairs which will then absorb multiple photons. Should the absorbed photons impart enough energy upon the lepton pair, they can become real, and so the initial photon is quite spontaneously decayed to the pair.

Within the low-ξ region of parameter-space ($\xi^2 \ll 1$), the probability of a spontaneous Breit-Wheeler process is small but not zero. It can be solved with typical perturbative QED [21], returning a rate (per unit volume) of the form:

$$\Gamma = \frac{(e\mathcal{E})^2}{4\pi^3\hbar^2 c} \sum_{n=1}^{\infty} (1/n^2) exp(-\pi^2 c^3 n/\hbar e\mathcal{E}) \tag{2.16}$$

and one can otherwise show the rate, or generally probability P, to depend on the parameter ξ:

$$P \propto \xi^{2n_*} \tag{2.17}$$

where n_* denotes the minimum number of photons to create a pair from rest: $n_* = 2(1+\xi^2)/\eta$. We can refer to this as the linear regime.

For the case where $\xi \gg 1$ & $\chi_\gamma \sim 1$, the probability evolves [22]:

$$P \propto \chi_\gamma exp(-8/(3\chi_\gamma)) \tag{2.18}$$

using the quantum χ_γ parameter of the incident photon. This solution requires use of the SFQED semi-classical models previously outlined. This expected high-ξ probability has not yet been experimentally measured, nor has the transition between the linear regime result 2.17 to the SFQED expectation 2.18. One can describe the process of pair-creation around this value of $\chi \sim 1$, or equivalently $\mathcal{E}_* \sim \mathcal{E}_{Schw.}$, as virtual pairs breaching a potential barrier, with assistance from the field, into reality. As a result we may call this 'tunnelling' pair creation behaviour. This is in contrast to the linear regime previously defined, and the higher-χ ($\chi \gg 1$) regime, which may be referred to as the complete non-perturbative regime. In this complete non-perturbative regime, it can be proven that the probability of the non-linear Breit-Wheeler probability is:

$$P \propto \chi_\gamma^{2/3} \tag{2.19}$$

From Ref. [23], we see that the effective coupling itself in this regime is $\alpha\chi_\gamma^{2/3}$ and so at $\chi_\gamma^{2/3} > \alpha^{-1} \sim 137$ the perturbative approach is fully divergent.

With the symmetry present in this interaction, the energy distribution of the final electron is equal to that of the positron. This distribution is a Gaussian-like peak, symmetrical around half of the incident photon energy. The single-interaction leptons in a pair are not generally of equal energy. The symmetry between electrons and positrons means they share an energy profile, the width of which increases with ξ.

2.3. The State of the Field

Investigation into light-light interactions through collisions at high-energy colliders have been performed. Measurements of light-light scattering and the diphoton Breit-Wheeler interaction have been made at the Large Hadron Collider and Relativistic Heavy-Ion Collider [24–26].

But the experiments which most directly test SFQED are those which use lasers to generate their intense fields, and the most relevant of those are presented in the following subsections. A clear advantage of using a laser is the ability to directly observe and control the magnitude of the intensity and therefore effective coupling constant, then observe the interaction characteristics in a clean environment.

2.3.1. The E144 Experiment

Strong-field Quantum Electrodynamics was perhaps most famously tested in the E144 experiment [27] conducted at the Stanford Linear Accelerator Center (SLAC). This experiment, conducted in the late 1990s, collided the high-energy electron beam at SLAC with intense laser pulses. Within these intense neodynium-glass laser pulses an intensity of $\approx 0.5 \times 10^{18}\,\mathrm{Wcm}^{-2}$ was achieved, or a ξ value of 0.4. The electron beam, operating at energies between 46.6 - 49.1 GeV, then induced a χ parameter of around 0.27. This represents a value of the assisted field (experienced by the beam)

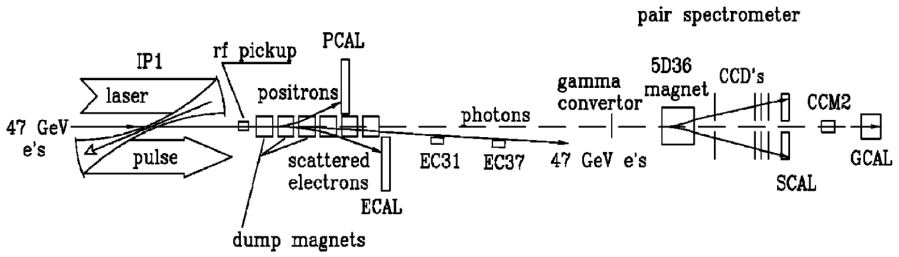

Figure 2.4.: A schematic of the E144 experiment performed at SLAC. Published in [27].

below the Schwinger value, yet close enough to make possible the observation of the multiphoton Breit-Wheeler process.

Figure 2.4 shows the layout of the experiment. Briefly, the emerging electron beam from the left interacts with the intense laser field and the resultant outgoing particles are separated by charge with a magnetic field before being detected with an array of detectors. The Positron and Electron Calorimeters (PCAL and ECAL) measured the energy spectrum of the positrons and scattered electrons respectively. For some fraction of the running time, a foil of heavy metal was used to convert high-energy photons to electron-positron pairs, which were reconstructed in energy using CCD pixel detectors and another magnetic field. With this setup E144 reconstructed the rates and the energies of the three particle types expected; namely, electrons positrons and photons. Photons were generated from the non-linear Compton process; the positrons are created only through the trident process, where a non-linear Compton emission is quickly followed by the multiphoton Breit-Wheeler interaction.

The results showed a new step into a new regime, including the identification of positrons created from 'light-light' scattering. The total number of these positrons identified from the multiphoton Breit-Wheeler process was 106 ± 14 after subtraction of background. The rate of positrons detected per electron-laser crossing is plotted with respect to the laser intensity parameter, in addition to a 95% confidence level limit on stochastic background imitating positron signal, in Figure 2.5. The data are fit with a power-law function, suiting the low-ξ trend of $P \propto \xi^{2n_*}$, and the function fits well. Holistically, and with reference to the maximum ξ achieved, it can be said that E144 successfully measured the multiphoton Breit-Wheeler process for the first time, though only within the low-ξ, power-law regime.

Analysis was performed of the non-linear Compton scattering process too. This came in the form of reconstruction of both the electron and photon spectra generated,

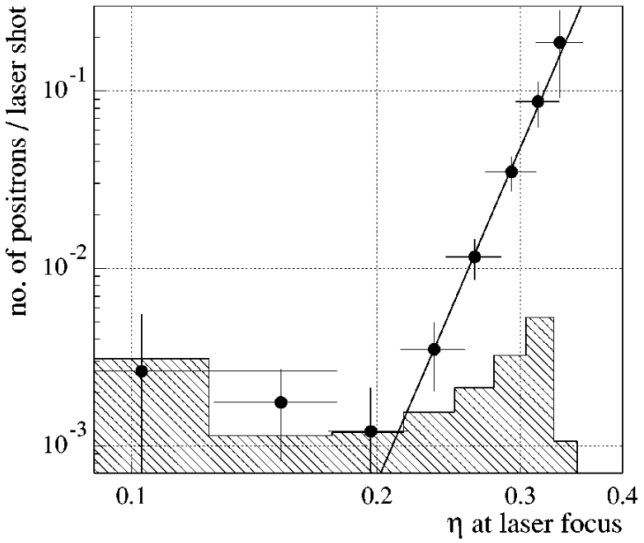

Figure 2.5.: Results for the measured rates of positrons from the multiphoton Breit-Wheeler process, shown with respect to the intensity of the laser focus, as measured by the E144 experiment [27]. The shaded regions represent the 95% confidence level limit on background imitating the positron signal. The η symbol is the unitless intensity parameter, defined as ξ, throughout the rest of this document and LUXE literature.

and measured with the array of detectors present in Figure 2.4. The reconstructions of the rate of non-linear Compton scattering, or specifically the rate at a specific point in the energy spectrum, normalised to the expected number of laser photons, are shown in Figure 2.6. This normalisation proves that, since the rates do not remain static through changing laser intensity, the interaction is not linear. Alongside is the expectation from a SFQED simulation. Note that this figure compares the rates for points in the energy spectrum for varying ξ; in Figure 2.7, one can see the actual measured distributions through energy. Each sub-plot shows the spectrum measured for a different value of ξ, which is denoted as η in the literature produced by E144.

2.3.2. The E320 Experiment

The current generation of SFQED experiment at SLAC, the E320 experiment [28], is currently running and acquiring data. The collaboration has successfully started colliding high-energy electrons with laser pulses – analyses of their results are expected in the near future [29]. The principle of the experiment is similar to that shown in E144, in that a focussed laser pulse is intercepted with GeV-energy electrons at an

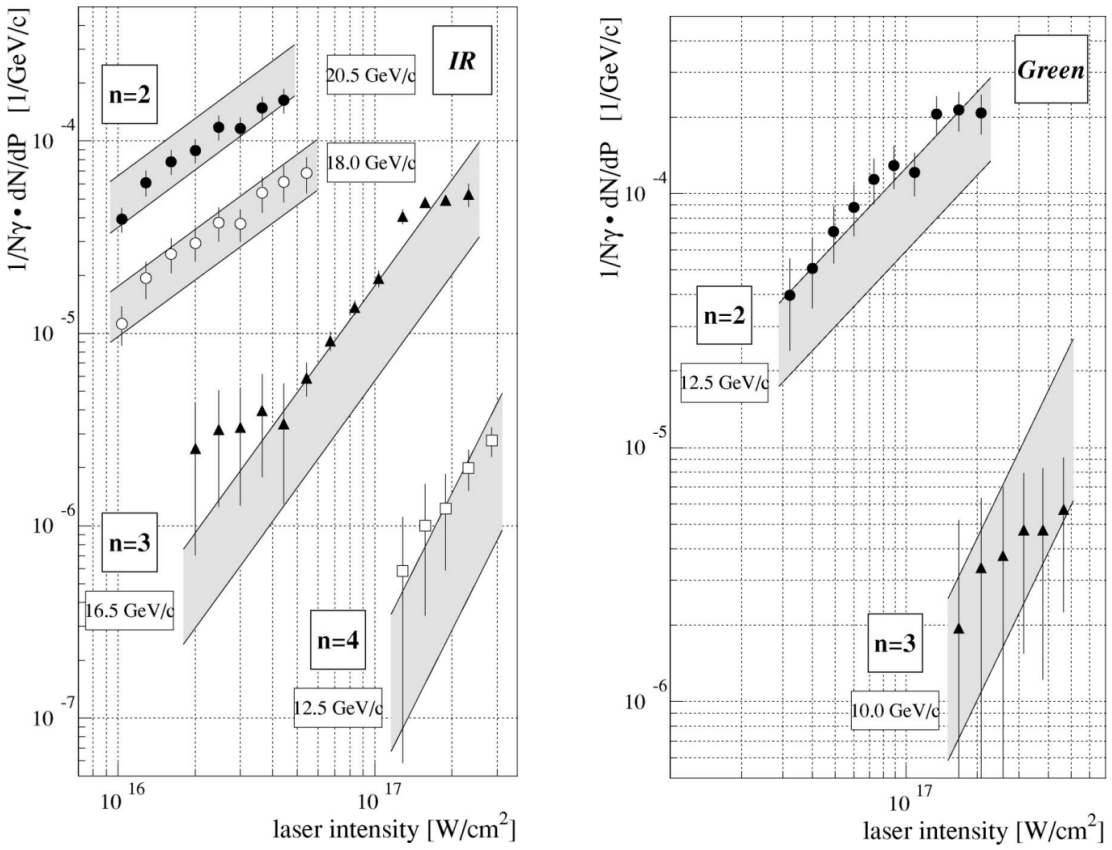

(a) **(b)**

Figure 2.6.: Results for the measured rates of electrons from the non-linear Compton scattering process, as measured by the E144 experiment. **(a)** shows four different datasets, for four differing points in the energy spectrum, with the infrared laser used, of wavelength 1053 nm. **(b)** shows an equivalent two datasets with the green-coloured laser of $\lambda = 527$ nm. Both are shown with respect to the intensity of the laser focus, but also normalised with respect to the photon intensity. Each point in the energy spectrum is labelled with the expected dominant order of the Compton process for that energy. The shaded areas shows the expectation for these yields from simulation with associated error bands chiefly from uncertainty on laser intensity [27].

interaction point, and the products of the interactions created therein are measured by an array of detectors.

The electron beam used is the FACET-II beamline, which has reduced energy in comparison to E144, at 13 GeV (compared to 46.6/49.1 GeV). Nevertheless the maximum χ achievable is far higher than previously possible due to the advancements in laser technology since E144. With an initial expected laser configuration of 17 TW, a peak intensity parameter (ξ) of 7.3 is reachable, corresponding to a χ value around 1.2.

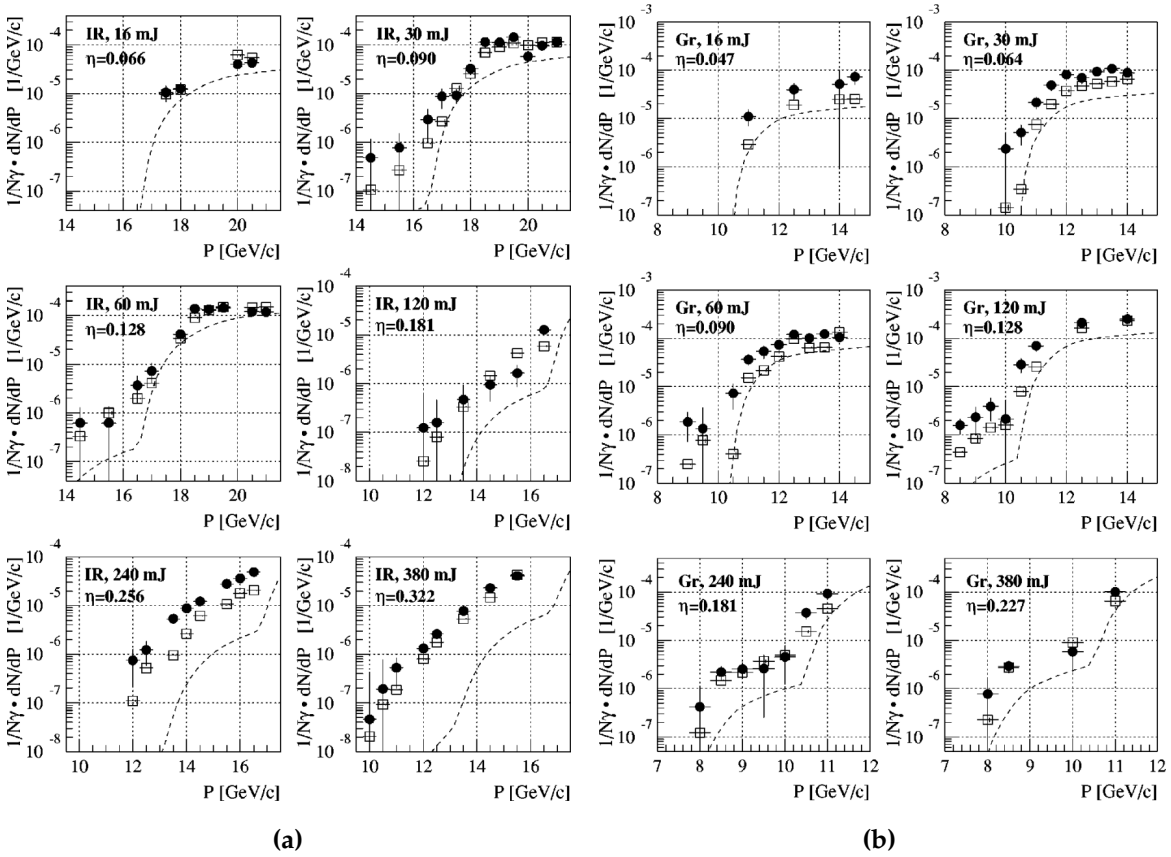

Figure 2.7.: Energy distributions of electrons from the non-linear Compton scattering process as measured by the E144 experiment. **(a)** shows six plots for six reconstructed values of unitless intensity (here η), with the infrared laser used, of wavelength 1053 nm. **(b)** shows an equivalent six datasets with the green-coloured laser of $\lambda = 527\,\text{nm}$. The black circles represent measured data; the empty squares are the expectation from SFQED simulation; the dashed lines represent only plural scattering, i.e. a solely linear simulation [27].

2.3.3. Astra-Gemini

An experiment at the Astra-Gemini laser system at the Rutherford Appleton Laboratory colliding laser pulses with relativistic electrons has been completed [30,31]. This was done using their twin-laser to simultaneously: power a laser-plasma accelerator as source of energetic electrons; and generate the strong field. This offers the advantage of an almost automatically temporally aligned combination of the laser and electron beam. However, this beam is more limited in energy and emittance compared to conventional electron acceleration present in other experiments, and so the flux of electrons at the desired energy will be invariably lower than those using a high-quality beam. This presented a novel method of using an existing laser to make measurements

Table 2.1.: The ξ and χ values reached by selected SFQED experiments.

Experiment	ξ	χ
E144	0.4	0.27
E320 (projected)	7.3	1.2
Astra-Gemini	~ 10	0.25
SPS 2018	not given	$\leqslant 1.4$
SPS 2023	not given	2.4

into the SFQED regime, but also remained challenged by low statistics and reached a χ value of ~ 0.25.

2.3.4. Strong Fields in Crystals

Although of lesser relevance to the LUXE in terms of the similarity of the apparatus, it should be remarked that as of time of writing the highest values of χ yet achieved have been in experiments which make use of crystal lattices. Experiments such as those in Refs. [32, 33], published in 2018 and 2023 respectively, made use of ≈ 200 GeV positrons (or electrons) from CERN's Super Proton Synchrotron (SPS). The beams were aimed at precisely oriented crystals; Refs. [32] and [33] used silicon and germanium targets respectively to generate χ parameters up to roughly 1.4 and 2.4.

2.3.5. Further Relevant Experiments

A brief comparison of the two crucial parameters of the mentioned experiments is given in Table 2.1.

A miscellany of further strong-field experiments with a variety of parameters, techniques, and states of development (from proposed to completed) also exist. More can be found in Refs. [34, 35].

Chapter 3.

The LUXE Experiment

3.1. Overview

This chapter details the proposed LUXE experiment: a new SFQED experiment currently being developed [1]. In the past three decades, technologies enabling higher intensities in the focal points of laser pulses have developed rapidly. With this fact, it is possible to design a successor to the E144 experiment, even with an equivalently or less energetic electron source, and explore entirely new parameter-space beyond that which was reached by the SLAC experiment, in terms of both the ξ and χ parameters defined in Chapter 2. The design is summarised in the name: 'LASER Und XFEL Experiment'. A modern, high-power laser will be constructed and its intense laser pulses collided with the high-quality high-energy European XFEL (EU.XFEL) electron beam (in an e-laser mode) to reach the most intense (assisted) electromagnetic fields currently possible. At the collision point, non-linear Compton scattering and multiphoton Breit-Wheeler interactions will be measured (see Figure 2.3). A parasitic approach to the EU.XFEL allows for continuous operation of LUXE throughout the year alongside the regular EU.XFEL photon physics program, and it is therefore expected that the experiment can accumulate high statistics for a variety of values of ξ and χ.

LUXE also presents the (unique in comparison to E144 and competing experiments) gamma-laser (or γ-laser) mode. This independent running mode uses the EU.XFEL electron beam to generate a high-energy photon beam, the characteristics of which can be independently measured, before these (real, on-shell) photons interact with the laser focus creating electron-positron pairs. This beam can be generated in the simplest case using a thin heavy-metal target inside the electron beampipe, stimulating

photon emission via Bremsstrahlung. Alternatively, by splitting the laser beam and generating a higher harmonic in the reflected beam, the electron beam may instead be initially scattered by a weaker higher-frequency laser beam. The resultant inverse-Compton-scattering photons are directed to the powerful laser focal point. In doing so, an effective monochromatic photon source may be used, which allows more precise analysis compared to a Bremsstrahlung spectrum. Polarisation of the produced gamma beam can also controlled, meaning the first measurements of polarisation-dependent pair-production at the IP can be investigated.

In each of the running modes, after colliding the electron/photon beam with the laser pulse, the resultant particles from the expected SFQED interactions continue travelling downstream in the direction of travel of the electron/photon beam. They are separated by charge with a magnetic field and each directed to integrated detector systems – one for each of electrons, positrons, and photons.

The following sections in this chapter first give descriptions of the EU.XFEL beam in Section 3.2, including its parameters and limitations of the experimental site, before a description of the laser system in Section 3.3. The third technical section is a brief description of each detector site and their sub-detectors. The description of the scintillator screen & camera system is kept brief as a detailed description of this detector is included in Chapter 5. Finally projections of the results, including estimates of interaction rates and an estimate of the sensitivity during the experiment's lifespan, are shown.

3.2. The EU.XFEL Accelerator

The EU.XFEL beam is a conventional RF-Cavity linear electron accelerator, used to generate extremely brilliant x-ray beams, which are then in turn used to image subjects down to the atomic level [36]. The quality of such an x-ray beam (in terms of its high brilliance, low energy spread and short pulse length) is ensured by using a high-quality high-energy electron beam to create the photons. The x-rays are generated by passing the electrons through magnetic undulators, stimulating synchrotron radiation (while oscillating the beam to keep it on-axis).

The EU.XFEL apparatus is 3.4 km long and stretches from the Deutsches Elektronen-Synchrotron (DESY) campus, where the beam originates, to a fan of beamline sites

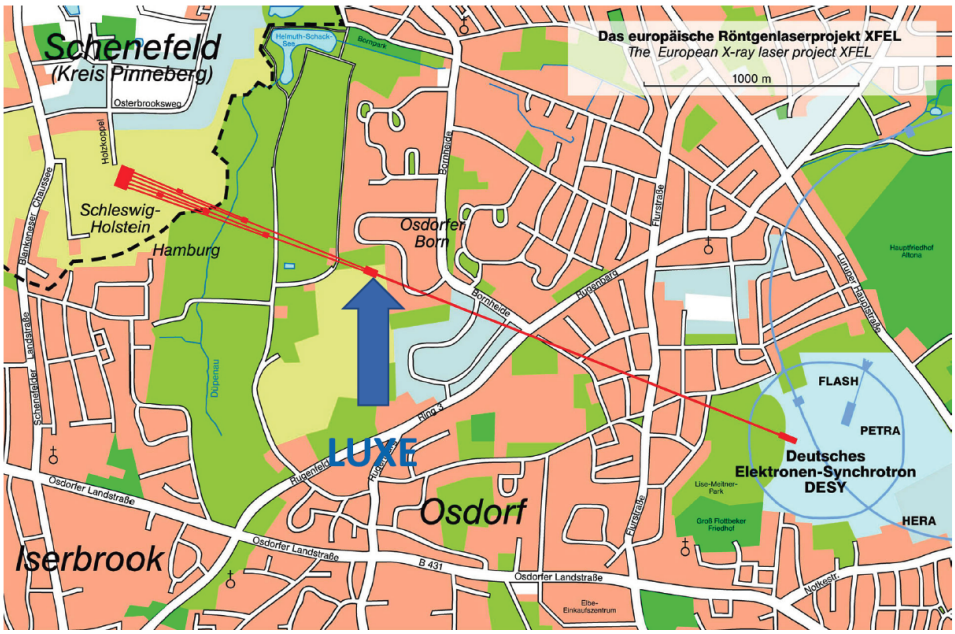

Figure 3.1.: A map of the west of Hamburg showing the location of the EU.XFEL linear accelerator and future site of LUXE [1].

northwest of Hamburg in Schenefeld. A graphic of its site is shown in Figure 3.1. In the middle of this beamline, just before the beam is split into a fan, the electron beam is already accelerated to its maximum energy for a given run. LUXE, which intends to use this beam at its highest energy, is located at this site. The architecture of the EU.XFEL beam is such that beam-trains of 2700 electron beam bunches are accelerated; the trains arrive at a rate of 10 Hz. With appropriate (and well-timed) kicker magnets, only one bunch per the 2700 of the bunch-train is appropriated for use in LUXE, minimally affecting the photon science downstream.

In Table 3.1 various parameters of the EU.XFEL beam are listed. These are only typical values, and are the values assumed for analyses within this thesis and in almost all LUXE literature. Note the EU.XFEL has the capability to run at various running energies and various bunch charges. In Figure 3.2 one can see the projected running times and beam energies for a typical year-long period; in this case, the calendar year 2022. The default running energy of 16.5 GeV for LUXE projections is represented (approximately) by 16.3 GeV beam-energy runs. These 16.3 GeV beam-energy runs constitute 66 of the 173 projected days of running at any energy, and an approximate data taking time over one year of 5.7×10^6 seconds. The other beam-energy runs will also be used for data-taking for LUXE, although their exact phenomena have not been so explicitly characterised in simulations. The maximum time of data-taking for

LUXE per year can be estimated then at 1.79×10^7 seconds; an approximate value of 10^7 s total data-taking time per year is used in projections, when taking into account unforeseen LUXE down-time.

Table 3.1.: Typical characteristics of the EU.XFEL electron beam. These parameters are assumed for following LUXE calculations and simulations.

Parameter	Value
Beam Energy [GeV]	16.5
Bunch Charge [nC]	0.25
Bunch Population [e^-]	1.5×10^9
Bunches / Bunch Train	2700
Bunch Train Frequency [Hz]	10
Spot-size at the IP [µm]	5-20
Bunch Length [µm]	30
Normalised Projected Emittance [mm mrad]	1.4
Energy Spread $\delta E/E$ [%]	0.1

The EU.XFEL currently runs with three x-ray beamlines propagating here down two separate chambers (XTD1, XTD2) which fan out from a common original electron beamline (XTL). There is an existing parallel chamber to the x-ray beamlines, ready for use in a possible future second-fan extraction to provide more x-ray beamlines. Until such a time, that is at least a decade in the future, this vacant chamber can house the LUXE experiment. A visualisation of the underground tunnels is available in Figure 3.3. This presents a convenient but physically limited space to place particle detectors, magnets and optical components to direct the powerful laser pulse.

To extract the bunches at the 10 Hz rate previously described, kicker magnets and beam-focusing quadrupoles are required, fitted to the main EU.XFEL apparatus. The installation of these components would in principle be the only disruptions to the operation of the EU.XFEL, but these additions will take place during the regularly scheduled beam-shutdowns.

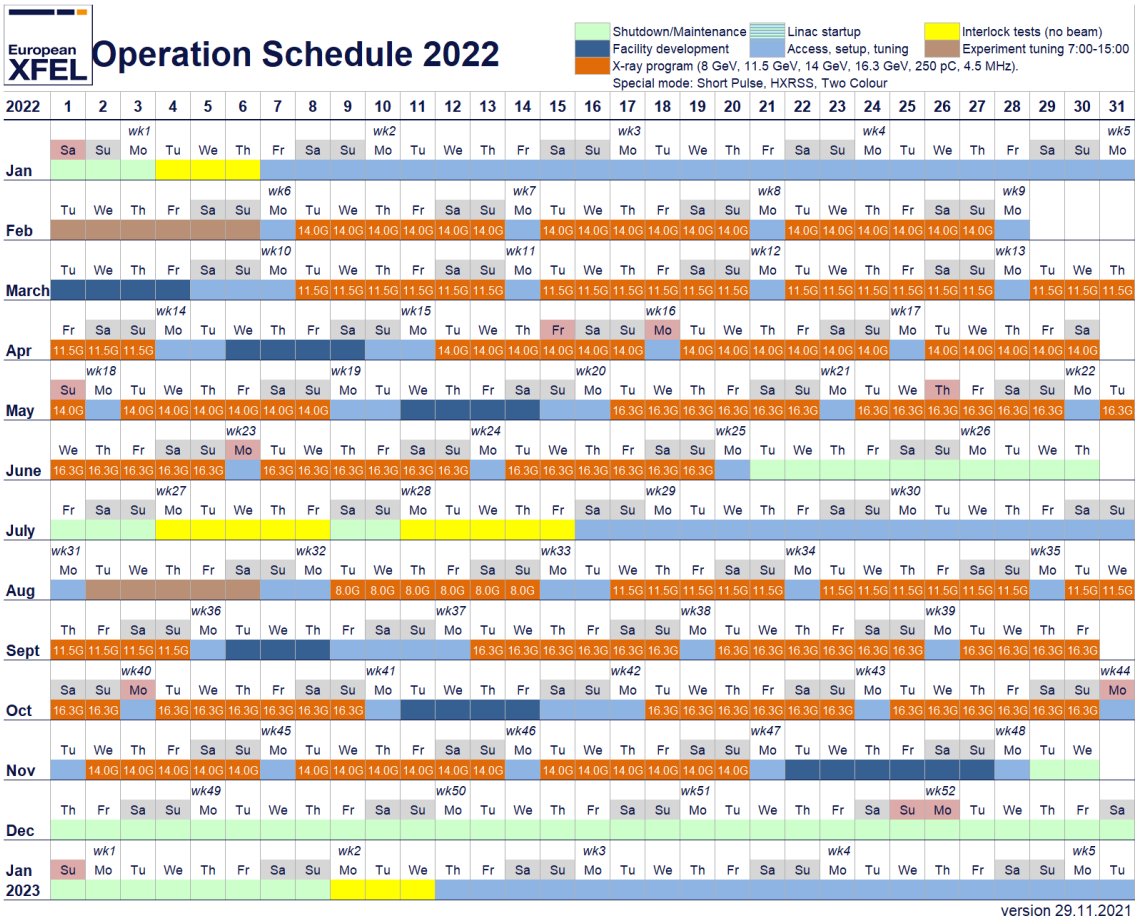

Figure 3.2.: The running schedule of the EU.XFEL accelerator for the year of 2022 [37]. This is characteristic of any year of running so far, and is taken as a realistic schedule for the operating years of LUXE. The orange time periods represent data-taking periods where the beam is present. Ref. [37] is updated to show the most recent operation schedule; 2022 is the most recent complete year of running at time of writing.

3.3. A Powerful Laser

In order to create some of the most intense electric fields possible in the lab today, a powerful, focussed, chirped laser pulse is used. The technique of 'chirping' the laser pulse (which earned the Nobel prize in physics in 2018 [38]) is one which can amplify the intensity reached at the maximum of the propagating laser pulse. The technique involves several steps. These are represented in Figure 3.4. The pulse is 'stretched', essentially enlarging it in time, before using a pump laser to amplify the longer pulse; the length of the pulse is then compressed, creating a very short yet intense pulse.

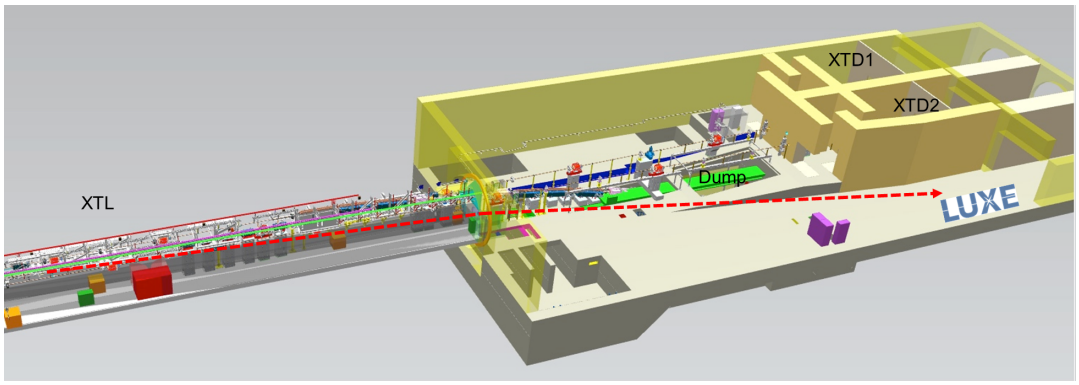

Figure 3.3.: A CAD visualisation of the underground EU.XFEL tunnels, including the currently unused XS1 shaft which will house LUXE [1].

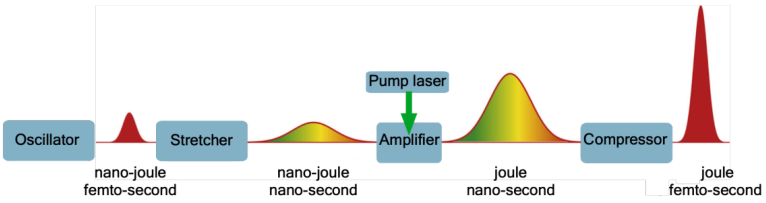

Figure 3.4.: A schematic of the process for generation of a chirped laser pulse [1].

LUXE intends to run in two exclusive phases (independent of the previously explained two *modes*, e-laser & γ-laser) named phase-0 and phase-I, which will involve the use of two different lasers, the latter more powerful than the former. For phase-0 the JETI-40 laser to be loaned from the University of Jena [39] brings a peak pulse power of 40 TW. Phase-I, using a second laser, brings an upgrade to the peak power up to 350 TW. The second laser must still be constructed before use. Both lasers use a Titanium-Sapphire construction, resulting in a monochromatic beam of wavelength 800 nm, and will be operated with an effective pulse repetition rate of 1 Hz[1]. The resulting laser pulse must be collided with the electrons (or photons) from the EU.XFEL in bunch-crossings of 1 Hz; the additional 9 Hz of the particle beam are used for background estimations in the detectors. Parameters for the intense field reached by the lasers are given in Table 3.2 for a particular tight focussing of the beam-spot to 3 µm. This represents the approximate upper limit of the intensity for each laser.

Despite the extreme intensity of the laser pulse produced, the laser photons can nevertheless be nimbly transported through an array of mirrors - keeping care to only focus the beam when necessary at the Interaction Point (IP), where it meets

[1] Although the JETI-40 laser has the capability to run at 10 Hz.

Table 3.2.: Parameters for a 3 µm beam-width focussing of the two LUXE lasers.

	Phase-0	Phase-I
Pulse Energy [J]	1.2	10
Pulse Duration FWHM [fs]	30	30
Laser Beam-Spot Width [µm]	3	3
Peak Intensity [Wcm^{-2}]	1.33×10^{20}	1.2×10^{21}
ξ	7.9	23.6
χ for $E_e = 16.5\,\mathrm{GeV}$	1.5	4.45
Repetition Rate [Hz]	1	1

the electron/photon beam. The plans for the laser clean-room include building a new, small building on the surface of the site, and simply piping the laser back and forth between the IP. A schematic of this in relation to the rest of the experiment (the underground magnets and array of detectors) is shown in Figure 3.5a. A visualisation of the interior of the designed IP chamber is shown in 3.5b.

The field of laser physics have developed instruments & detectors which can independently measure the properties of the laser beam, in particular at the focal point, which have been created in one laser shot. This conveniently allows for the measurement of ξ independent of the high-energy physics which occurs therein. In doing so, the interesting particle physics measurements of the rates and kinematics of the non-linear Compton scattering & multiphoton Breit-Wheeler interactions can be measured, and in a completely model-independent fashion, correlated directly to the ξ value at which they occurred.

A very brief overview of the diagnostic processes for the laser pulses, and what they can measure, includes:

- Energy Tagging - the full beam energy is measured, with an attenuated beam, onto a CCD device. Accuracy down to $<10^{-5}$.
- Fluence Tagging - a high-magnification image of the IP focal spot is projected onto a CCD camera.
- Pulse Length Tagging - using a Wizzler and autocorrelator the pulse duration precision is measured down to $< 10^{-3}$.

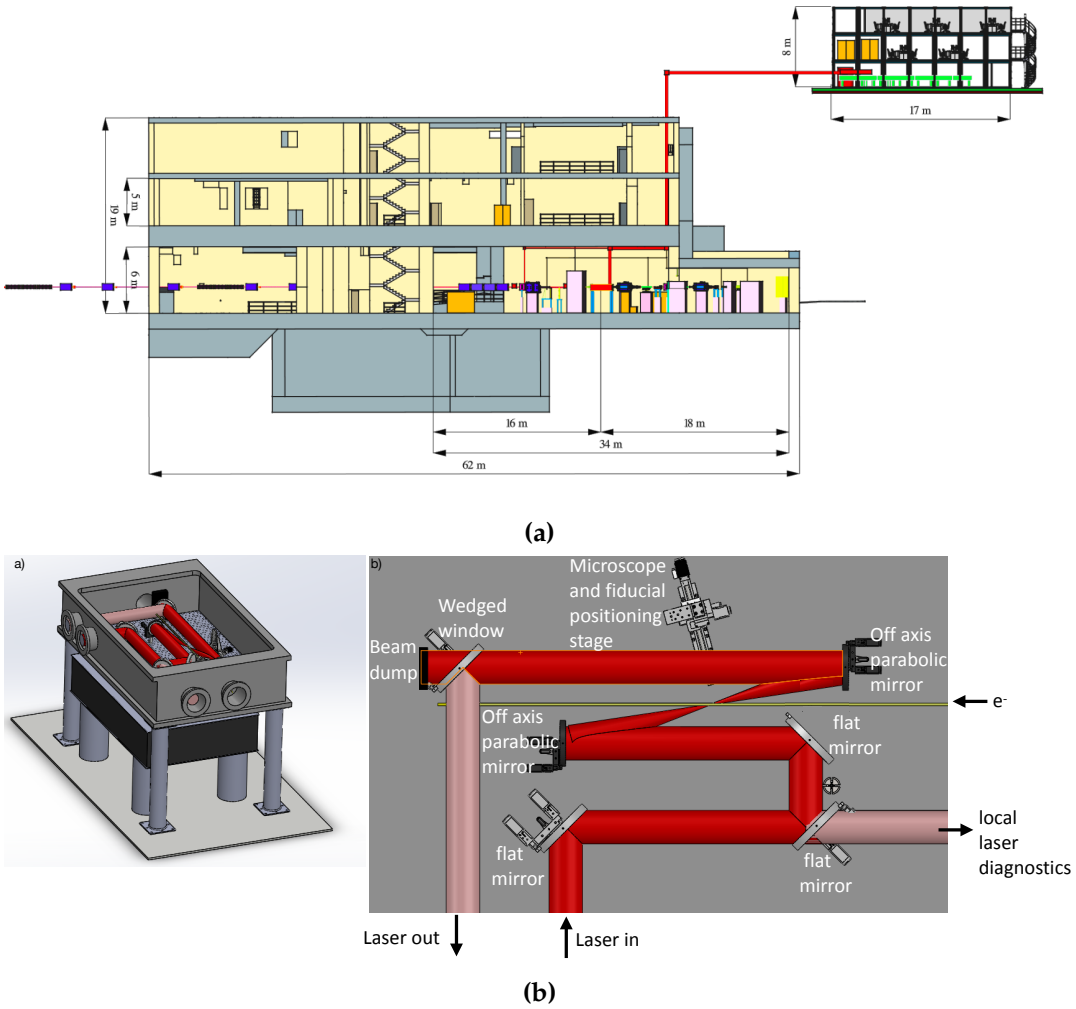

Figure 3.5.: **(a)**: A CAD illustration showing the position of the laser clean-room (top-right) with respect to the rest of the LUXE apparatus and EU.XFEL beamline. **(b)**: a CAD illustration of the interior of the IP chamber [40].

- Full Field Reconstruction - use INSIGHT [41] to then model the full field at focal point.

With these parameters measured, the distribution of unitless intensity ξ can then be calculated independent of the resultant high-energy physics measurements. Aberrations in imaging and optical transport affect the absolute value of ξ one can reconstruct, without being an obvious error source, leading to an accuracy in the absolute intensity reconstruction of $\pm 2.5\%$. Stability from laser-shot to laser-shot is better, giving an estimate for the laser-derived *relative* ξ reconstruction down to below 1% uncertainty

shot-to-shot. Note this is the accuracy of the reconstructed ξ and not the stability of the ξ produced shot-to-shot.

3.4. LUXE Detectors

Interactions in LUXE, regardless of the mode (e-laser or γ-laser), phase, or running beam energy, occur at the IP in a highly boosted centre-of-mass frame with respect to the lab frame. The resultant particles are therefore highly collinear along the beam axis.

The scattered electrons and radiated photons form a measurement of the non-linear Compton scattering; the multiphoton Breit-Wheeler interaction creates an electron-positron pair. Since the Compton interaction is so much more probable than the Breit-Wheeler process, electrons from the latter are not resolvable above the Compton-scattered electrons in the e-laser mode. Only the positron measurements inform us of the pair-production. In the γ-laser mode, there is no initial electron beam present in the IP and so measurements of both electrons and positrons can be made.

The three resultant particle types – electrons, positrons and photons – are separated by their charge with a dipole magnetic field. This is shown in Figure 3.6; looking at the e-laser setup, the three systems for measuring the electrons, positrons and photons are the Electron Detection System (EDS), Positron Detection System (PDS) and Gamma Detection System (GDS), located on the right, left and along the beamline, respectively. The constituent detectors of these three systems are:

- EDS: The scintillator screen and camera system and the Cherenkov detector.
- PDS: The silicon-based pixel-tracker detector and the sampling calorimeter.
- GDS: The scintillator screen and camera-based gamma spectrometer, the gamma profiler, and the backscattering calorimeter.

One should note, with respect to Figure 3.6, that the γ-laser apparatus exchanges the EDS of the e-laser mode for a copy of the PDS – this is due to the far smaller particle rates meaning the EDS is no longer suitable. In addition, the EDS is replicated at the photon generation site before the IP to monitor the photon beam generation interaction by reconstructing the discarded electron beam. Finally, at the end of the beamline in

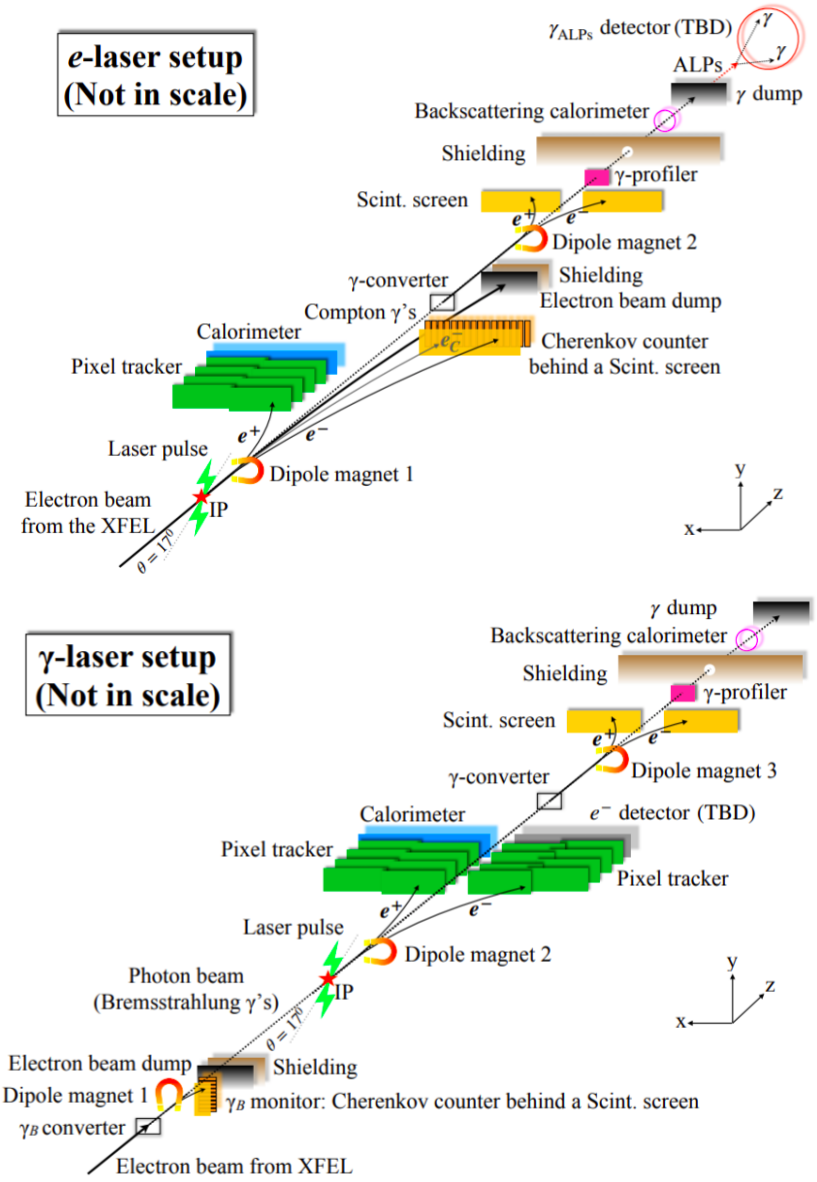

Figure 3.6.: A schematic of the LUXE experiment detector layout in its two modes. Above is the e-laser mode and below the γ-laser mode. [1].

both modes, some non-finalised detector system is used to make a convenient search for Axion-like particles.

A description of each of the components contained in Figure 3.6 is contained in the following subsections. Visualisations of the detector systems described are included in Figure 3.7, excepting the scintillator screen and camera system; several visualisations and a full description of this particular detector system are shown in Chapter 5.

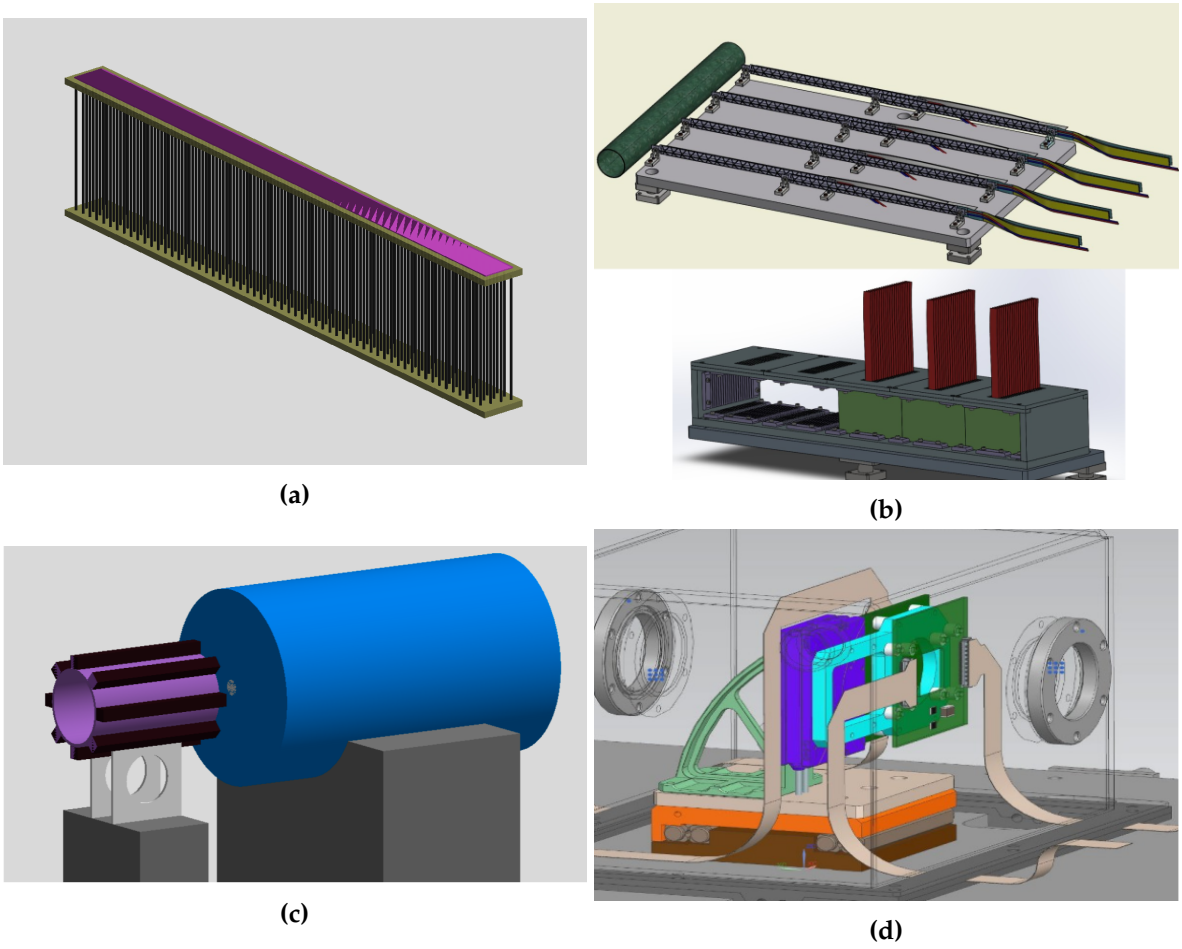

(a) **(b)** **(c)** **(d)**

Figure 3.7.: Illustrations of various LUXE detectors. **(a)** Shows the Cherenkov detector from the EDS. This shows the interior substructure, constructed of rows of low-density reflective straws. **(b)** An illustration of the silicon-wafer tracker detector (above) and the electromagnetic calorimeter (below), which together form the PDS. **(c)** shows the lead-glass gamma flux calorimeter blocks in purple, around the beam axis and in front of the photon beam-dump. **(d)** Shows an illustration of the sapphire-based gamma profiler.

3.4.1. Electron Detection System

The Electron Detection System, or EDS, has the function of reconstructing the rate and energy distribution of an intense flux of GeV-energy electrons emerging from the IP. It is formed of two sub-detectors: the scintillation screen & camera detection system, and the Cherenkov detector.

A detailed description of the scintillation screen & camera detection system, the detector which forms the main body of work in this thesis, is available in Chapter 5. In extremely brief terms, the electrons scattered by SFQED interactions are deflected with

a magnetic field; they are intercepted with a thin, high-efficiency scintillator which emits light locally in proportion to incident charge-flux, and the light is recorded with remote cameras. The imaged map of light, in combination with knowledge of the magnetic field, is used to reconstruct the initial energy distribution. This system offers a high position and therefore energy resolution, but is somewhat susceptible to the influence of background radiation not directly from the IP, including scattered photons.

The Cherenkov detector is designed as an array of independent channels of some transparent refractive medium. Within such a medium, the Cherenkov mechanism can take place; this is the emission of photons from charged particles which travel through the medium at a velocity higher than the phase velocity of light in that same medium. This is expressed through the refractive index n, such that Cherenkov emission is observed for a charged particle of velocity β when:

$$n\beta > 1, \quad \beta = v/c \tag{3.1}$$

The electron energy range in the EDS is constrained to around 1-15 GeV. For an electron of 1 GeV, the absolute velocity β is calculated as $1 - 1.3 \times 10^{-7}$. This value being so close to c means that some Cherenkov emission will be seen for this energy range in effectively any medium. The emitted photons appear in a cone along the direction of travel of the charge, with an effective angle of:

$$\cos(\theta) \approx \frac{1}{n\beta} \tag{3.2}$$

Their energy distribution is given by the Frank-Tamm formula:

$$\frac{d^2E}{dxd\omega} = \frac{\omega q_e^2 \mu(\omega)}{4\pi}\left(1 - \frac{\beta^2}{n^2(\omega)}\right) \tag{3.3}$$

where $\mu(\omega)$ denotes the frequency-dependent permeability of the medium. With the mechanism of the Cherenkov emission in mind, by choosing a relatively low value

of the refractive index n, an effective lower limit of the velocity of a charged particle which will induce the Cherenkov response is established. This correlates to an effective energy limit too. The choice of air near to atmospheric pressure will be used, giving $n = 1.00027$, and an effective energy limit for electrons/positrons at 21.6 MeV. This is equivalent to a Lorentz factor of 42.3. The second least massive charged particle in the Standard Model is the muon, and at 105.7 MeV the required energy to reach the minimum velocity is 4.47 GeV; or in other words, extremely suppressed in an experiment with a beam of maximum energy 17.5 GeV. Non-charged particles never create Cherenkov radiation (although through multiple scattering they can create charged particles which do). These considerations mean the response of the detector is very resistant to signal from particles of 'background' origin.

The physical design of the Cherenkov detector involves the use of straws as independent channels. These are filled with the refractive medium as described. A diagram of a single channel of the detector is shown in Figure 3.8. The electron flux passes through, and as per Equation 3.2, the photon flux is produced in a cone in a narrow angle. The interior of the straws are highly reflective, and reflect the light produced to an array of photodetectors. As with the scintillator screen, the light response is only used as measurement of the charge incident on each channel; the energy-differential measurement is reconstructed only using the position of the charge, after it has passed through the magnetic field, in the manner of magnetic spectroscopy. With good alignment, the photodetector response for a specific channel corresponds to the charge flux incident through a specific interval in the x dimension, corresponding to some interval in the electron energy spectrum, and can therefore be used for an energy interval reconstruction.

The fineness of the position resolution is variable - the diameter of the straws used are envisioned to be 3 mm. A finer resolution is in principle possible, but doing so greatly complicates the construction and operation of the system - as well as reduces the Cherenkov light response in each channel, as the path length of each electron through the medium is reduced.

3.4.2. Positron Detection System

The low rates expected for the Breit-Wheeler process means there must be a high power of background exclusion for positron detection. For this, the use of technologies

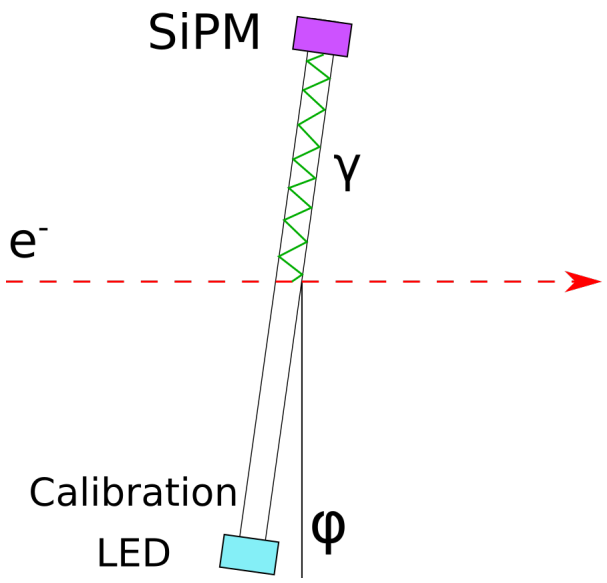

Figure 3.8.: A schematic of the Cherenkov detector. Incident electrons above the energy threshold induce Cherenkov photons which are internally reflected toward the silicon photodetector. On the opposite end of the straw lies an LED for calibration purposes.

which can utilise track reconstruction - including direct analysis of track calorimetry - are required. The combination of silicon pixel-trackers and silicon/GaAs sampling calorimeter(s) has been chosen for this.

In front sits the silicon tracker, composed of four layers of two staves each of 25 µm of silicon. The design is similar to (and based on) the ALPIDE tracker in development for ALICE [42]. Digital hits are generated from charge deposition in the silicon from ionising radiation passing through. A Kalman filter fitting algorithm is used to identify tracks from the hits, and those which fit geometric expectations for the positrons can be identified as signal, and so background excluded [43]. The best estimate for tracker sensitivity during LUXE running of positron production is down to 10^{-3} e^+ per bunch-crossing; at higher multiplicities above 10^5 tracking becomes unwieldy but simpler particle counting can continue with the improved SNR. The sampling calorimeter uses 20 tungsten plates to induce showering within the detector, which is then sampled by silicon or GaAs sensor layers to reconstruct the energy and position of tracks. This destructively but directly measures the energy of the track. Performance for this detector, from simulations of the LumiCal prototype [44], offer energy resolution of $\sigma/E = 20\%/\sqrt{E[\text{GeV}]}$ and position resolution at 500 µm.

To assist with reducing general background, mitigation shielding is placed above and below the beampipe which separates the high-flux electron side from the positron side. The feasibility of future quantum computers finding tracking solutions for the positron tracker detector is being evaluated. This entails taking the raw data of 'hits' in each layer of the tracker and finding the most accurate combinatorial solution as to which hits belong to which tracks (whether they originate from background or signal). The current limitation of the number of qubits available in current quantum computers restricts this to post-facto analysis.

3.4.3. Gamma Detection System

Three independent detectors are used to measure various characteristics of the photon beam in the Gamma Detection System. The gamma spectrometer uses a thin tungsten target to convert a proportion ($\sim 1\%$) of the gamma beam to electron-positron pairs, and using a Bethe-Heitler deconvolution algorithm and the summed energy of the e^-/e^+ pair, the energy distribution of the gamma beam is reconstructed [45]. The energy profile of the electrons and positrons are reconstructed with another scintillation screen & camera system, similar to the EDS, although the camera models used are more sensitive, with lower typical electronic noise, as the signal flux is far lower.

A sapphire-microstrip gamma beam profiler measures the flux and physical shape of the produced gamma beam. Two layers of these thin strips, one arrayed in the x dimension and one in the y, accumulate charge in response to the photon flux to a resolution of 5 µm. Sapphire is chosen for its resistance to radiation damage. The shape of the beam is crucial as it informs us immediately about the quality of the particle-laser interaction from bunch-to-bunch in the e-laser mode, and gives a high-quality measurement of the initial photon beam in the γ-laser mode.

Finally, in front of the gamma beam dump, a backscattering calorimeter measures the total photon energy flux using photon back-scatters from the beam dump. Eight lead-glass blocks are arranged around the beampipe; electromagnetic showering within the glass leads to Cherenkov light which is detected by photomultiplier tubes attached to the glass blocks.

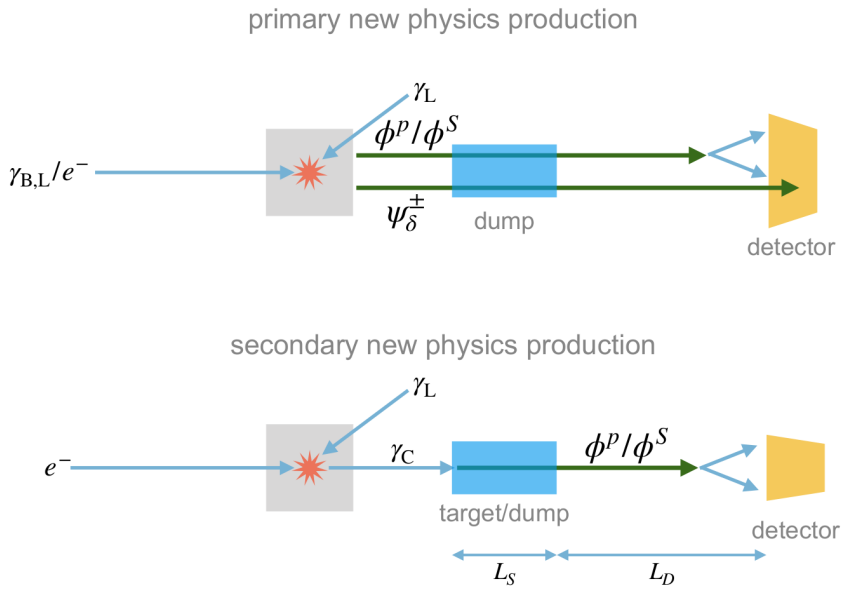

Figure 3.9.: A schematic showing the possible creation and subsequent detection of possible BSM particles [1].

3.4.4. Beyond the Standard Model Detectors

A search for particles Beyond the Standard Model (BSM) can be made using the LUXE apparatus; this will be done concurrently during normal data-taking operation. Direct production of Axion-Like Particles (ALPs) can occur in the IP. Alternatively, by virtue of producing a high-energy, highly focussed and well-populated photon beam, in the process of safely dumping the photon-beam ALPs may also be produced. The search is made on the premise that an ALP produced in either the IP of LUXE or the photon-dump will travel downstream through the photon-dump and its decay products will be detected by final BSM detectors. A schematic of this search is shown in Figure 3.9.

The detectors required to make this measurement are at a less mature level of development and design compared to the rest of the experimental setup. This poses ultimately no problem as installation of this addendum can happen at some point during the LUXE lifetime. Regardless of the details of the detector(s), their general requirements are known. As one can see in Figure 3.9, the required ALP is expected to decay to two photons in front of the final detector. A BSM detector then requires good energy resolution of photons, but also great pointing resolution in order to ensure photons are traced back to a common vertex (and so non-signal events are excluded).

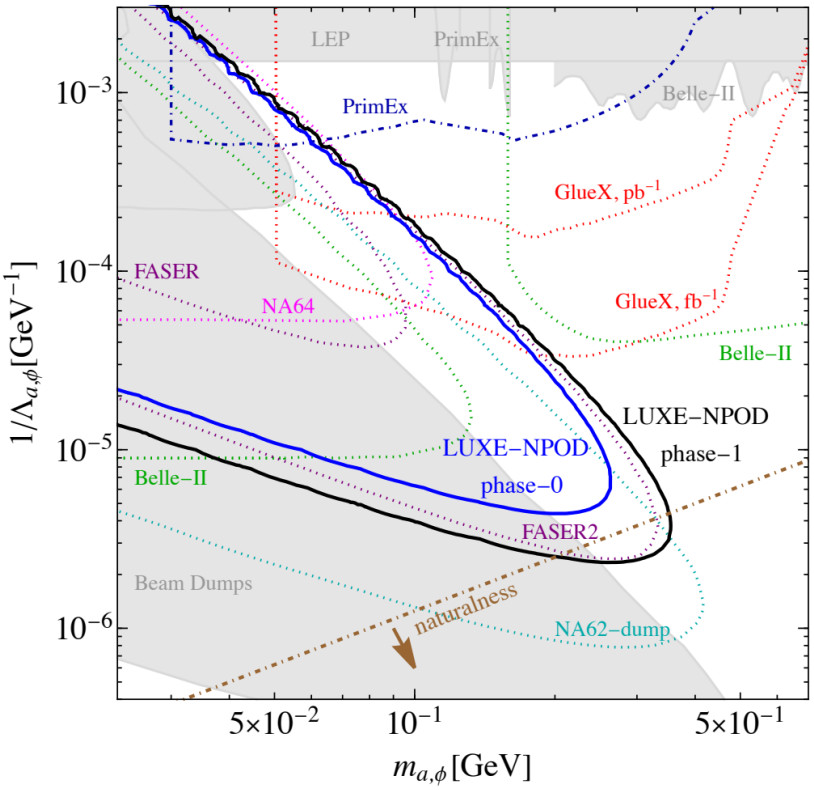

Figure 3.10.: The ALP parameter-space LUXE is expected to be sensitive to through the LUXE lifetime [46]. The comparison is made with other upcoming (dotted lines) and completed (solid grey areas) experiments and analyses. The parameters in the x,y axis are the mass of the ALP and ALP-photon coupling respectively. The grey shaded regions denote parameter-space which has already been excluded.

With reasonable assumptions for the quality of these detectors, the typical running photon fluxes, and cumulative bunch-crossings achieved, the LUXE-NPOD group (New Physics search with an Optical Dump) at LUXE have calculated the region of parameter-space which the search of ALPs at LUXE are sensitive to; these parameters are the mass and a scattering cross-section of the ALP [46]. This is shown in Figure 3.10.

3.5. Expected Results

The physics goals of LUXE can be summarised in the measurement of the rates and kinematics of the produced particles from non-linear Compton scattering and the multiphoton Breit-Wheeler process. As previously elucidated, these depend on the ξ and χ parameters. The region of parameter-space LUXE expects to be able to measure

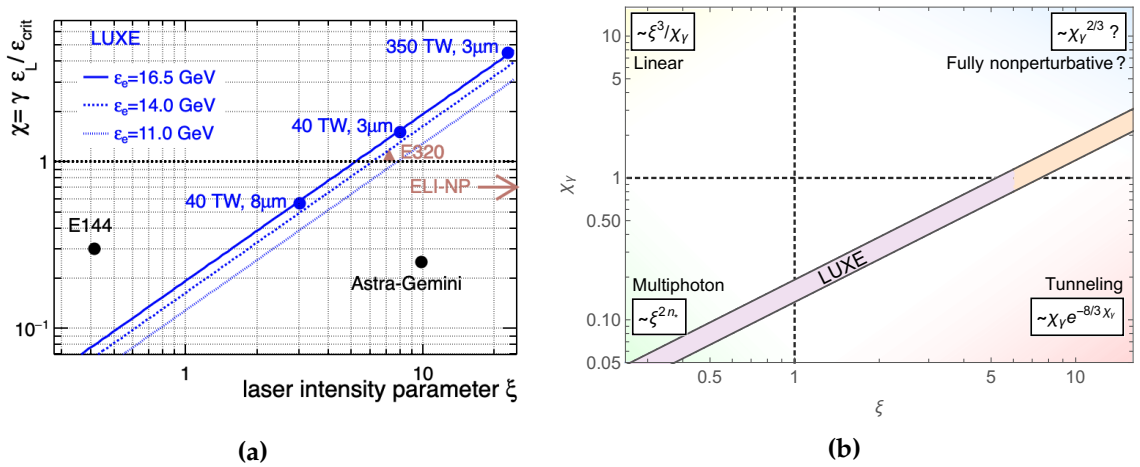

(a) (b)

Figure 3.11.: **(a)** shows the region(s) of parameter-space LUXE intends to measure, in comparison to other past and future experiments. **(b)** gives the transition between several approximate SFQED regimes regarding the probability of the Breit-Wheeler process that LUXE intends to probe [1, 47].

is shown in Figure 3.11. A comparison is shown to other relevant experiments in Figure 3.11a, as well as the regions of SFQED Breit-Wheeler process modes LUXE will probe, with reference to the regimes defined in Chapter 2 and how the process probability evolves, in Figure 3.11b.

The typical rate of the non-linear Compton scattering is much higher than that of the Breit-Wheeler process. The measurement of the kinematic features of the Compton process, which can become more difficult to identify for increasing ξ, is aided by the generous statistics per bunch-crossing. The expected number of photons and scattered electrons per bunch-crossing are given in Figure 3.12a, for varying ξ parameter within the two different phases of LUXE. These results are generated using the electron and laser beam parameters, and the SFQED simulation PTARMIGAN [48]. The yields are different between the two phases even for equal maximum ξ, as the distribution of ξ surrounding the maximum of the phase-1 laser spot is wider and so causes more interactions with the periphery of the electron beam. These projections to not include shot-to-shot jitter between the beams either spatially or temporally. The number of electrons which have scattered saturates at the maximum of the beam population, whereas the number of photons continues to grow as each electron within the beam radiates on average more than one photon.

Within the reconstructed electron/photon energy spectra the Compton edge position is measured. Its simulated position is compared to the theoretical expectations in

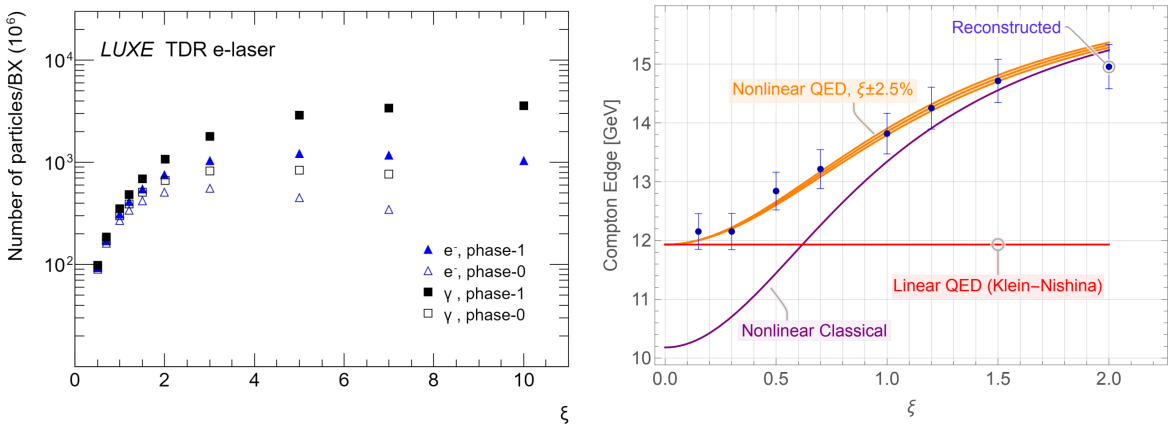

(a) **(b)**

Figure 3.12.: (a): Expected yields of scattered electrons and photons per bunch-crossing at LUXE for various ξ. **(b)**: Comparison of expected experimental results of the Compton edge position and theoretical expectations [47].

Figure 3.12b. There are some expected reconstruction points, associated with a $\pm 2\%$ error, as well as the non-linear QED expectation with error bands for an uncertainty of $\pm 2.5\%$ on ξ . The distinction is seen between the non-linear QED approach and the simple linear QED or non-linear classical expectations.

The measurement of the rates and kinematics of the multiphoton Breit-Wheeler process is a more subtle endeavour. Figure 3.13 shows the expected yields per bunch-crossing for both the e-laser and γ-laser modes in both phases of LUXE. This is expressed in numbers of positrons, one of which is produced in each instance of the Breit-Wheeler process, and the detection of which is the sole measurement of the interaction in the e-laser mode. The plot is shown without detector emulation, and so it is not clear a quality measurement can actually be made to a precision of 10^{-5} positrons/bunch-crossing; in reality, a measurement down to a rate of 10^{-3} positrons per shot is likely from performance expectations of the tracker detector [1].

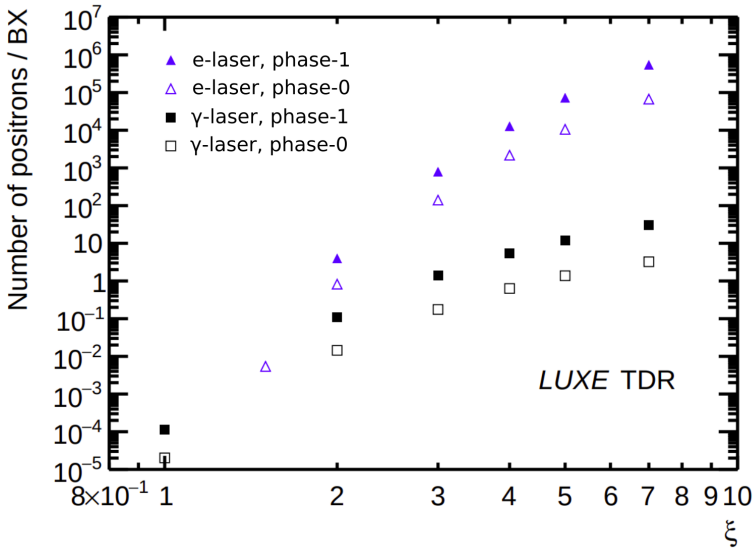

Figure 3.13.: Expected yields of positrons per bunch-crossing at LUXE for various ξ in both the e-laser and γ-laser modes [47].

Chapter 4.

High-Energy Bremsstrahlung Analysis

The γ-laser mode of LUXE sets it apart from previous and contemporary SFQED experiments. So far experiments have relied on the trident process to induce multiphoton Breit-Wheeler interactions, which rely on an understanding of the non-linear Compton scattering beforehand; in LUXE's γ-laser mode, an independently measured beam of real photons will be used for a more direct probe of the process. Crucial to the success of this mode is the ability to deliver a high flux of high-energy photons to the IP, to be intercepted with a laser pulse.

A hard, high-flux beam will be created using the EU.XFEL electron beam and a thin heavy-metal target, designed to induce Bremsstrahlung emission. The parameters of this beam are dependent on the well-characterised high-quality EU.XFEL beam and the Bremsstrahlung mechanism. Having confidence in the mechanism of Bremsstrahlung at these high energies, especially the population and divergence of the resulting photon beam, is therefore of paramount importance.

This chapter details the motivation, apparatus, and analysis of a test-beam experiment designed to measure the divergence of a high-energy photon beam generated by Bremsstrahlung.

4.1. Bremsstrahlung

Bremsstrahlung is, within the context of the SM, an extremely simple interaction. Represented by the Feynman diagram in Figure 4.1, this is the radiation of a photon by a charged particle (in the diagram and throughout this chapter, an electron). This

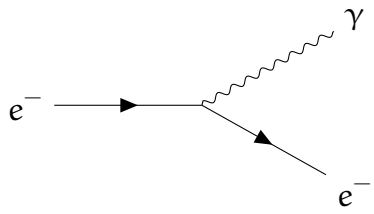

Figure 4.1.: Bremsstrahlung.

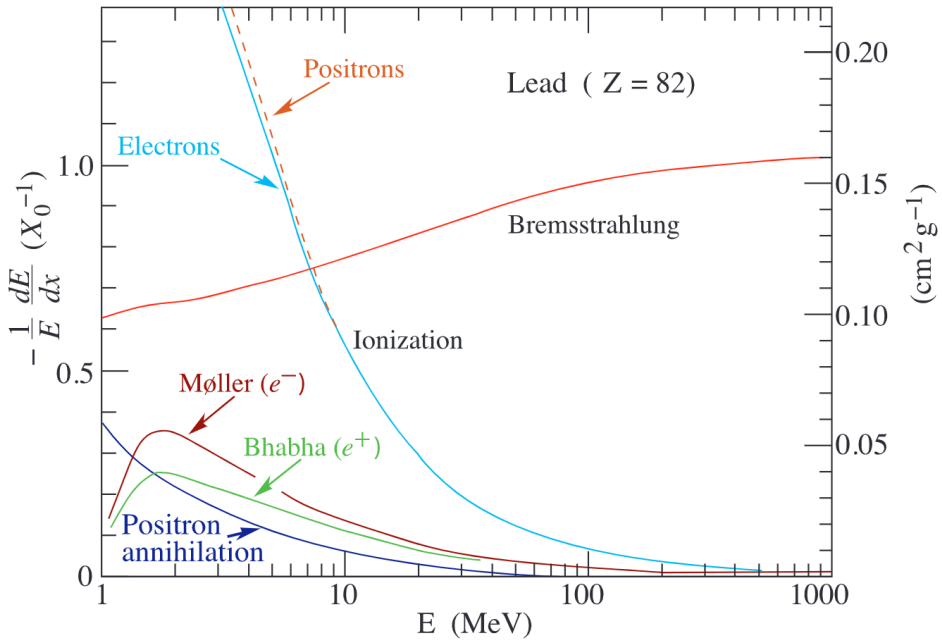

Figure 4.2.: Comparison of energy loss per unit depth travelled within lead by electrons / positrons. Plot from the PDG Review of Particles in Matter [49], in which it is stated that the plot is adapted from Ref. [50].

interaction forms the dominant mode of energy loss for highly energetic electrons travelling through matter.

In Figure 4.2 the relative (fractional) energy loss per unit distance in lead for electrons / positrons of varying energies is shown. Bremsstrahlung is relevant at all energies but particularly dominates in comparison to the other listed modes of radiation at higher energies, becoming the most likely mode at around 10 MeV.

The theoretical treatment of Bremsstrahlung in terms of a relativistic electron amongst high-charge nuclei, completed with QED, returns an emitted photon distribution which falls with rising energy. The probability of such an emission in the relativistic limit of the Bremsstrahlung process can be given as:

$$\frac{d\sigma}{dk} = \frac{4\alpha r_e^2}{3k}\left[(y^2 + 2(1+(1-y)^2))(Z^2(F_{el}-f) + ZF_{inel}) + (1-y)\frac{Z^2+Z}{3}\right] \tag{4.1}$$

with the fine-structure constant α and the classical electron radius r_e. The value k is the photon momentum; y is defined as k/E, the proportion of initial electron momentum carried by the photon (with E the initial electron energy). This expression also uses the atomic number, elastic and inelastic form factors (Z, F_{el}, F_{inel}) which are dependent only on the nuclei present in the medium.

The flux of high-energy photons from Bremsstrahlung is also dependent on the angular emission profile. As seen in the Physics Reference Manual for the particles-in-matter simulation software GEANT4 [51], finding simple formulae for the angular dispersion of the Bremsstrahlung interaction is not easy. For a solution, GEANT4 uses the differential cross-section from Refs. [52, 53]:

$$\begin{aligned}\frac{d\sigma}{dk d\Omega} = \frac{2\alpha^2 e^2}{\pi k m_e^4}\Bigg(&\left[\frac{2y-2}{(1+u^2)^2} + \frac{12u^2(1-y)}{(1+u^2)^4}\right] Z(Z+1) \\ &+ \left[\frac{2-2y-y^2}{(1+u^2)^2} - \frac{4u^2(1-y}{(1+u^2)^4}\right][X - 2Z^2 f_c(\alpha Z)^2]\Bigg)\end{aligned} \tag{4.2}$$

with X defined as:

$$X = \int_{t_{min}}^{m^2(1+u^2)^2} [G_Z^{el}(t) + G_Z^{in}(t)]\frac{t-t_{min}}{t^2}dt \tag{4.3}$$

$$t_{min} = \left[\frac{k m_e^2(1+u^2)}{2E(E-k)}\right]^2 \tag{4.4}$$

with atomic form factors $G_Z^{el}(t)$, $G_Z^{in}(t)$, and t representing the momentum transferred. Crucial to this study, the polar angle is expressed within:

$$u = \frac{E\theta}{m_e} \tag{4.5}$$

with θ the polar angle. Given that the dependence of the shape of the function on Z and E is small, the distribution is sampled with an approximative function of the form:

$$f(u) = C(ue^{-au} + due^{-3au}) \tag{4.6}$$

in GEANT4. The constants are defined as:

$$a = 0.625, \quad d = 27, \quad C = \frac{9a^2}{9+d} \tag{4.7}$$

4.1.1. Experimental Validation

The existing literature of the experimental side of the Bremsstrahlung mechanism for high-energy electron emission (multiple-GeV) has some data to confirm the theoretical result. In particular, two experiments performed at SLAC [54] and CERN [55] provide information on the relative rates of production of photons at GeV energies from electron beams of 8 & 25 GeV, and 149, 207 & 287 GeV respectively.

Selected results from both experiments are shown in Figures 4.3 and 4.4. The reconstructed energy profiles of the high-energy Bremsstrahlung photons match the calculations well. The SLAC measurements shown are performed using a thin tungsten target to induce the Bremsstrahlung reaction, as will be used in LUXE. The LUXE target is expected to be 35 µm thick, or 1% of tungsten's radiation length. The most significant deviations, in the SLAC experiment in Figure 4.3, occur at the low-energy region of the plots, and so have little relevance for LUXE interactions where only photons greater than 1 GeV are expected to interact in the multiphoton Breit-Wheeler process. Each of these experiments' analysis of rates with respect to energy proved to well validate the model used in the particles-in-matter simulation GEANT4 [56].

These studies do not make measurements in their high-energy interactions for one aspect that should prove crucial for LUXE: the divergence of the produced Bremsstrahlung beam.

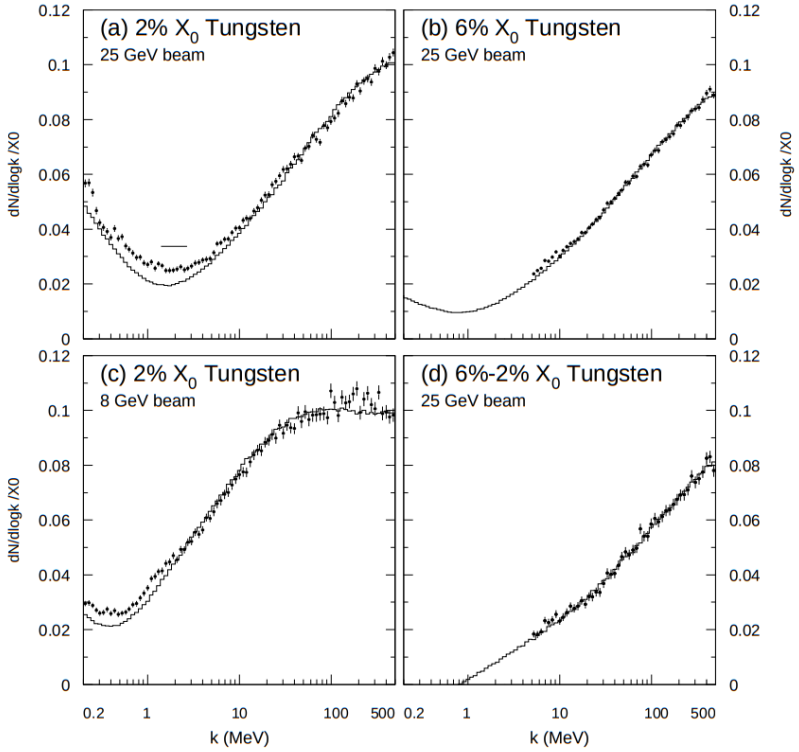

Figure 4.3.: Results for the energy distributions for high-energy Bremsstrahlung photons from the SLAC experiment [54]. Each sub-plot shows the measured data for various thicknesses of the metal target and two settings for beam energy. The data are in black bars, and compared to the theoretical calculation in the solid line. Sub-plot **(d)** shows the result of the bin-by-bin subtraction of **(a)** from **(b)**, performed in order to remove effects from the physical surface of the target and analyse the 'middle 4%'.

4.2. Experiment with the DESY-II Test-Beam

The DESY-II test-beam provides an electron beam of variable energy in the GeV range, wherein individual electrons can be temporally distinguished [57]. The mechanism of the beam generation involves the conversion of the DESY-II 6-7 GeV synchrotron beam into a spectrum of GeV-energy photons via Bremsstrahlung. This is done with a carbon fibre target. These photons, with a falling approximate $1/E$ energy dependency, are then intercepted with a heavy-metal target, creating an electron-positron pair with total energy equal to their mother photon. The GeV-energy resulting leptons are deflected with a magnetic field, creating a planar fan of electrons, where the electron position is dependent on both energy of the particle and the intensity of the dipole magnetic

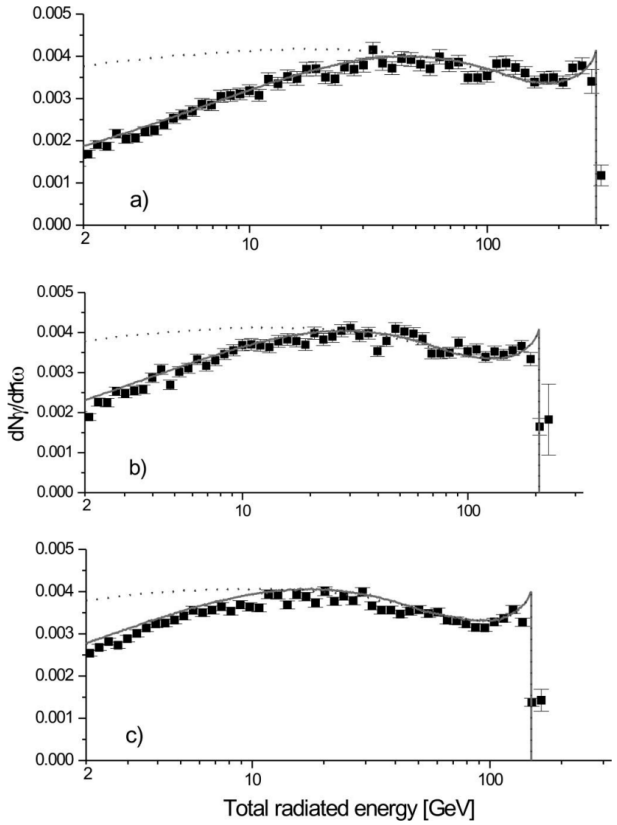

Figure 4.4.: Results for the reconstructed energy distributions for high-energy Bremsstrahlung photons from the CERN experiment [55]. Plots **(a)**, **(b)** and **(c)** show profiles for beam energies of 287, 207 and 149 GeV respectively. The electrons hit differing thin metal targets of iridium, tantalum and copper respectively. The black bars are data; the dotted and solid lines are the results of two simulations, the former based on only Bethe-Heitler spectra and the latter including a Landau-Pomeranchuk-Migdal effect correction (explained further in Ref. [55]).

field. With a fixed, collimated beam-exit area, a small region of the energy range is passed through a beam-window and outside the vacuum. The central energy of this energy slice can be chosen by the user by changing the magnetic field, allowing for a scan through the 1-6 GeVenergy range. The beam can then deliver, for the user, up to 6 GeVelectrons in a non-focussed but collimated beam of around 1 mrad divergence. A plan of the test-beam hall at DESY-II is shown in Figure 4.5, which includes a schematic of this beam generation process. These electrons come at a variable rate, dependent on the energy chosen. Due to the 1/E energy dependence, this rate is lowest for the electrons of highest energy. The typical momentum spread of the collimated beam is shown to be $158 \pm 6\,\mathrm{MeV/c}$ [57].

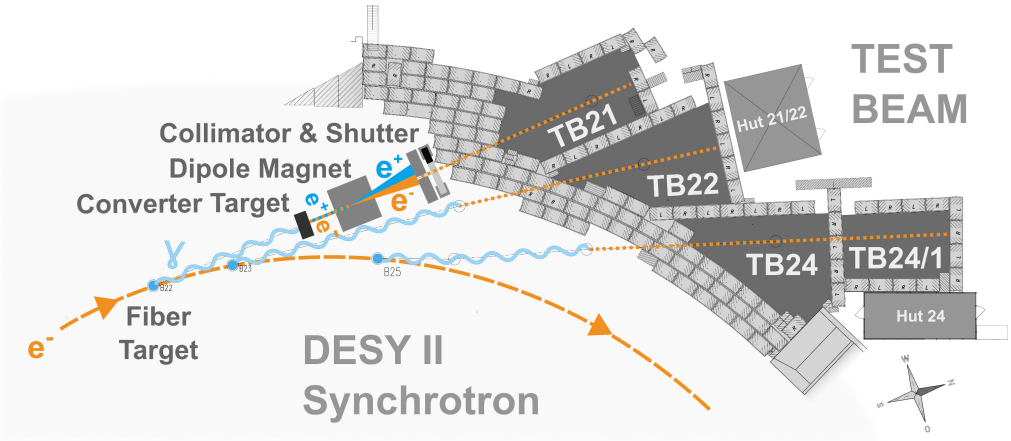

Figure 4.5.: A plan of the DESY-II test-beam experimental hall, with a graphic illustrating the beam generation mechanism [58].

4.2.1. Apparatus

The design of the experiment is to induce a certain sequence of events / interactions for (some fraction of) electrons in the produced beam. This sequence is elucidated below, and represented visually in Figure 4.6. The intention is to track charged particles and thereby reconstruct high-energy photons produced in the Bremsstrahlung interaction in order to measure the polar angle of the radiated photon with respect to the initial electron.

The detection of the particles required for this analysis is performed, besides the simple use of plastic scintillators for triggering, by MIMOSA26-sensor detector planes [59]. This data is collected using EUDAQ [60] software, and a clustering of the activated pixels was performed using the (now largely deprecated) EUTelescope software [61, 62]. The MIMOSA26 detectors are monolithic CMOS-based sensors of pitch-size 18.4 µm and a modest readout time of 115.2 µs. It has been noted that the performance of the sensors in a telescope detector can give a detection efficiency of 99.5 % while maintaining a fake rate of 10^{-4} per pixel at room temperature [63].

Analysis is made using only the six total MIMOSA EUDET detector planes. As visible in Figure 4.6, a prototype for the FCAL calorimeter detector was present, but the comparative looser position resolution of the FCAL prototype means the data from this device was not incorporated into the analysis. The beam energy chosen is 5 GeV. The first two scintillators generate a trigger upon activation due to a beam electron passing through. The second two scintillators are placed in the path of electrons of

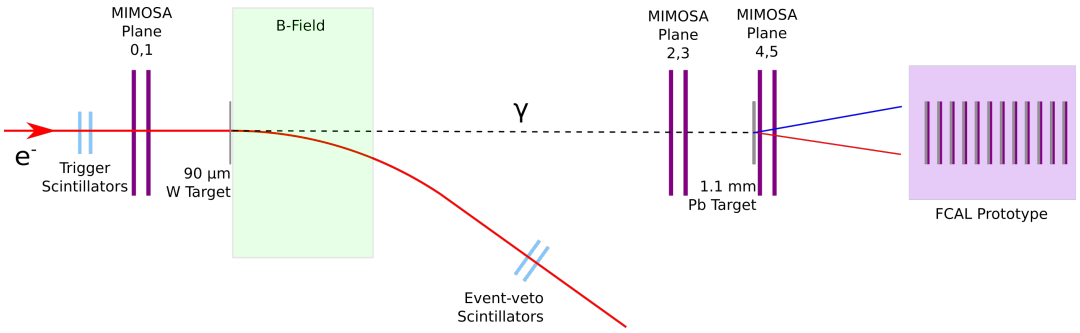

Figure 4.6.: A schematic for the layout of the experiment performed at the DESY-II test-beam.

5 GeV after the magnetic field; this then vetoes events in which electrons have not radiated via Bremsstrahlung (or very low-momentum-transfer events).

Event Selection

As mentioned, there is a sequence of events which the event selection looks for:

- First, the desired single electron must make it through the narrow collimator. The chosen beam energy of 5 GeV results in a low particle rate, and despite the mediocre temporal resolution between the MIMOSA detector planes one-electron-at-a-time events are easily analysed using the following event selection.
- The electron then passes through the first two MIMOSA detector planes. At this point, the proximity of the detectors to the collimator and the high detection efficiency of the detector planes mean that the vast majority of beam electrons create one hit in each of these detector planes. Selection requires exactly one hit in each.
- The selected electron, in addition to some distance of air, then passes through a thin tungsten target (90 µm), where some significant fraction radiates through Bremsstrahlung. From simulations, it is seen that the proportion of events which do radiate via Bremsstrahlung is expected to be around 31%.
- The electron and its daughter photon immediately then enter a relatively strong magnetic field ($\sim$0.3 T for $\sim$1.5 m). Within the dipole field, the two particle species are then separated. The photon continues travelling along the same vector at which it was created.

- A desired event here requires that the photon passes through $\sim$7.5 m of air and then two MIMOSA detector planes without interaction. For selection rules, this means events with zero occupancy in the MIMOSA planes 2,3 are chosen. Performing this cuts down on interfering background events where charged particles may be travelling downstream here, instead of the desired photon.

- Downstream of this is the second heavy-metal target, this time of 1.1 mm of lead, designed to induce a conversion of the high-energy photon to an electron-positron pair.

- The produced electron and positron then continue downstream, and depending on their momenta / opening angle, will both be detected by the last two MIMOSA planes. These two planes are relatively close behind the second target, so the charge deposition of the two leptons can easily spatially overlap. The MIMOSA detector signal does not attempt to measure charge magnitude besides measuring whether each pixel is above a threshold, so each pixel is simply activated or not. This means the case of 2 or more lepton tracks which deposit charge near one another is not easily distinguishable from a single charged particle. This is particularly pronounced in plane 4 but also possible in plane 5. For this reason selection is made of detection of:
  1 hit in plane 4 and 1 hit in plane 5;
  1 hit in plane 4 and 2 hits in plane 5;
  or 2 hits in plane 4 and 2 hits in plane 5;
  but not 2 hits in plane 4 and 1 in plane 5, as this almost certainly means one of the two leptons is lost and has not produced signal in the last detector plane.

- Finally, again dependent on the vectors of the final electron-positron pair, the two leptons are detected by the FCAL calorimeter prototype downstream, which destructively measures the showers of each track.

This particular sequence of events is a relatively unlikely one. In simulation it is seen that the number of events, defined as the passing of one single 5 GeV electron through the geometry, that go on to pass this selection is around 0.6%. Nevertheless, for a dataset from the test-beam campaign of around 5 million events, the number of successful events passing selection is of order 30,000 – statistics enough for analysis. In reality, the total number of selected events broadly agrees at $\sim$50,000 events. A small dataset where the heavy metal targets and magnetic field were removed to assist in post-facto alignment was also recorded.

To analyse the datasets, first a cleaning of the data was performed. This involved removing events where an outlying hot pixel was identified. The definition required histogramming of the data in terms of their x, y position, and removal was performed for pixels which produced hits at a rate significantly more than the mean of their neighbouring pixels.

The sum of all the Bremsstrahlung data, in terms of a map of all hits after the cleaning, is shown for each MIMOSA detector plane in Figure 4.7. The square shape of the collimated beam can clearly be seen in the first two detector planes; the next two planes have a considerably lower occupancy as the electrons are diverted by the magnetic field. The occupancy of the last two planes then increases again, as a number of high-energy photons are successfully converted to a lepton pair by the secondary lead target.

Figure 4.8 shows the maps of hits for events which have passed the selection described. There are necessarily zero hits in the intermediate two detector planes. Otherwise the shape of the signal follows that of Figure 4.7 with lesser statistics.

Figure 4.9 shows the same hit maps for the alignment dataset, where the heavy-metal targets and magnetic field are removed / deactivated, and a selection of one hit in each plane is used. The statistics of this set are the most challenged, with only 16186 events.

4.2.2. Alignment Validation

Alignment-Specific Data

Data was taken with the DESY-II test-beam with no metal targets and no magnetic field. This allows for the typical method of alignment of particle detectors, where a large set of hits between the detector planes are recorded and expected to be in a straight line. The sum of residuals – the difference between each hit and the linear best-fit of the hits – are calculated, and by varying alignment parameters this sum is minimised. Should the process converge, the best possible alignment is then calculated (limited by statistics of the dataset and how close the particles follow a straight line).

Alignment of the apparatus was crucial for the analysis. This was particularly pronounced within the first two planes, as they are the only detectors used in the reconstruction of the initial electron. With the measured difference in z position (with

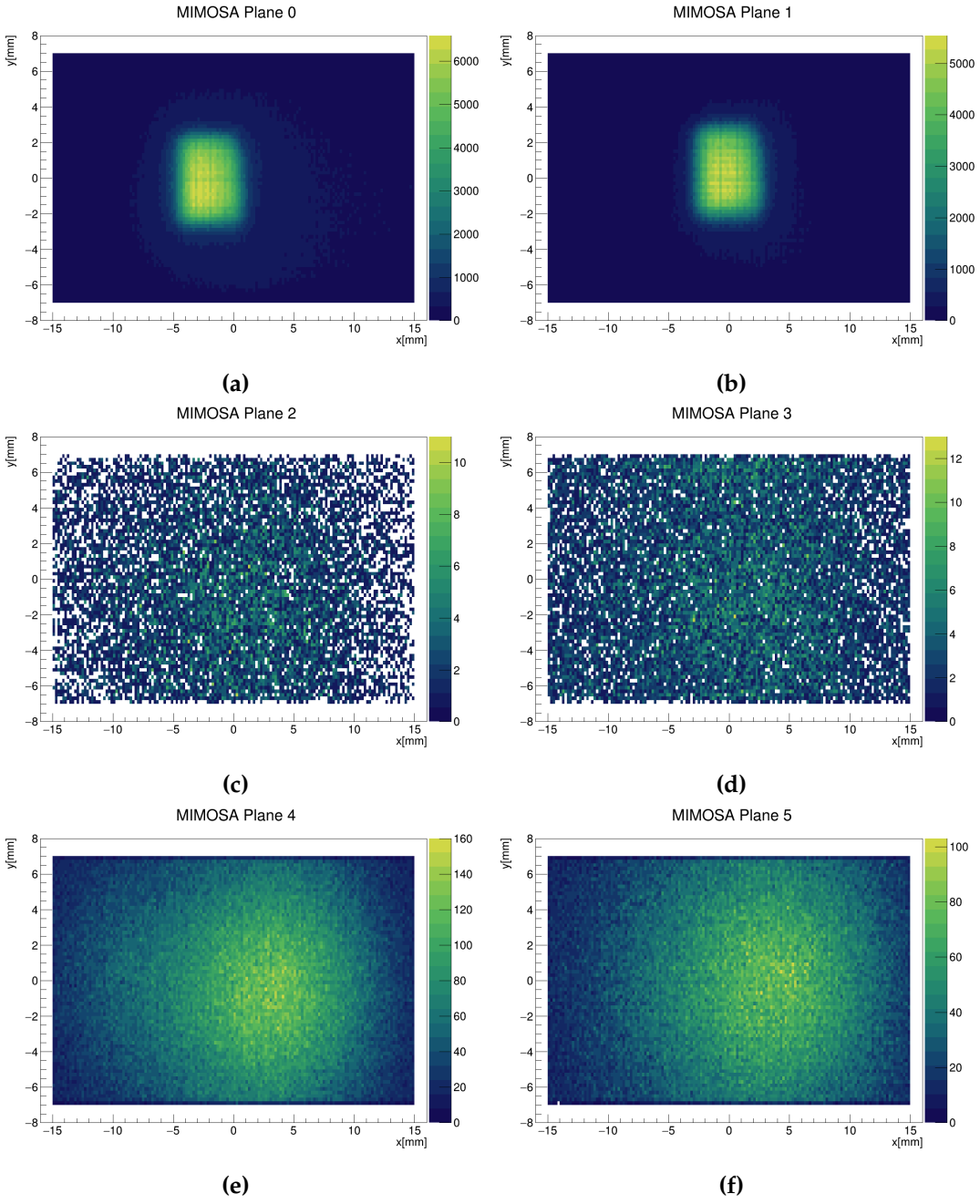

Figure 4.7.: Maps of hits in the MIMOSA detector planes for the full Bremsstrahlung test-beam dataset, after being cleaned for hot pixels.

z being the axis of the beam) of the first two planes at 178 mm, a misalignment in one of the parallel x or y dimensions of just 50 µm will return an angular discrepancy of 0.2 mrad – which is of the same order of the expected Bremsstrahlung beam divergence at 5 GeV.

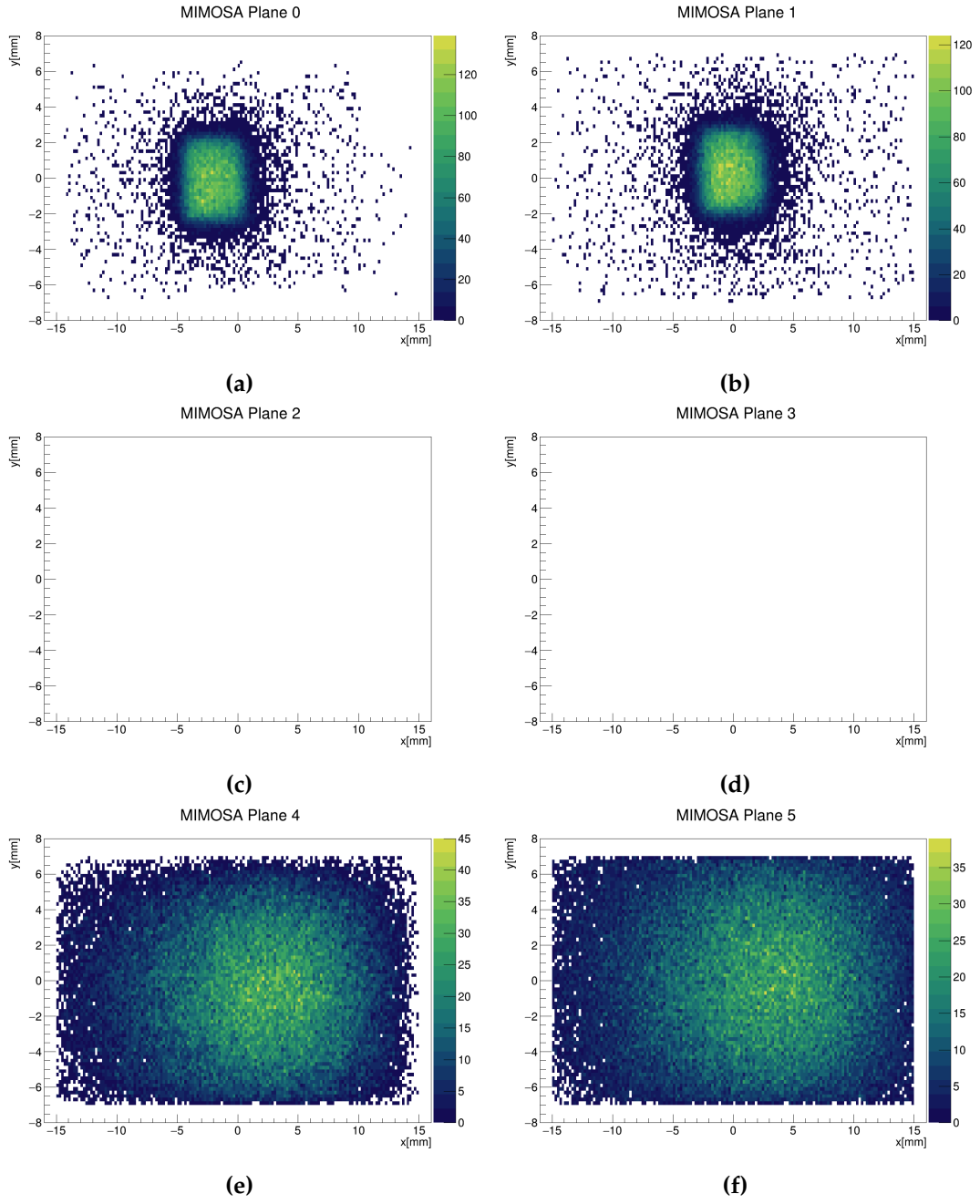

Figure 4.8.: Maps of hits in the MIMOSA detector planes for the full Bremsstrahlung test-beam dataset, after being cleaned for hot pixels and selection rules applied. Selection includes one hit in the first two planes each, none within the intermediate two detector planes, and one or two within the last two planes.

As there is a total of 7.54 m between the first two and last four detector planes, small-angle scattering through the air is a significant factor. An empirically-derived equation for the divergence of a charged particle beam due to multiple-scattering through small angles, appropriate in the low-density environment of a GeV-energy

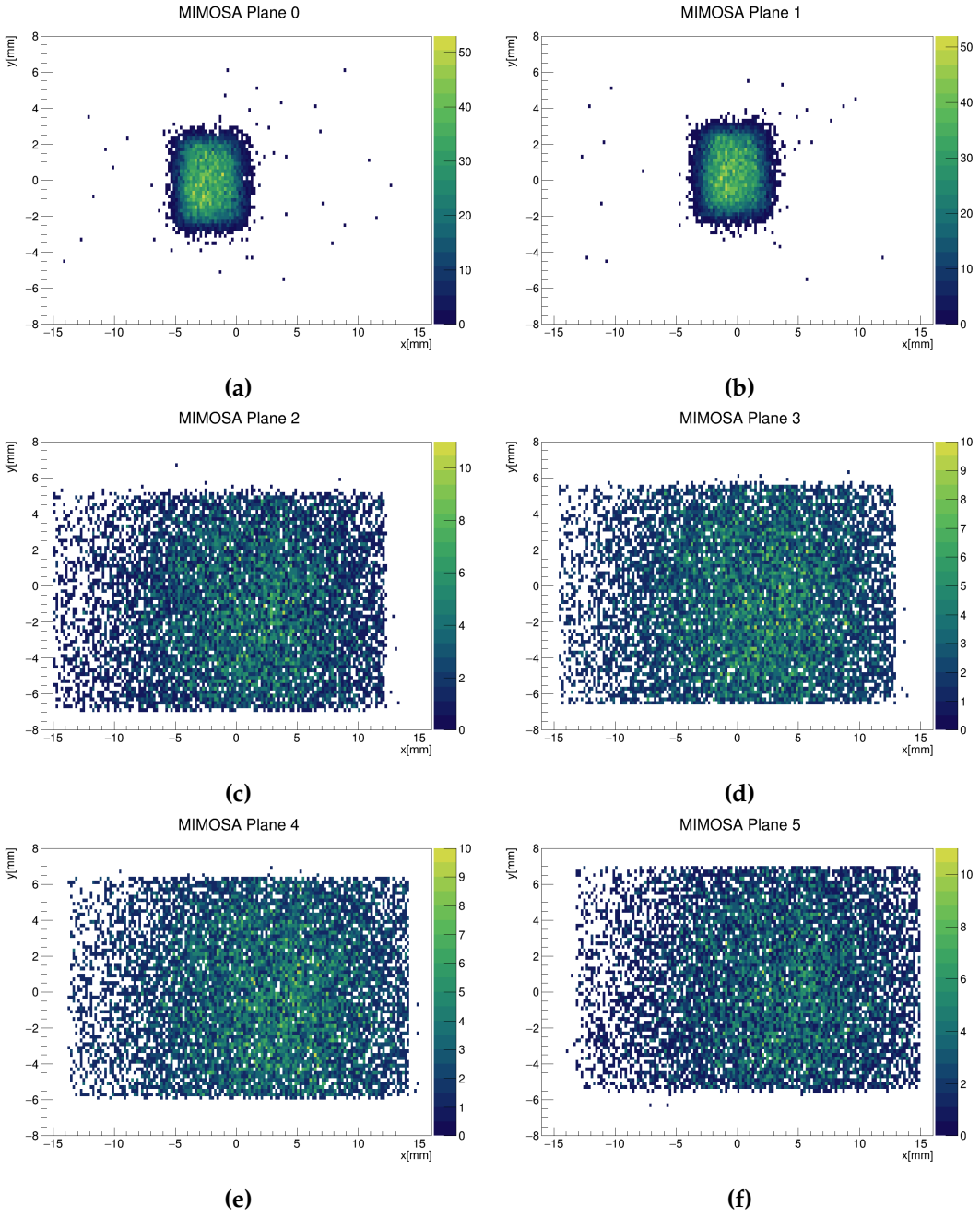

Figure 4.9.: Maps of hits in the MIMOSA detector planes for the test-beam alignment dataset, after being cleaned for hot pixels and selection rules applied. Selection requires one hit in each plane.

electron beam in air, is given by:

$$\theta_0 = \frac{13.6\,\mathrm{MeV}}{p\beta c} \times q\sqrt{x/X_0}[1 + 0.038\ln(xq^2/X_0\beta^2)] \tag{4.8}$$

where $\theta_0 = \theta^{\text{rms}}_{\text{plane}}$, the standard deviation of a Gaussian form which approximates the angular spread of the beam [49]. The β, p, q values are the velocity (as fraction of the speed of light), momentum and charge number of the travelling particle. X_0 is the radiation-length of the medium and x the path length travelled by the particle. This is applicable most of all within the central 98% of the distribution, as the true spread of the beam exhibits much longer tails around the edges. Computing the expected divergence for the test-beam setup here one returns a standard deviation value of 3.036 mm at a distance between the first and last detector planes.

Alignment is performed by scanning through the various free parameters for each plane. The dimension parallel to the beamline, the z axis, is not a free parameter, cannot be aligned and was measured in-situ, with appropriate uncertainty. The remaining parameters are:

- x, in the horizontal plane orthogonal to the beamline.
- y, the vertical axis.
- θ, rotation around the beamline z axis.
- ψ, rotation around the y axis.
- ϕ, rotation around the x axis.

For this analysis the residuals in each plane for the alignment dataset for a given set of alignment parameters were plotted in a histogram. The histograms were fit with a Gaussian function. A quality-of-alignment parameter was created, which is the sum of the mean value and variances of each of these fits, in both x and y dimension and for each plane. A scan was made through the data for each alignment parameter and a minimum of the quality-of-alignment found.

The variances of the fits of the residuals for just the last four planes, which are close to one another compared to the first two, should follow approximately the variance expected of the telescope detector system intrinsically. With reference to previous efforts in ascertaining the positional accuracy of the MIMOSA-sensor detectors [64], this is expected to be around 3.24 µm for the full six planes with negligible scattering due to air. Each of the resulting variances in one dimension of the last four planes in this analysis are below 10 µm, and the mean is measured as 5.57 µm. These are shown in Figure 4.10.

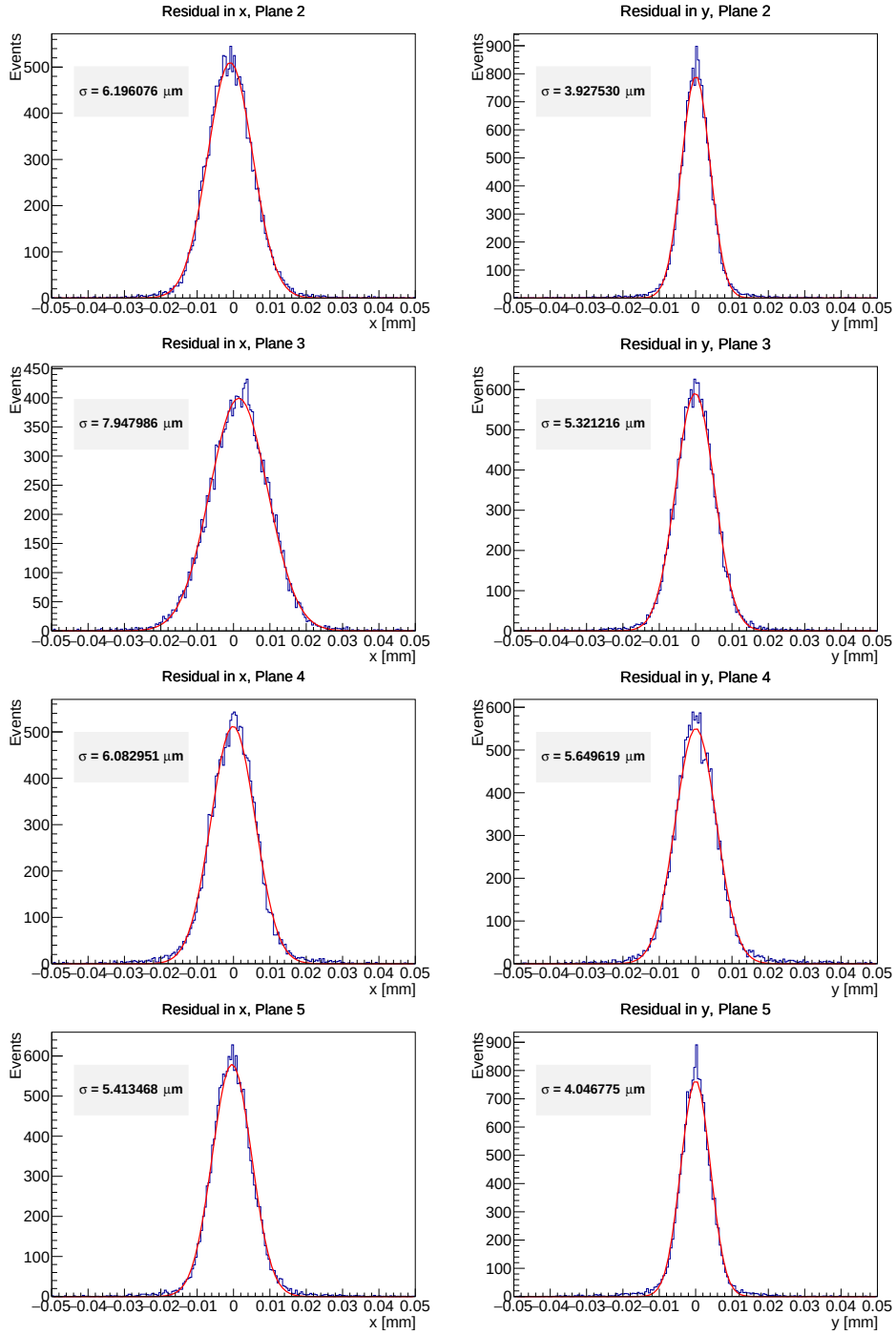

Figure 4.10.: Residuals for the last 4 detector planes in the x (left) and y (right) dimension. The best-fit solutions are calculated only with data from these last four planes.

The last four planes were aligned first, then kept constant while varying the alignment parameters of the first two planes in order to find a minimum in the quality-of-alignment.

Stray-Field Interference

Physical contraints of the test-beam setup were also present. There was limited space for the placement of the detector planes and tungsten target before the magnetic field used to separate the initial electrons from their radiated photons. The size of the magnet used means that when powered, a significant stray (or fringe) field is present. This is problematic in terms of tracking and reconstruction, as the goal is to have the initial electron take as straight a path as possible. The reconstruction of the initial electron vector is done by the particle hits recorded in two detectors at z=0, 178 mm. This is propagated to find the electron vector at the point of the Bremsstrahlung target, 233 mm downstream. At this point, due to the fringe field, bending of the trajectory has occurred. With knowledge of the dipole's field map, this bending can be calculated and accounted for, and so a more accurate initial electron vector recovered. A plot of the magnetic field strength is shown, along the direction of the beam (or z axis, in the test-beam coordinate system), in Figure 4.11. This includes many trendlines for various running currents. A setting of 300 A was used in this experiment, corresponding to around 0.3 T at peak field strength. As one can see from the plot, outside the physical start and end of the dipole (P.A. & P.E.), there is still a considerable stray field.

A photograph showing the initial electron setup, and in particular the proximity of the dipole to the telescope detectors and tungsten target, is given in Figure 4.12.

To include the stray-field's effects in the reconstruction, a field-map of the magnetic field was used. The field-map gave measurements of the y component of the B-field in increments of 20 mm. As will incidentally be shown later in this thesis (Section 6.2.1) in the context of electron spectroscopy with scintillation detectors, the bending of a relativistic electron in a magnetic field can be expressed using:

$$R = \frac{E}{qBc} \tag{4.9}$$

where R is the radius of turning in the field, q is the electron's charge, E is the particle's energy, B is the magnetic field strength and c the speed of light. Calculating this for each of the 20 mm increments of the field map, with the beam energy of 5 GeV, delivers a turning radius of the electron's path.

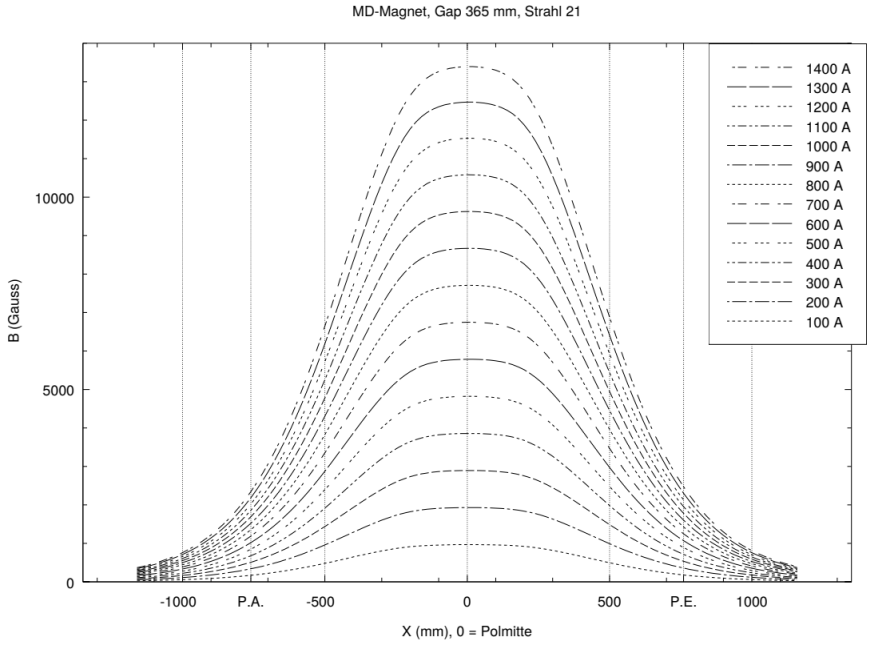

Figure 4.11.: The field strength for the 'Big Red Magnet' present in the TB21 beam-area [57]. Each trendline shows the values for a specific running current, shown in the legend. The initialisms P.A. and P.E. denote the beginning and the end of the magnet's coils, respectively, visible as a black solid in Figure 4.12.

With knowledge of the existing B-field, a function can be constructed to find the electron trajectory at the target. The function stitches together circular paths of differing radii. The radii are calculated from the B-field intensity (and particle energy fixed at 5 GeV) – the exact path is still subject to variable initial particle x,y positions and vector of momentum. Using this function a best-fit solution is made to the initial two hits in each of the first two detector planes, and then extrapolated to the position of the tungsten target.

After the Bremsstrahlung emission the propagation of the event thereafter is encapsulated only in the photon, which is unperturbed by B-fields, until the pair creation several metres away from the dipole which is no longer in the presence of non-negligible stray field. The B-field map is then no longer relevant for the reconstruction after the tungsten target.

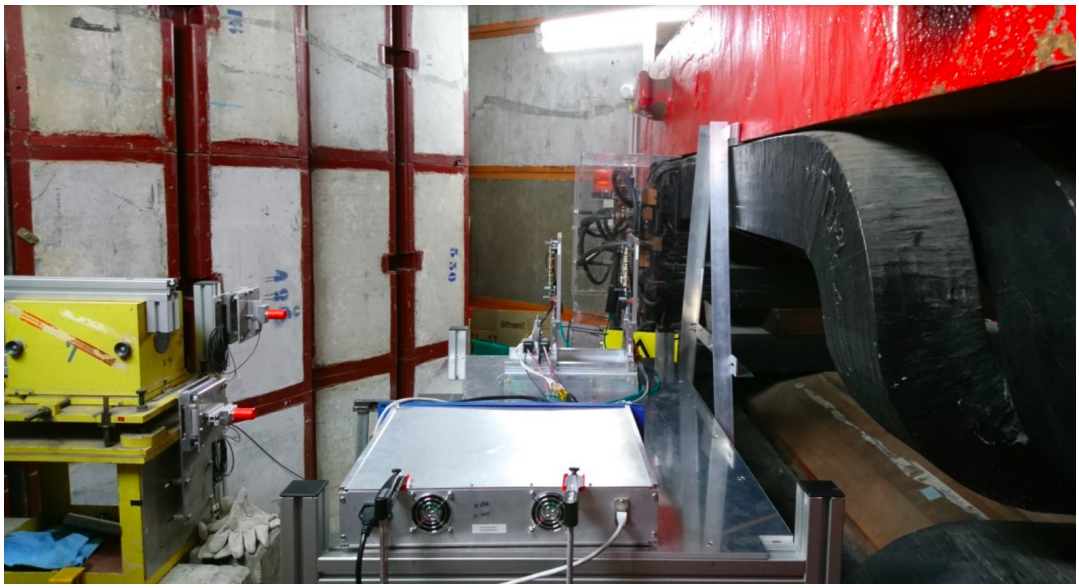

Figure 4.12.: A photograph of the initial electron region of the test-beam setup. The beam emerges from the left. The two detector planes are visible in the centre, and the thin tungsten target is flush to the edge of the magnet in a metallic frame.

4.2.3. Bremsstrahlung Analysis

Analysis with the objective of recovering the dispersion of the generated photon beam requires reconstruction of the event. First, the previously defined selection must be made. The telescope detectors are temporally responsive enough and work in conjunction with one another such that they can return 'events', where the results of the propagation of typically just one high-energy electron at a time is recorded. This is aided by the mechanics of the DESY-II test-beam, as when choosing for the comparatively high energy of 5 GeV the electron rate is at most 600 Hz depending on the conversion target and DESY-II running energy [65]. In this experiment, with the final size of the collimator and triggering scintillators, the effective trigger rate was measured as $\sim$34 Hz. The generation of one event was performed using the triggering of scintillators present along the beamline.

Almost all the events include detection of one hit, but only a small proportion of the total events, or initial electrons, are expected to contain the full hit-pattern as set out in Section 4.2.1. This proportion is seen to be just 0.8%.

A clustering algorithm was used to group the pixels together which had detected charge above their threshold. This included simply connecting all pixels which had a direct neighbour above threshold. The magnitude of the charge deposited is not

recorded with the MIMOSA detector – simply the binary condition of whether or not each pixel is activated. The algorithm returns a position in x and y of the detector plane, calculated as the 'centre of gravity' of the pixel cluster. This hit position becomes the best estimate of the position of the electron as it passed through the plane.

In order to complete the analysis, the trajectory of the Bremsstrahlung photon is reconstructed and compared to the mother electron track at the point of the Bremsstrahlung interaction. Reconstruction of the initial electron means fitting the three-dimensional stray-field function to the two hit points from the first two MIMOSA planes, and taking the tangent at the z-point of interception of the first tungsten target.

To reconstruct the Bremsstrahlung photon the two vertices of its creation and destruction are used to form a straight line. The first vertex is shared with the initial electron in the plane of the first metal target. The second vertex requires more detail; there are three types of event, differing only in the exact number of hits detected in the last two detector planes:

- The process is first described in the case of two hits in each plane. These are (assumed to be) caused by an electron-positron pair which again share a vertex with the Bremsstrahlung photon. Fitting two straight-line tracks from one hit each in plane 4 to one hit in plane 5 gives a tracking solution. The other combinatorial solution, where the hits in plane 4 are connected to the *other* hit in plane 5, is also computed. The trajectories are traced back in each case to the z-position of the centre of the lead conversion target. The displacement between the two tracks is calculated in each case, and the tracking solution with a smaller displacement is identified as the correct solution; if neither solution gives a displacement smaller than 1 mm, the event is rejected.

- In the case where only one hit is detected in plane 4, there is no combinatorial problem and the tracks are similarly reconstructed and their incidence on the plane in the centre of the target is calculated.

- In the case of only one hit in plane 4 & 5, only one track's incidence needs be computed.

In any case a single vertex of the annihilation of the Bremsstrahlung photon is required; this is computed using the simple mean in the x, y position of the two reconstructed tracks in the plane of the centre of the target; for the single-track case, the point of incidence is used directly. Figure 4.13 shows a diagram of this scheme.

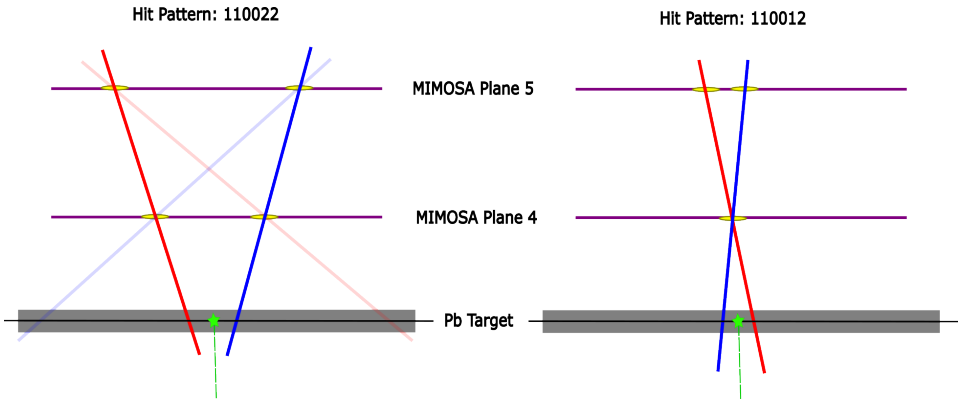

Figure 4.13.: A diagram of the tracking method used for reconstruction of the final lepton pair in the test-beam. Left shows the tracking for 2 clusters in each of the two last planes; right has one cluster in detector plane 4. The yellow areas denote activated pixel clusters, which have been used to reconstruct lepton tracks (red & blue). The inferior tracking solution is shown on the left in faded colours. The midpoint of the tracks in the target plane is used as the reconstructed Bremsstrahlung photon vertex (in green).

With the best tracks for the two particles (initial electron & Bremsstrahlung photon) reconstructed, the angle between the two tracks is calculated using the dot product of the unit vectors. With 51598 events processed, the resulting distribution of reconstructed polar angle of the Bremsstrahlung photons is shown in Figure **??**. The distribution is normalised such that the integral of the distribution is equal to one (where the units are radians). The distribution shown is significantly inflated in comparison to the theory expectation; to determine the effect of the detector and reconstruction process, we must make use of a Monte Carlo simulation to replicate the experiment. The result of the polar angle distribution of such a Monte Carlo simulation is shown beside in Figure 4.14. The method of using this simulation is discussed in the next section.

4.3. Comparison with Monte Carlo

There are two levels of Monte Carlo used for analysis. To make any meaningful comments on the underlying physics, an analysis of the divergence of the photon beam as generated by Bremsstrahlung at its instantaneous point of creation is performed. This was generated in GEANT4. The profiles of this polar angle, defined as the angle between the radiated photon and its mother electron at the point of emission, can be

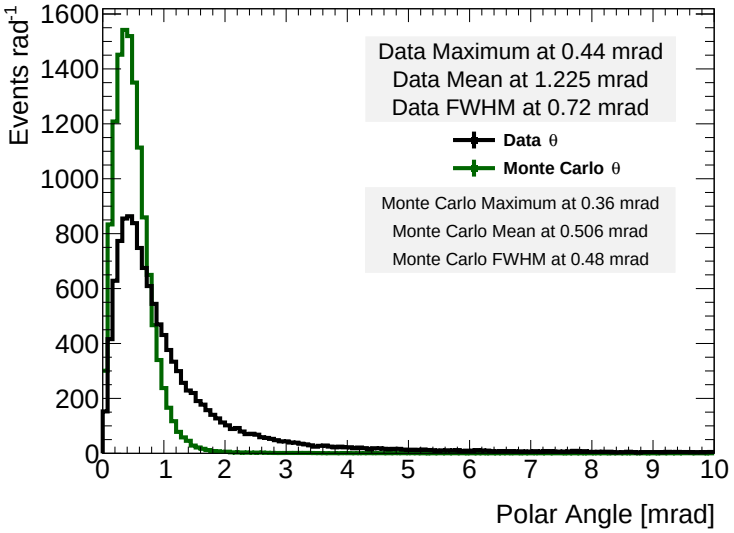

Figure 4.14.: The reconstructed distribution of polar angle of the reconstructed Bremsstrahlung interaction. The experimental data reconstruction is in black and green displays the Monte Carlo reconstruction. Key statistics of the distribution are also shown. Here and in the following distributions shown hereafter, those reconstructed from the experimental data are plotted in black, and the Monte Carlo data (including full detector effects) in a dark green.

fit with the approximative function used to generate them. This is Equation 4.6. The profile alongside two fits of this function are seen in Figure 4.15. The fit is imperfect when applied to the entire relevant range spanned by the histogram, as in 4.15a, but proves much more accurate when limited to an arbitrary interval between $\theta = 0$ and a point just larger than the full-width-at-half-maximum as in 4.15b. A discrepancy between the Monte Carlo simulation result and its generating function, seen to be localised to the tail of the distribution, is likely to be a result of the nature of the simulation, in particular where an electron radiates via Bremsstrahlung several times at differing energies, causing a small excess at higher values of the polar angle.

A straight comparison to the expected divergence of the Bremsstrahlung process alone would not be sufficient for this analysis. The resultant divergence of the beam is dependent on detector effects and the reconstruction process more than it is on the fundamental Bremsstrahlung photon divergence, expected in this energy range to be small. The operation of the detectors used, the MIMOSA sensors in beam telescope arrangement, as well as the actual process of the Bremsstrahlung mechanism followed by an induced pair production within a finite volume, must be simulated. In order to simulate the process selected here with this experiment, the beam-telescope

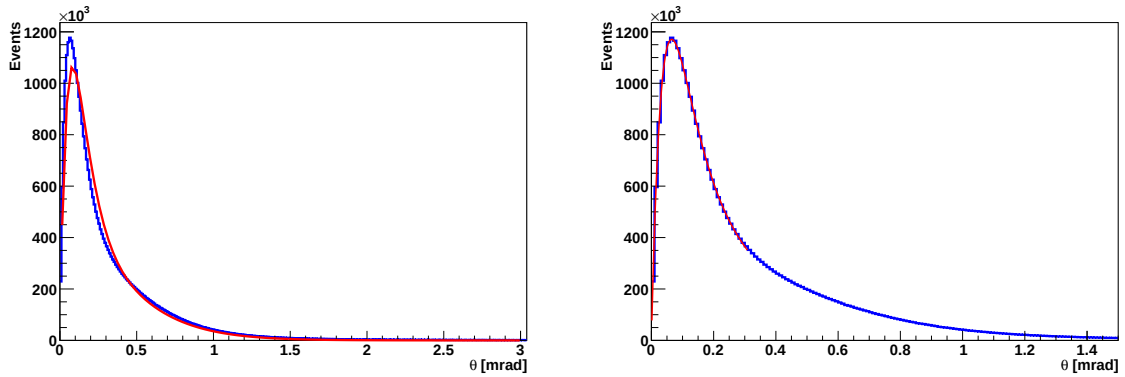

(a) **(b)**

Figure 4.15.: The polar angle, θ, of the photon beam generated by Bremsstrahlung in GEANT4. Data in blue and fitted functions in red. **(a)** shows the result of the fit of Equation 4.6 across the range of values in the histogram. **(b)** instead shows a fit for the region closest to $\theta = 0$, up to $\theta = 0.3$ mrad.

simulation Allpix^2 [66] was used. This gave a full simulation of the particle transport and other physics, using the GEANT4 framework, before a full account of the charge propagation and digitisation in the detectors and finally the clustering algorithm used in the experiment to recover particle tracks.

Within this context the experimental area was remade. Standard definitions for the density, atomic number and temperature of standard materials as defined by GEANT4 were used to calculate the scattering (explicitly simulating Bremsstrahlung, ionisation, pair production, etc.) within the targets and surrounding air. A pre-made model for the full operation of the MIMOSA telescopes was used. This included explicit modelling of the generation of charge from ionised particles within the detector, the propagation of the charge in an electric field, conversion of charge to digital signal, before a registering of activated pixels as charge over some threshold. Groups of neighbouring pixels were used as clusters, and the projected position of the initial charged particle hit was calculated using a centre-of-gravity approach, identical to that used in the clustering of the real raw data from the MIMOSA sensors. Figure 4.16 shows a visualisation of an event in the simulation at each of the two targets, and examples of patterns of clusters each generated from a single high-energy electron passing through. The vast majority of these clusters included a number of activated pixels fewer than five.

The distribution of reconstructed successful Bremsstrahlung event polar angles from this developed Allpix^2 simulation was shown in Figure 4.14, alongside the

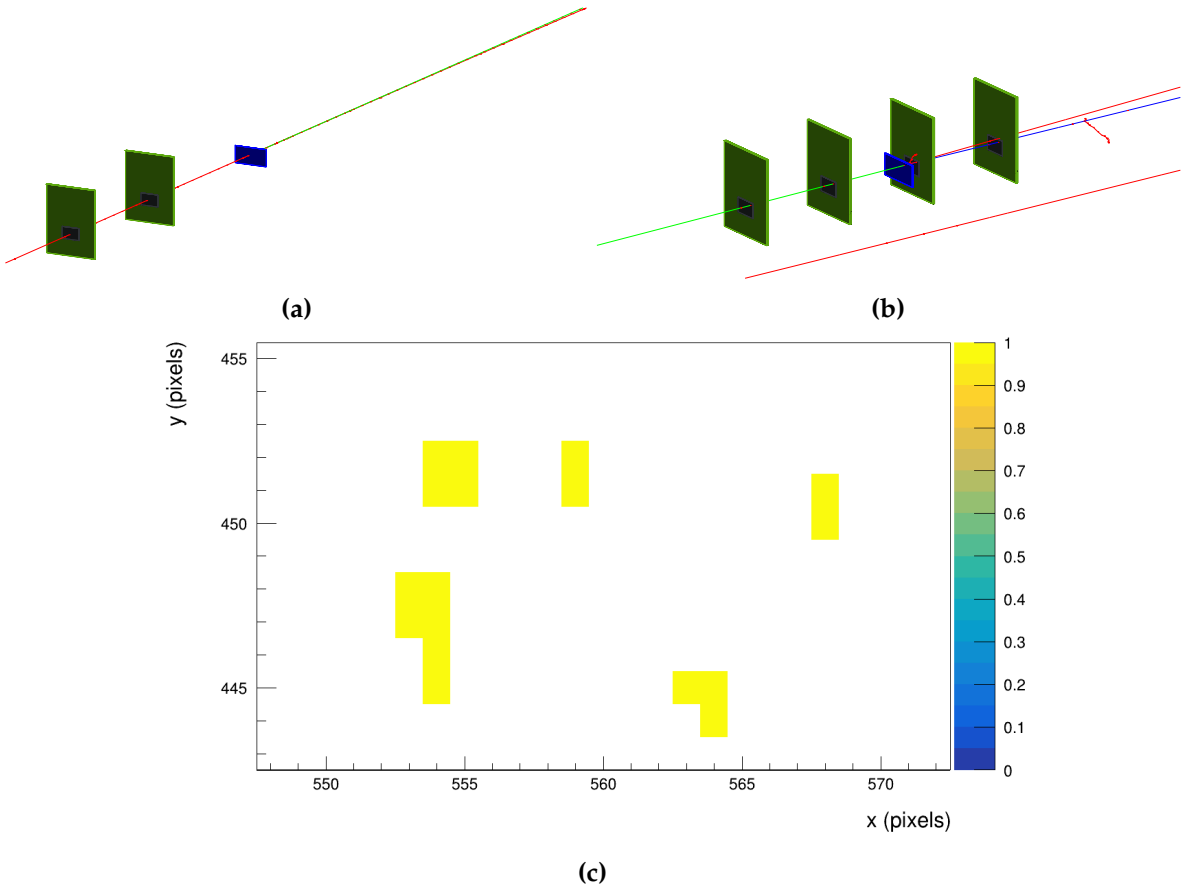

Figure 4.16.: **(a)** A visualisations of a successful electron-to-photon-to-pair event at the first two MIMOSA planes. **(b)** shows the latter four planes. The red traces are that of electrons, the photons are in green, and positrons blue. The MIMOSA planes are green and the heavy-metal targets blue. The B-field is simulated but not visualised here. **(c)** Shows typical cluster shapes / sizes for a handful of individual GeV-energy electrons.

experimental data distribution. The distribution of the polar angles from data is noticeably larger than that in the case of Monte Carlo. The shape too includes a longer tail in the real data, evidenced in the statistics by a large discrepancy in the mean values, but a smaller discrepancy in the maxima of the distributions. This discrepancy in the shape of the tails may be some artefact of the electron beam (the edges of which are trimmed with a collimator in the experiment) or features of multiple-scattering from the dumping of the beam. These were not recreated in the Monte Carlo simulation for computational efficiency. In light of the measurements to be performed by LUXE, which hinges on the flux very close to the very centre of the Bremsstrahlung beam, we may prioritise the small-angle region.

The distribution of the polar angle of the hits can also be displayed using the expression for the distribution normalised to unit area of the emitted beam. This is simply performed by weighting each reconstructed value by the denominator $1/(2\pi \sin\theta)$. This has the effect of systematically reducing the size of the larger-angle portion of the reconstructed distribution, which is actually useful for this analysis, as we try to focus on the maximum flux. These distributions are shown in Figure 4.17. Although the underlying true area-normalised polar angle distribution should follow the function of Equation 4.6 divided by $2\pi \sin\theta$, the reconstructed distributions (of data and Monte Carlo) are distorted enough that we instead fit with an arbitrary second-order polynomial. Using the fitted functions to reduce the effect of statistical fluctuations, the width of the distribution at half of its maximum value is calculated. Polynomial functions of greater order were also fit, but the resulting width measurements exhibited a higher variance, so the second-order fits were used for analysis.

In order to gather information on what the reconstructed data implies about the underlying variance of the Bremsstrahlung interaction, we use the width of the second-order polynomial fits at half of their maximum. By iteratively running the Allpix^2 simulation with an increased Bremsstrahlung interaction divergence, we can find the point at which this fit-width parameter matches that of the data. To control the Bremsstrahlung polar angle, an ersatz solution of a reduced beam energy is used, which results in an increased polar angle (roughly a $1/\gamma$ relationship). Because this analysis is not concerned with the rate of the interaction and only the polar angle, this is a reasonable emulation of directly changing the polar angle sampling of a 5 GeV beam. The energy of these ersatz-electrons are controlled to vary the photon divergence from simulation-to-simulation. The stray magnetic field experienced by the ersatz-electrons is corrected to preserve the geometric bending undergone by the 5 GeV electrons.

The reconstructed area-normalised widths are shown for varying Bremsstrahlung divergence (controlled by the electron energy) in Figure 4.18a. These are fit with a falling $1/E$ distribution. Using this function, the width of the fitted function of the data in Figure 4.17, 367 µrad, is matched at 3.0 GeV, or a relative 67% increase in the polar angle of the distribution. The reconstructed area-normalised polar angle from simulation using this modified divergence is shown in Figure 4.18b; this can be compared directly to Figure 4.17. The longer tail of the shape of the experimental data results in a larger mean of the distribution. Since the normalisation of these distributions are such that the total integral of the polar angle is equal to unity, we can

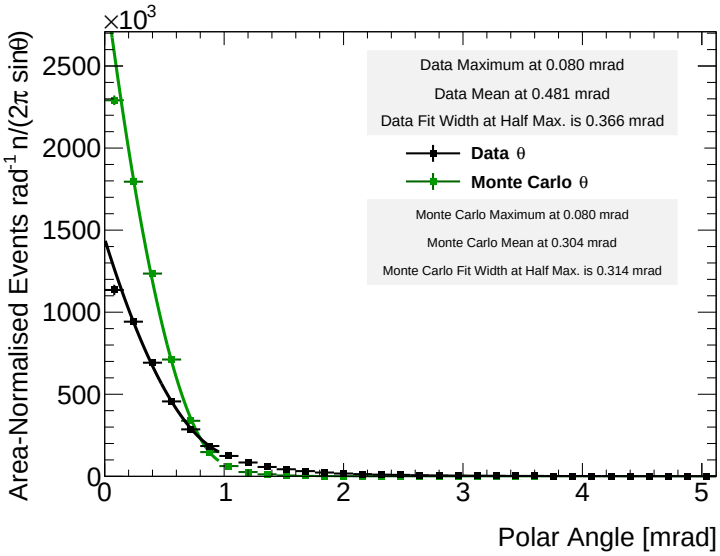

Figure 4.17.: The reconstructed distribution of polar angle of the reconstructed Bremsstrahlung interaction per unit area. Comparison is made between the test-beam experiment data and Monte-Carlo generated samples.

directly compare the values in the y axis, and see the maximum value for the Monte Carlo result is about 50% larger than the experimental data.

The discrepancy may one or all of detector effects, a sampling bias, or physics, which we cannot currently account for. For the following analysis, the worst-case-scenario for LUXE is assumed, which is that this is entirely due to error in the model as implemented in GEANT4.

4.4. LUXE Physics Sensitivity to Photon Beam

The LUXE physics sensitivity to the characteristics of the generated photon beam can be expressed in the number of electron-positron pairs produced via the Breit-Wheeler interaction. The yield of the electron-positron pairs per beam-laser bunch-crossing depends on the flux of photons overlapping spatially and temporally with the laser focus. This is then dependent on the angular spread of the photon beam but is also highly dependent on the energy profile of the beam. As shown, the data from the SLAC and CERN results [54, 55] concerning the energy profiles are consistent with the accepted theoretical model. Therefore, the flux of photons incident at the IP is directly proportional to the electron-positron yield per bunch-crossing. LUXE collaborators

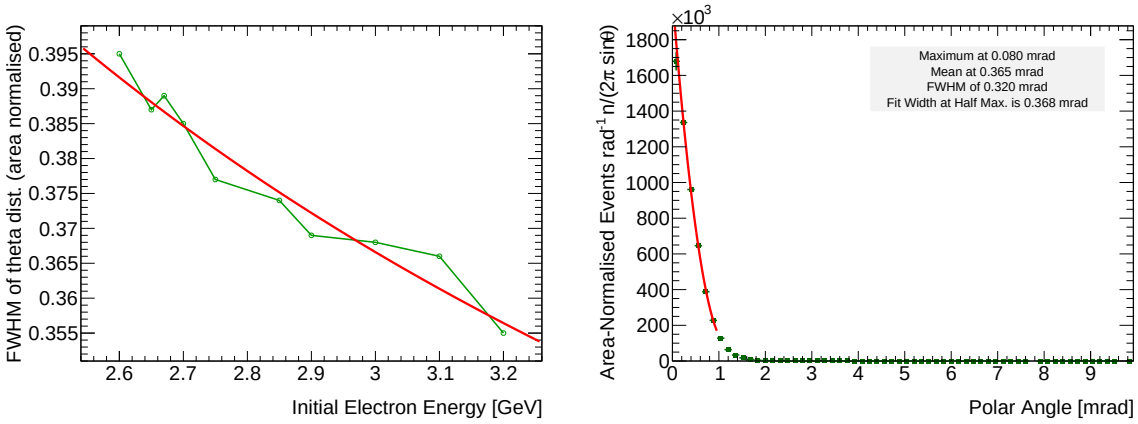

(a) **(b)**

Figure 4.18.: The reconstructed distribution(s) of polar angle of the reconstructed Bremsstrahlung interaction, from a modified Allpix^2 simulation used to inflate the Bremsstrahlung divergence, normalised to unit area.**(a)** shows a scatter-plot of the width of fits for varying Bremsstrahlung divergence, controlled by initial electron energy. **(b)** is the result of simulation matched to the data in terms of the width of the fit. This is the distribution of area-normalised equivalent to energy 3.0 GeV.

have used a Bremsstrahlung beam simulated by GEANT4 to project yields of positrons with the PTARMIGAN software. The electron-positron yield for a particular photon flux can be calculated from these results with comparison to the GEANT4 default. If one changes the Bremsstrahlung photon flux by some fraction, the resulting positron yield changes similarly. Assuming similar timing characteristics:

$$\frac{n_{e+1}}{n_{e+0}} = \frac{n_{\gamma 1}}{n_{\gamma 0}} = \frac{\int^{A_{laser}} j_1 . dA}{\int^{A_{laser}} j_0 . dA} \tag{4.10}$$

for positron yield n_{e+}, number of Bremsstrahlung photons within a cross-sectional area n_γ and relative photon fluxes of j. We use the 0 subscript for the GEANT4 default photon flux, and 1 to denote the flux as reconstructed from this experiment. In the LUXE geometry there is a distance of 7.5 m between the Bremsstrahlung target and the IP. The maximum size of the laser spot at the IP can be approximated as diameter 100 µm. This corresponds to $\xi = 0.15$ for the phase-0, JETI40 laser. Technically the laser spot can be further defocussed, especially if a run is desired with the phase-I laser with extremely low ξ. However the expectation, as per Figure 3.13, is that no detectable pair production will be observed at this magnitude. So, the estimate of the yield within a cross-sectional circle of the beam with radius 50 µm is used. This corresponds to a polar angle of 6.65 µrad.

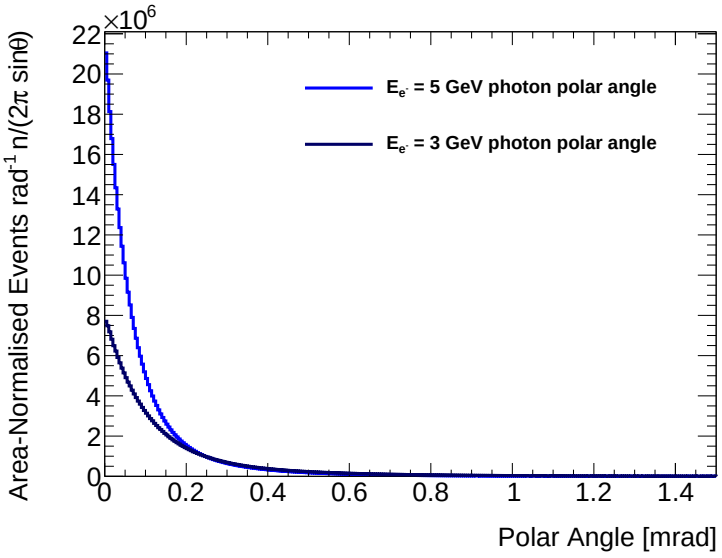

Figure 4.19.: The truth-level distribution of polar angle of the Bremsstrahlung photon interaction, as simulated by GEANT4, normalised to the cross-sectional area of the photon beam. This compares the 5 GeV Bremsstrahlung beam photons as simulated by GEANT4, to the ersatz photon beam which emulates the divergence seen by the test-beam experiment. This is implemented as a Bremsstrahlung beam produced from 3 GeVelectrons.

In order to calculate the relative flux implied by the reconstruction of the data, we use the distributions in Figure 4.19. These are the truth-level area-normalised polar angle distributions as simulated by GEANT4 for the theory-based divergence of Bremsstrahlung photons from 5 GeV electrons, and the inflated divergence implied from the reconstruction of the data. The decreased flux factor implied by the data is assumed to be constant up to 16.5 GeV. Arbitrary second-order polynomial functions are fit to the small-angle region smaller than 6.65 µrad. These can be integrated to find the best estimate of the proportion of the beam within a 100 µm-diameter laser spot. Expressing this function as $f(\theta)$, the integral is:

$$\begin{aligned} I = \int f dA &= \int_0^{2\pi} \int_0^{6.65\mu rad} f(\theta)\ \theta\ d\theta d\phi \\ &= 2\pi \int_0^{6.65\mu rad} f(\theta)\ \theta\ d\theta \end{aligned} \tag{4.11}$$

where ϕ represents the azimuthal angle. Since Bremsstrahlung has no preferential direction the emission is flat through ϕ. Performing the calculation, the data then implies a reduction of 63% of the peak photon flux from high-energy Bremsstrahlung

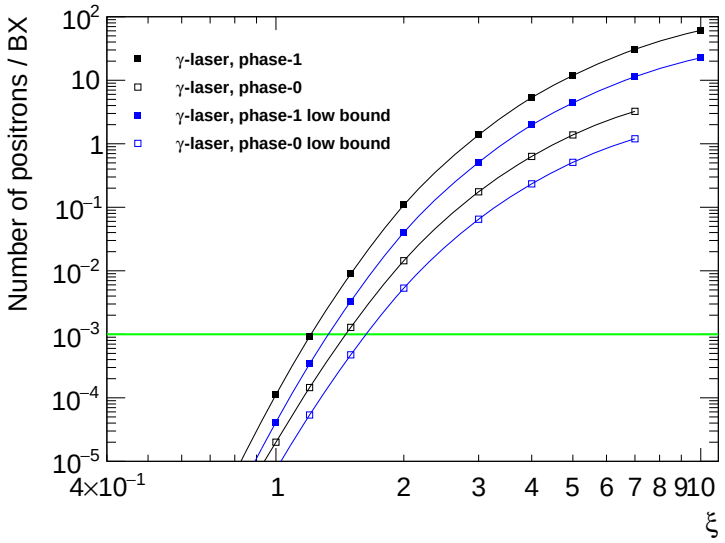

Figure 4.20.: Expected yields of positrons per bunch-crossing at LUXE for various ξ, with the lower bound limit implied from DESY-II test-beam data, for the LUXE γ-laser mode in both phase-0 and phase-I.

in comparison to the default model included in GEANT4. This means a 63% reduction in the positron yield which is shown in the following plot, Figure 4.20, an amended version of Figure 3.13.

From Figure 4.20 one sees the possible reduction in positron yields implied by this analysis. With the tracker detector expectation of being able to make significant measurements down to 10^{-3} positrons per bunch-crossing, the original and amended lower limit of sensitivity to Breit-Wheeler rate in terms of ξ in the γ-laser mode is made. Due to the very steep falling probability with changing ξ, even the reduction of 63% in positron yield means only a modest change of the lowest detectable limit of ξ from 1.47 to 1.65 in phase-0, and 1.21 to 1.34 in phase-I. These limits are 12.8% and 10.8% larger than the GEANT4-derived estimates in phase-0 and phase-I respectively. For comparison, the absolute relative uncertainty of the measurement of ξ from the laser diagnostics is expected to be $\pm 2.5\%$.

The data-implied rates are treated as a lower bound as the discrepancy between the reconstructed data and the Allpix^2 results have been taken to be entirely due to a problem with the theoretical Bremsstrahlung expectation. Qualitatively it can be said that the discrepancy is much more likely explained by some faulty assumption or inaccurate modelling of the experimental area and detection process. Upon the realisation of LUXE in full, the profile of the beam will be directly measured by the

Gamma Profiler defined in Section 3.4.3 on a shot-by-shot basis to have absolute confidence of the divergence of the photon beam. This analysis therefore presents an aspect of the more preliminary feasibility study for this γ-laser mode of LUXE.

4.5. Considerations for the Future

Reconstruction of the data proved to be difficult. The alignment of the sensors suffered from the fact that the six detector planes were arranged such that the first two planes were close to one another, and the last four were more than seven metres downstream of the first pair. This made aligning the first two planes difficult, and gave only two detector planes to reconstruct the initial electron. For just two planes a linear fit of two points can always be made perfectly, frustrating alignment between them. In comparison the latter four planes were all provably aligned with respect to one another well. The author then recommends, were the experiment to be repeated with similar goals and limitations, to use three planes at both the upstream and downstream locations of the beamline. This would enable good intra-alignment in both regions before the challenge of the inter-alignment between them. A greater separation in z of the first group of detector planes would also clearly be beneficial, but in the test-beam area space restraints prevented this.

The experimental setup also measured the energy of the generated photon, via the use of the calorimeter FCAL prototype. This can be seen in Figure 4.6, where the positron-electron pair produced in each successful event is then destructively measured in two (possibly overlapping) tracks by the calorimeter. This data was not used in this analysis as it is not clear whether including the data would meaningfully aid the analysis given the significant effort of calorimeter analysis. Finding the energies of single electron/positron tracks of order-GeV energy is difficult with such a calorimeter [67]. Were it performed, such an analysis does have the possibility of checking the assumption that divergence with respect to photon energy is constant, as well as checking behaviour in the very-high-momentum-transfer events, which are crucial for LUXE.

Chapter 5.

Scintillation Screen & Camera Detector System Design

This chapter explains the design of the scintillation screen and camera detector system in LUXE. After making clear the challenges of the detection in Section 5.1, the general design and principles of detection are shown in Section 5.2. This includes some graphics and indicative plots which come from GEANT4 simulations detailed later in Chapter 6. Section 5.3 then gives a detailed description of the components of the system and its exact geometry, with reference to material from the manufacturers of the various components.

The two regions this thesis is concerned with, the electron detection of the IP region of the e-laser mode (the Electron Detection System or EDS) and the gamma beam monitor region (the Initial Bremsstrahlung Monitor or IBM) of the γ-laser mode, exhibit similar particle rates and have similar requirements, and so can use almost identical detection systems. Although both may be installed at the same time, it is not expected that both operate concurrently.

As shown in Figure 3.6, the scintillation screen and camera system will be used in these two locations. In each case they are located several metres downstream (following the initial beam direction) from the SFQED IP or high-energy-gamma converter; they are also placed a few metres downstream from a constant magnetic field, which separates particles by charge and energy. The field lines are oriented such that GeV-energy electrons are incident on the screen. For the purposes of this thesis the two sites are considered separate from the somewhat similar setup in the downstream gamma spectrometer. Its particular needs and challenges, particularly a

lower flux of electrons/positrons, motivate the decisions made for it, laid out in its own technical report [68].

Mentioned within the LUXE Executive Summary [47] is the consideration, in view of the possibility of delay in assembling the detectors, that a minimal or 'next-to-minimal' detector layout of LUXE may be used. In brief, the minimal setup involves the use of only the scintillation screen & camera system and/or the Cherenkov detector, the already-existing CALICE calorimeter prototype and the backscattering calorimeter. These are used to measure the electrons, positrons, and photons respectively. In a next-to-minimal setup, a Silicon pixel tracker of 2-4 layers may also be utilised on the positron side. In either of these cases, or the full-LUXE case, the implementations of the screen & camera system(s) are identical and as described here.

5.1. Electron Detection Requirements

5.1.1. Electron-Laser IP Electron Detection System (EDS)

In the Interaction Point (IP) of LUXE (e-laser mode) the highly focussed electron beam of the EU.XFEL is directly collided with an intense laser pulse. The beam, having interacted with the strong field, then transforms from a mono-energetic electron beam to electrons which follow some spectrum of energy as seen in Figure 5.1, where the particles remain largely collinear. They are then separated from photons and positrons by the dipole spectrometer magnet. This magnetic deflection is approximately inversely proportional to the energy of the charged particle, creating a plane of GeV-energy electrons.

The high-intensity Compton scattering mechanism results in a much lower rate of low-energy electrons compared to the high-energy end of the spectrum. The acceptance of any detector system, constrained by the opening angle of the magnet, restricts the lower bound of any detector acceptance to approximately 2 GeV. This covers the full spectra shown in Figure 5.1, roughly representative of all expected spectra from beam-laser interactions in LUXE.

Achieving detection of the full spectrum up to the highest energy possible – but without running risk of intercepting the unscattered beam directly – and so recovering the non-linear Compton interaction rate is required. Electrons created from the rarer

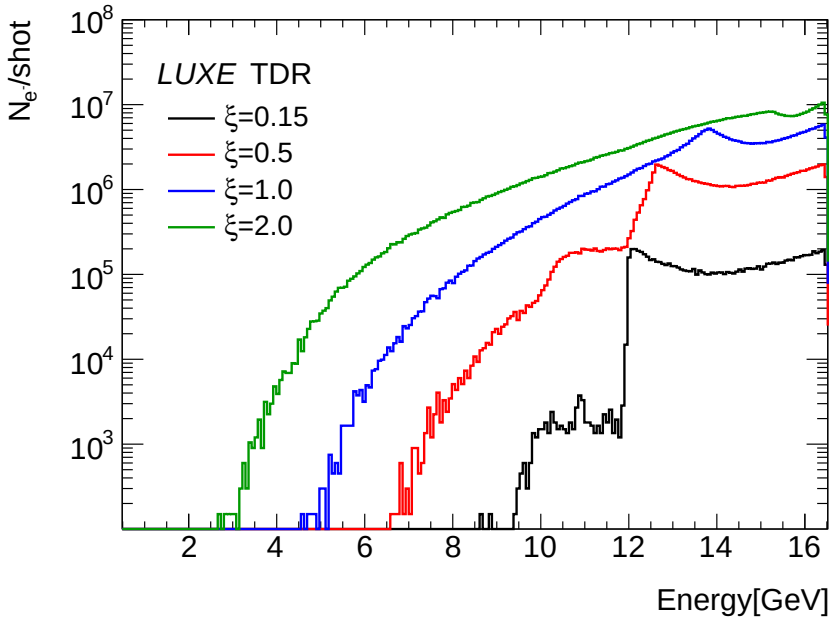

Figure 5.1.: Examples of the expected outgoing electron spectra for a single LUXE interaction. These are created using the PTARMIGAN Strong-Field QED simulation [48]. The initial beam energy is 16.5 GeV with bunch population of 1.5×10^9, the LUXE baseline.

trident process (in which a multiphoton Breit–Wheeler interaction has occurred) in the IP are also present, but are not expected to be resolvable above the signal resulting from the Compton-scattered electrons. This is because the lower rates, lower mean energy and greater divergence of these trident electrons results in a much lower flux. The trident process is instead observed by positron detection, which is symmetrical in terms of distributions of kinematics to these electrons. In the γ-laser mode a two-sided measurement of the electron-positron pair is performed, but not with the scintillator screen & camera system, as is seen in Figure 3.6.

Detection is also required of the Compton edge, a feature in the energy-spectrum, meaning a system is required with accuracy in reconstructing both total incident flux and absolute energy. The behaviour of this Compton edge is explained in Chapter 2. The requirement of the edge detection is defined as 2% uncertainty of the reconstructed edge energy – this is approximately the resulting uncertainty of the Compton edge position due to uncertainty of $\pm 5\%$ in ξ from the laser diagnostics. Simulated measurements of this accuracy, alongside the expected Compton edge transformation (with a ξ uncertainty of $\pm 2.5\%$), were shown in Figure 3.12b. The problem of measuring this edge is exacerbated by the variance in ξ present from the laser focus at

higher ξ_{max}, making the the edges appear smeared. To estimate the ξ_{max} achieved, finite-impulse-response filters will be employed [69]. To do this as effectively as possible requires fine energy (and therefore position) resolution. An analysis including this technique is presented in Chapter 6. Finally, detectors must be used which will remain tolerant to the level of radiation present, and remain cost-effective.

5.1.2. Gamma-Laser Initial Bremsstrahlung Monitor (IBM)

The second site using the screen and camera system is the IBM. Monitoring the generation of both possible sources of the γ-laser mode (Inverse Compton Scattering (ICS) and Bremsstrahlung) can be achieved using the deflected electrons used in the generation of the photon beam. In both production modes electrons from the same EU.XFEL beam radiate photons. By measuring the electron energy spectrum, and with good knowledge of the beam energy, the photon spectrum can be recovered in the ideal case of electrons radiating only once, using conservation of energy:

$$E_{\gamma} = E_{beam} - E_{electron} \tag{5.1}$$

This is only measurable within the range of the electron beam energy minus the detector acceptance energy limits. There is a subtlety in the fact that one electron can radiate multiple times. For both the Bremsstrahlung and ICS modes, the distribution of these multiple-emission events and the effect they have on the final spectrum, and therefore how to unfold the electron measurement to reconstruct the final photon energy spectrum, will be ascertained through simulation. For Bremsstrahlung, GEANT4 provides profiles of the expected rates of multiple-emission – which comes with associated errors. For this reason the accuracy of the detection is limited, and the most precise measurement of the initial photon energy profile comes from the downstream suite of photon detectors, and the purpose of the scintillation screen and Cherenkov systems is as complement to the downstream detectors and to act as a shot-to-shot beam-laser interaction quality monitor.

The full spectrum of electrons emerging from a 35 µm tungsten plate within the γ-laser mode, with the comparison of the level of multiple-emission Bremsstrahlung radiation events and electrons created from other sources, has been simulated with

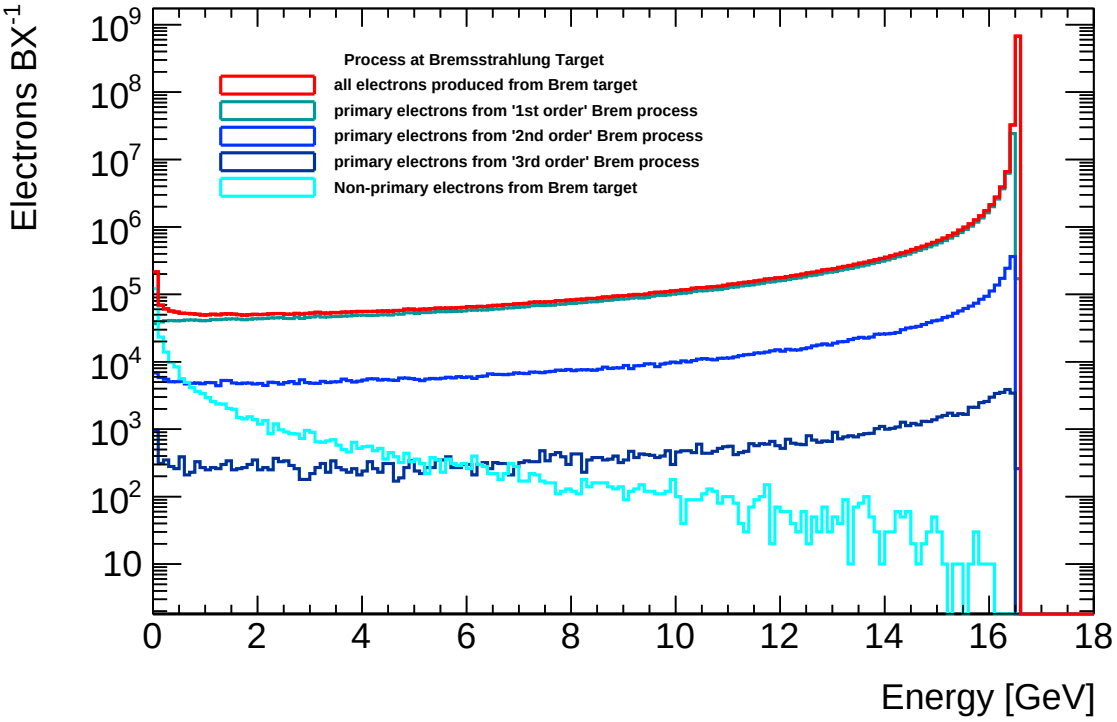

Figure 5.2.: Energy spectrum of electrons after the EU.XFEL beam at 16.5 GeV has passed through a 35 µm tungsten target, simulated in GEANT4. This simulation uses the standard LUXE EU.XFEL beam parameters (see Table 3.1). The total spectrum is softened compared to the ideal single-emission Bremsstrahlung case. A 'first-order' Bremsstrahlung event is defined as the case where a beam electron has radiated via Bremsstrahlung once, a 'second-order' Bremsstrahlung event has the same electron radiated twice, and so on.

GEANT4 and is shown in Figure 5.2. The proportion of the electrons which are first-order Bremsstrahlung electrons (which have radiated only one photon) between 2 GeV and 16.4 GeV is approximately 90%.

5.1.3. Electron Flux and Radiation Environment

Linearity in the response of the scintillation for a large range of fluxes, spanning several orders of magnitude, and one order of magnitude in electron energy, is useful for making a high-quality measurement. Chosen detector technologies must therefore be sensitive to the lower end of this range, but resistant to damage from the radiation environment associated with the higher end, and linear, or at least predictable, in their response throughout the range in flux.

The active elements of any detector in these regions need to be highly resistant to radiation damage, as the accumulated flux in either region is appreciable and accumulates as runs of data-taking progress. Alternatively elements at risk of damage could be replaced regularly, but only if this is enabled by the design of the detector. Observed in simulation, the dominant source of active detector element irradiation includes an approximate maximum flux of GeV-energy electrons of $\sim 10^8\,\mathrm{mm}^{-2}$ per bunch-crossing in the EDS. There is also a persistent neutron flux, which induces the possibility of damaging electronic elements even if they are not within the beam-plane. The details of this problem are discussed more in Section 5.3.2.

5.2. Scintillation Screen & Camera System Overview

The physical mechanism of scintillation is the response of a sensitive material to the deposition of energy by ionising radiation. Some fraction of the deposited energy is absorbed by a characteristic process, particular to each material, but consistent in the empirical consequence which is the emission of light. This release of light occurs some short time after the deposition, typically taking nano- to micro-seconds to occur.

These properties make scintillating materials very common elements in particle detectors. For LUXE the flux of ionising radiation is intense enough such that the intensity of light emitted is very high, and can therefore be imaged remotely. This offers the advantage of keeping the sensitive electronics outside the path of the direct radiation. With a relatively thin screen oriented such that the normal of the surface is aligned with the direction of incoming ionising particles, the position of the particle passing through the plane of the screen is given by a near-point-like emission of light – within the inherent position resolution of the deposition of energy and optical point-spread-function of the screen.

The material chosen for the LUXE detector is the high-light-yield scintillator Gadolinium Oxysulfide, doped with Terbium. This material exhibits a very high light output, around 70,000 photons per MeV absorbed energy; a density of $7.32\,\mathrm{gcm}^{-2}$; and a very slow time constant ≈ 600 µs. The slow light emission is helpful, as the camera exposure opens shortly after the beam-trigger. The fact that the screen is very thin means that, despite the higher density, the high-energy electrons typically pass through having lost very little of their energy. The low impact on the electron energy spectrum means it can be placed before the Cherenkov detector, the detection

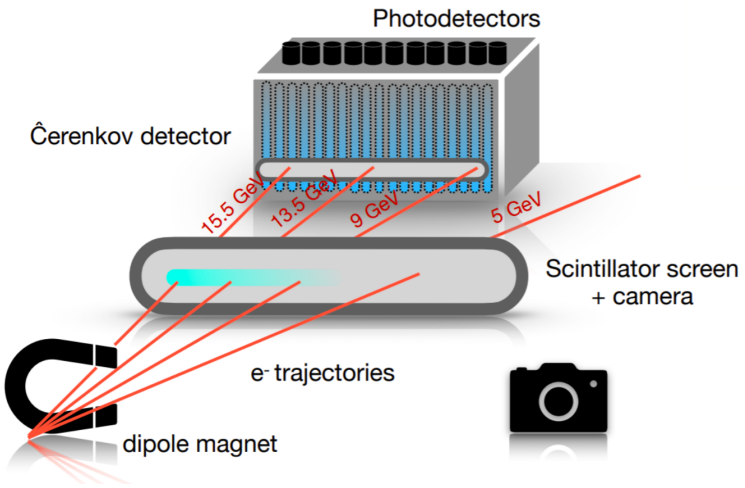

Figure 5.3.: An illustration of the scintillation screen and Cherenkov detector subsystems at the EDS site of LUXE [1]. Besides the particular energy labels, the schematic is also illustrative of the IBM site of the experiment.

mechanism of which remains unperturbed [70]. An illustration of these two detectors and their position with respect to the deflected electrons is shown in Figure 5.3. Using optical cameras means this light can be used to reconstruct the energy distribution of incident particles: with good knowledge of the field map of the deflecting B-field, the energy of the particles correlating to each position is calculated and the spectrum of energy reconstructed.

In both sites in LUXE, the electrons to be reconstructed (immediately after the interaction but before the dipole) are highly collinear. Both intended sources of electrons are from the focussed EU.XFEL beam having undergone one or more emissions of photons. The beam energy – typically between 14 and 16.5 GeV– means the Lorentz factor of the beam electrons is of order 10^4 and so their frame is highly boosted. The dispersion (orthogonal to the bending via magnetic field) of these electrons is a few millimetres (dependent on their energy) over the travel distance of around 1-3 m between IP/gamma target and the screens in each respective site. This results in the signal being contained within a central band on the screens. Extending the screen surface beyond this band in the y[1] dimension allows for some measurement of a more ambient background not confined to the central band. Evaluation of this 'quiet' part of the screen allows for background measurement and subsequent subtraction for clean

[1]The general LUXE coordinate system is seen used in Figure 3.6. There the z axis is for the initial electron beamline and the x axis is the orthogonal horizontal direction into which the screen extends in the EDS. The y axis is orthogonal to both.

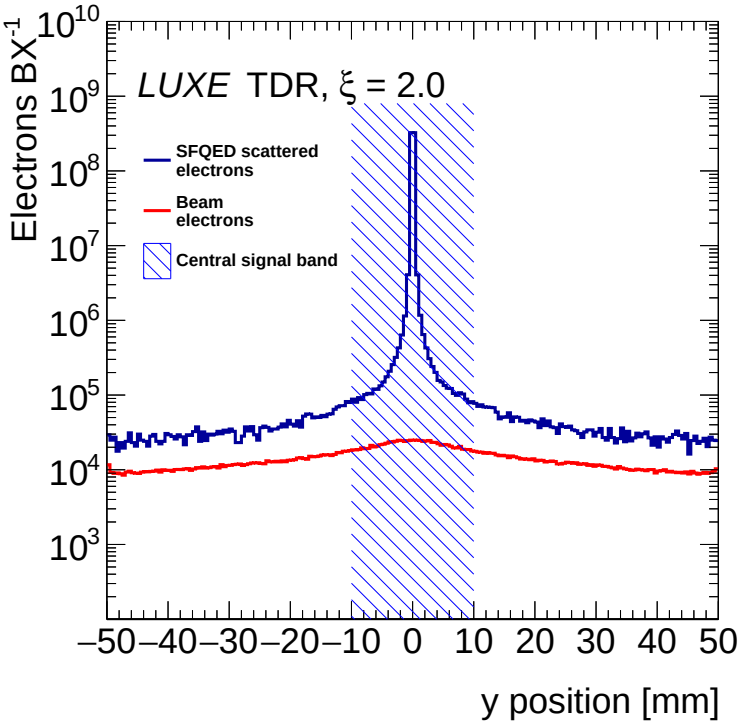

Figure 5.4.: Distribution of electrons in y in the scintillation screen in the EDS for a sample interaction with IP $\xi_{max} = 2.0$. Contributions to the signal coming from scattered electrons at the IP (blue) and from the un-scattered 16.5 GeV beam (red) are identified and shown. The beam is aimed such that it misses the screen, and so those electrons which do impact the screen necessarily have undergone unusually hard scattering in the environment.
The signal measurement includes secondary electrons and significantly deflected primary electrons from the environment in GEANT4. The central 2 cm band is used for final measurement and the signal on either side used to make a subtraction of background.

signal measurement. This is illustrated (using PTARMIGAN and GEANT4 to simulate the signal and its dispersion) in Figure 5.4.

As described in Chapter 3 and detailed within the general LUXE documents [1], signal bunch-laser collision events are planned to occur with a rate of 1 Hz, and beam-only[2] events for a further 9 Hz, to make a total of measurements at a rate of 10 Hz. The system is then designed to cater for a 10 Hz rate. Each camera's exposure is opened upon being triggered by the accelerator, upon the arrival of an electron bunch - alongside the laser or not. These beam-only events allow for background measurements fit for subtraction from data after signal collisions. The cameras chosen,

[2] In this case and hereafter, beam-only refers to the unscattered *electron* beam.

detailed technically later in this document, come from the Basler Area Scan range [71]. These present a quality position resolution, particularly when choosing multiple cameras to observe one screen, a high quantum efficiency, a dynamic range each of 12 bits (or 4096), an imaging frequency satisfactory for the 10 Hz required, and a comparatively low cost. The dynamic range of the combined system with both cameras exceeds 12 bits (shown in Chapter 7).

The lenses fitted depend on, and inform, the working distance between the screen and cameras. This distance is chosen on balance between the competing needs of being close enough to gather enough light, but not too close as to suffer radiation damage and have image of the screen warped by perspective issues (associated with lenses of small focal lengths and short working distances).

Optical filters are fitted to the camera lenses to accept only light within a tight waveband including the characteristic emission wavelength ($\sim$545 nm) of the scintillator material, in order to exclude as much as possible ambient light within the experimental hall. The hall cannot be left in complete darkness, as safety lighting is necessary. These safety lights can be chosen for monochromatic emission outside the wavelength of the screen, and so optically blocked by filters. Such filters are available with optical transmission lower than 99.9% for wavelength outside the desired waveband [72].

For both of the detector components (screen and camera) accurate positioning and orientation is of paramount importance. To keep each of the screens stable and free from sag, a precisely machined aluminium frame will be created to rigidly hold the screens, which are themselves fixed to an optical table alongside the Cherenkov detector. Aluminium is chosen as a compromise between hardness and low density to minimise environmental scattering. For the EDS measurement, as the screen is fixed extremely close to the EU.XFEL beam, a small loop of the frame is extended to enclose the beam but maintain stability on this side – this particular feature is shown in Figure 5.5.

The cameras are held within lead shielding to help protect from stray radiation. This lead shielding also assists in heat dissipation and therefore minimises electronic noise. They are secured mechanically to their mount by fixing both the lens and camera. Figures 5.6 and 5.7 show visualisations of the geometries of the screens, cameras and supporting structures in each of the two sites.

A high linearity of response from the scintillator is expected. Although the deposition of energy within the thin screen is stochastic in nature and varies electron-

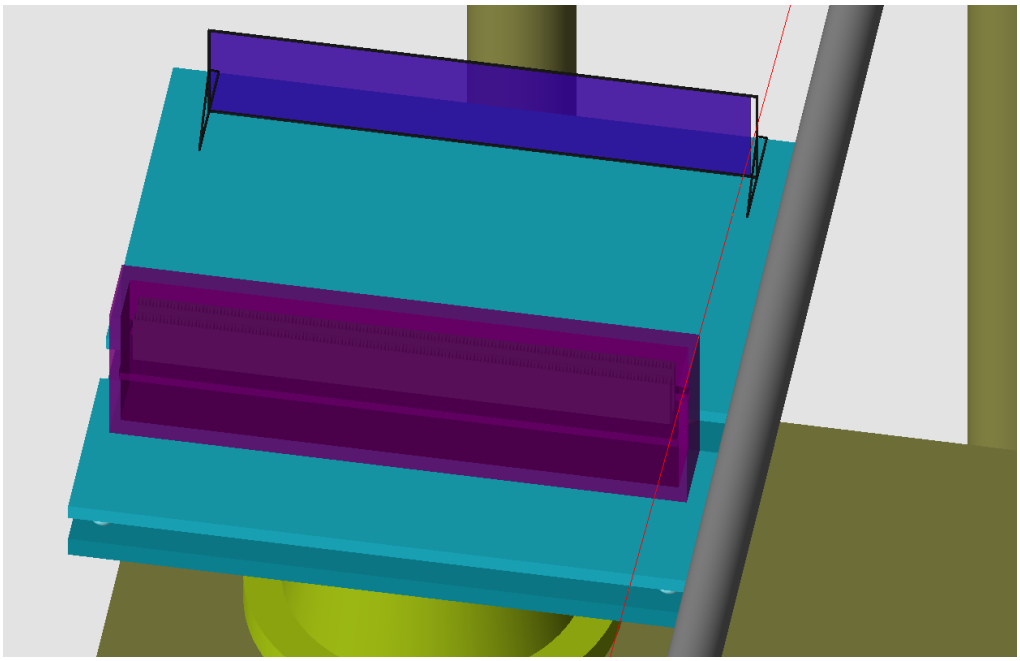

Figure 5.5.: A GEANT4 visualisation of the EDS scintillation screen (dark blue) and Cherenkov detector (purple) with a traced path of electron beam in red. They sit upon an optical table (light blue). The beam passes through a loop in the aluminium frame holding the screen.

to-electron, the energy deposited per electron converges to a mean for high statistics/fluxes. This has been explicitly simulated in GEANT4, detailed later in this thesis, where good linearity is shown for the fluxes expected to be measurable by the screen. The linearity of the CMOS-sensor cameras, minus expected backgrounds/electronic noise, is seen in Section 5.3 and the documentation [73,74].

5.2.1. Magnetic Action

The setup of the electron detectors at both sites of the experiment use magnetic fields to separate the particles by charge. The magnetic deflection of these charged particles is dependent on their energy, forming a magnetic spectrometer. The relation between energy and position of particle incidence upon a screen is used to reconstruct spectra by energy. The particles' movement traces a circular path in the magnetic field with radius of curvature $R = E/qBc$. From this an expression for the theoretical hit point (in x) within a detector plane rotated by θ, as seen in Figure 5.8, is derived:

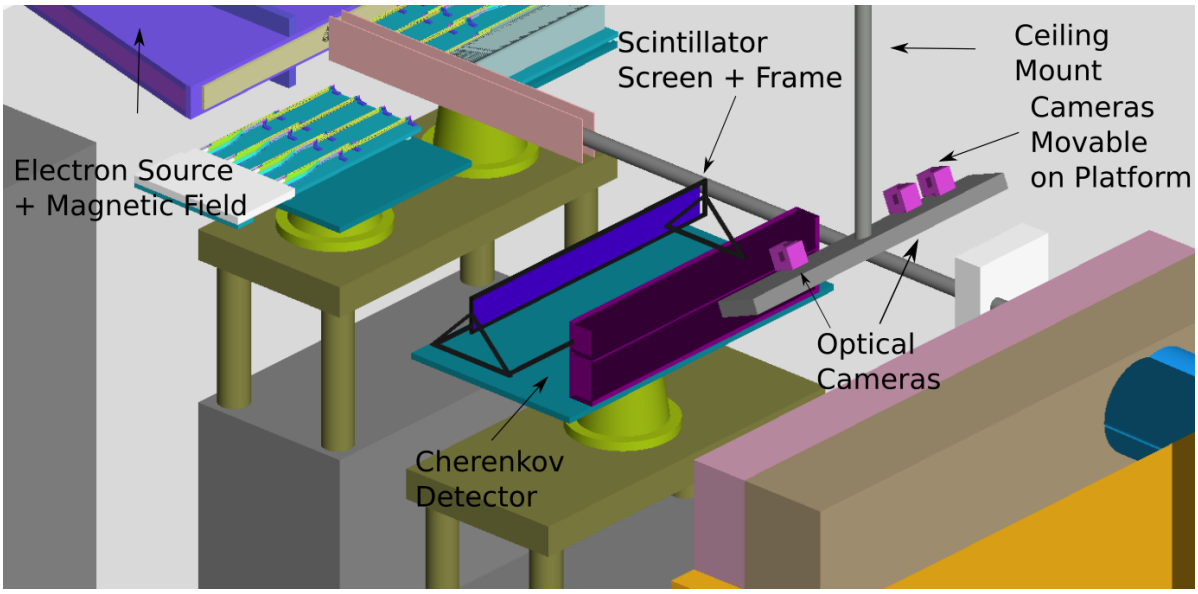

Figure 5.6.: A GEANT4 visualisation of the EDS region set-up of the electron detectors, in particular the scintillation screen and cameras.

$$x_1 = R(1 - \cos(\phi)), \tag{5.2}$$

$$x_2 = \tan(\phi) z_d, \tag{5.3}$$

$$x_3 = \frac{\tan(\theta)\tan(\phi)(x_{\text{detector}} - x_1 - x_2)}{1 + \tan(\theta)\tan(\phi)} \tag{5.4}$$

Where the final x-position is the sum of x_1, x_2, x_3 and ϕ is equal to $\sin^{-1}(z_m/R)$. This derivation and more details are present in Chapter 6. An approximate function of how the energy maps to the x position, for some standard parameters of the EDS site, is given in Figure 5.9a. Additionally, in Figure 5.9b there is a plot of the scintillation light profile (in x) in the EDS region for a signal e-laser interaction of $\xi = 2.0$. The shape of this light profile is equivalent to the electron energy distribution at $\xi = 2.0$ seen in Figure 5.1 transformed to position-space using the function in Figure 5.9a. As a result at the high-x position there is a double-peak feature – the lower-energy peak being the Compton edge.

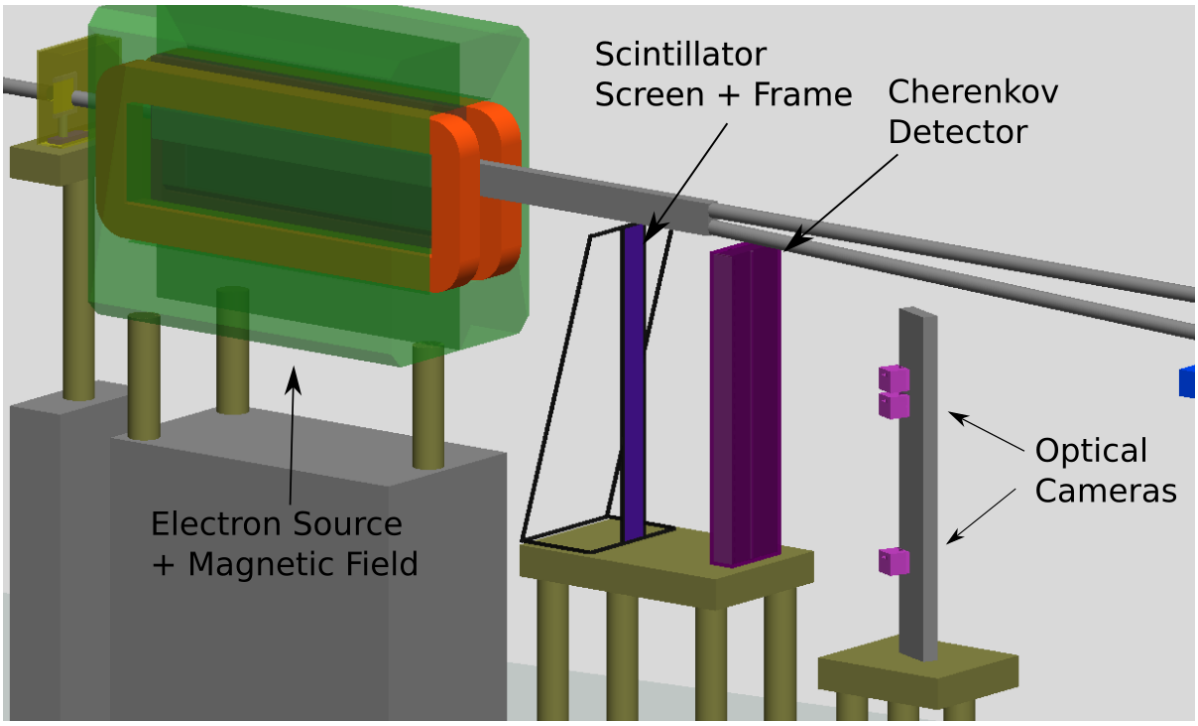

Figure 5.7.: A GEANT4 visualisation of the electron measurement set-up of the IBM detectors, in particular the scintillation screen and cameras. As can be seen here, and in contrast to the EDS region, the deflection of electrons is into the y direction of the general coordinate scheme of LUXE.

As the electrons exit the beampipe, the beampipe wall can cause considerable scattering, especially when they approach at a shallow angle, producing background interference and reducing the quality of the signal. To minimise such effects a vacuum chamber fitted with a thin beam window is utilised in the EDS, constructed of aluminium, designed to keep the electron exit at a near-normal angle to the beam window. This is visible in the top-left of Figure 5.6. This has been designed and is being physically tested for the EDS, and the applicability of such a window is in the process of being investigated for the IBM.

5.2.2. Reconstruction

Reconstruction of the electron energy spectrum involves transforming the electron position map to the energy map in order to reconstruct energy for a given interval. The fidelity of these energy intervals then has a minimum dictated by the position resolution of the combined resolution of the screens and cameras.

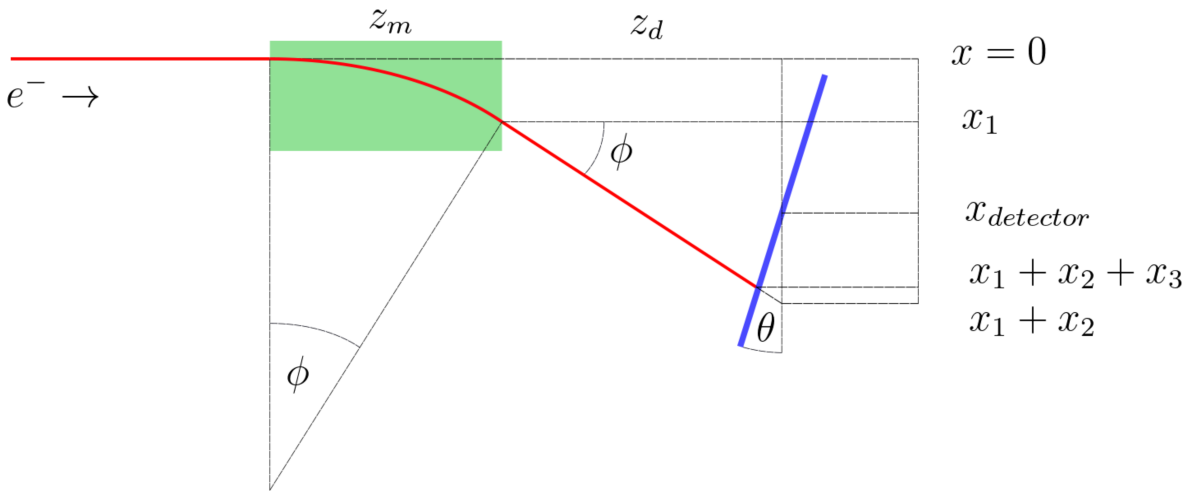

Figure 5.8.: An illustration of the path of an electron through a box-like magnetic field. The green area represents the effective magnetic field, the red line an electron path and the blue line the scintillation screen. x_1 is the x coo-ordinate when the particle leaves the field; $x_1 + x_2$ represents the position of the particle incident on the plane of the centre of the detector plane which is orthogonal to the beam axis; $x_1 + x_2 + x_3$ calculates the position in x of the particle in the detector plane rotated by angle θ.

The conversion of light to particle flux requires the use of a light/charge calibration curve. This will be established for the screen and camera system outside LUXE, using a well-known electron test-beam of adequate energy and a high bunch population in order to measure the light emitted for some known electron flux, and ensuring its linearity.

As previously mentioned, the regions of the screen and image outside the central signal band, and use of beam bunches sent with no laser, allow for the creation of profiles of background to be made and subtracted from the signal measurements. This background can be understood to be a composite of a largely flat distribution of radiation principally coming from the respective beam-dumps, or other complex multiple-scattering events from all around the experimental hall; and in addition a distribution of background particles reaching the screen shortly after being produced from the electron beam. This latter source can then, especially in the EDS, be modelled as symmetric around the deflected electron beam axis. By measuring the background per unit area in the quiet part of the screen, for some radial distance from the modelled e-beam, this symmetry can be exploited to subtract the expected background from the narrow signal band. An illustration of the position of particles of all types from background sources is shown in Figure 5.10.

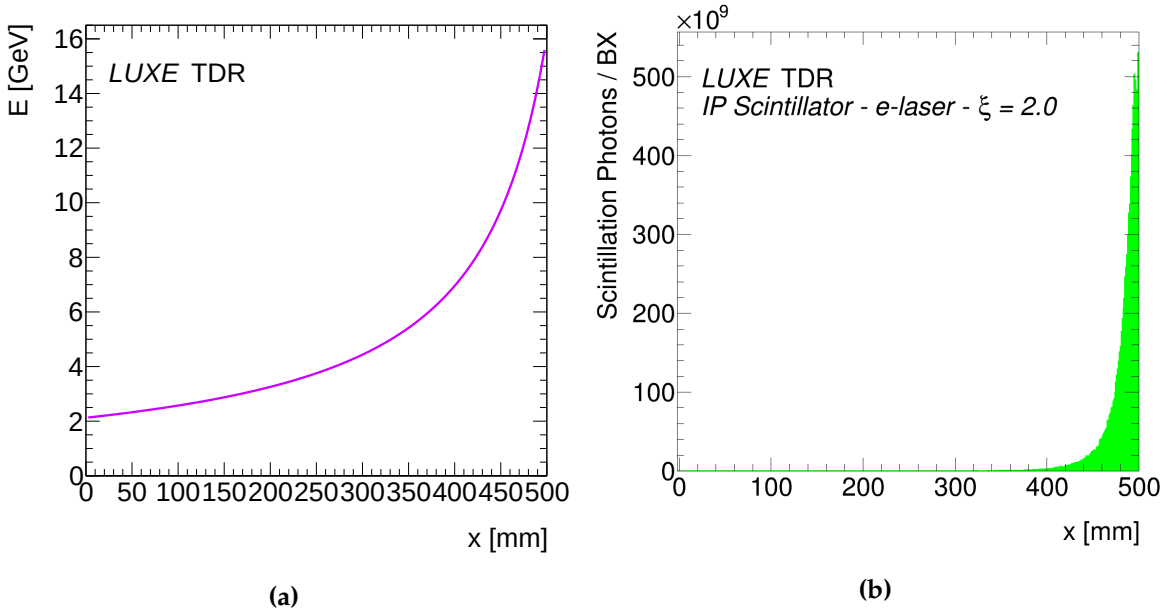

(a) **(b)**

Figure 5.9.: **(a)** The approximate transformation from E to x plotted for the EDS scintillation screen, for a B-field of 1 T. The zero point in the x coordinate here is the low-energy edge of the screen; $x = 500$ mm is the high-energy edge. **(b)** The profile of scintillation light in x position within the scintillation screen, for a $\xi = 2.0$ PTARMIGAN signal simulation, for phase-0 of the experiment. Scintillation light is simulated in GEANT4.

5.3. Technical Description

5.3.1. Scintillation Screen

There is little practical difficulty or high cost associated with extending the range of the screen in the x direction, so the scintillation screen can be engineered to cover the entire possible energy spectrum of electrons exiting the magnetic field (which is expected to be constrained by the size of the aperture of the preceding magnet). However, at present, the design does not attempt to extend as far as possible, as the magnetic action results in the low-energy limit of the spectrum becoming increasingly spread, and given the low electron rates for the EDS below 2.5 GeV as visible in Figure 5.1, the on-screen flux drops to the point of difficulty of detection. The lower energy limit is chosen more pragmatically. In Table 5.1 the dimensions and key parameters of the screens are listed.

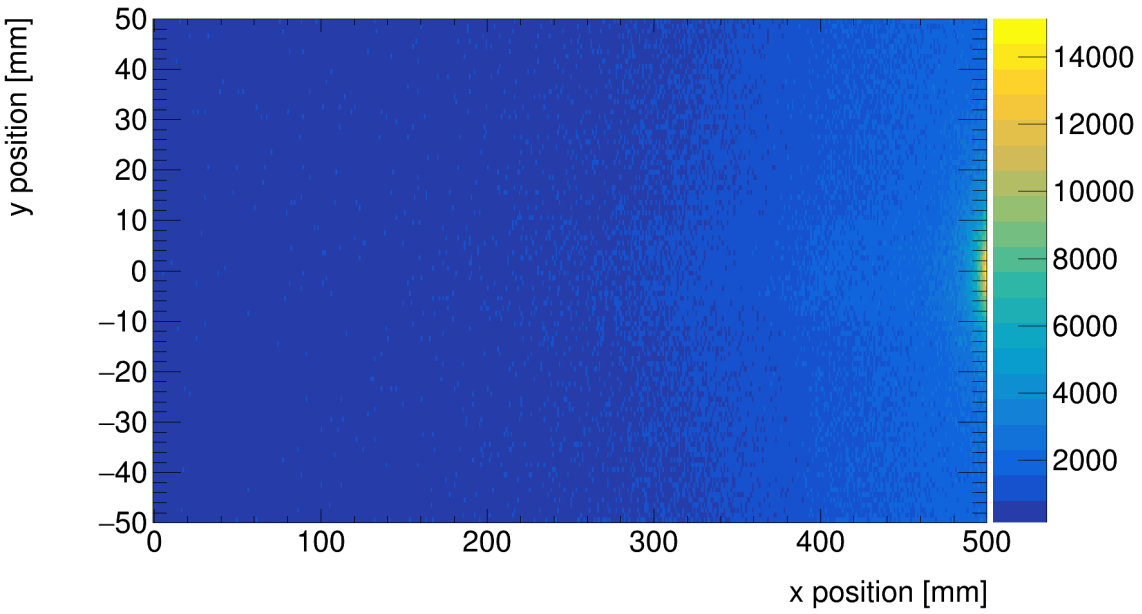

Figure 5.10.: An indicative plot of the background levels for all particles intercepting the scintillation screen in the EDS region. Each bin represents one mm^2 unit of area. The x and y position are with respect to the centre of the screen in y, outermost edge in x, such that high x points toward the beam axis. Simulation performed in GEANT4.

Table 5.1.: Key parameters of the scintillation screen used in the electron detection systems [75]. The screens are foreseen to be identical at each site.

Parameter	Default Value
Length, x [mm]	500
Height, y [mm]	100
Protective layer PET thickness [µm]	6
Phosphor layer GadOx thickness [µm]	310
Support layer Plastic thickness [µm]	188
Total thickness [µm]	507
Thickness in radiation Length, X_0 [%]	2.8
Typical phosphor grain size [µm]	8.5

The scintillation material Terbium-doped Gadolinium Oxysulfide (Gd_2O_2S : Tb, GadOx) is chosen for the screen. Analysis of the material's properties ensures it is suitable for use in this detector:

- **Emitted light wavelength profile:** Best chosen to be within the optical wavelength band of non-specialised optical equipment (mirrors, cameras). The characteristic light emission wavelength of GadOx doped with Terbium is around 545 nm, which easily fulfils this requirement, and filters exist which are optimised for this fluorescent wavelength. While there are secondary emission peaks, this primary emission peak contains the majority of visible light output from GadOx, visible in Figure 5.11 [76].

- **Light emission time profile:** The maximum bunch frequency expected at LUXE is 10 Hz. The relatively long emission evolution of GadOx compared to most common materials – with decay constant $\tau \approx 600\,\mu s$ – is still comfortably within the modest 100 ms required [77]. With this in mind a camera exposure time of approximately 3 ms is used. Ref. [77] gives an afterglow value of 500 parts per million after 20 ms.

- **Scintillation photon yield:** Greater light output gives more statistical significance of measurements in general and above the ambient light background, and GadOx offers some of the highest outputs in terms of the number of photons per unit energy deposited [78]. This is estimated by us as 70,000 photons per MeV deposited. The yield of the scintillator is in principle susceptible to saturation – a quenching of the light yield for high charge fluxes – but the fluxes of particles to measure in LUXE are not expected to be intense enough to observe these effects. At high fluxes it was demonstrated by the AWAKE experiment that GadOx has a linear response up to charges of 350 pC [79], within a $\sim 1\text{mm}^2$ beam-spot area, i.e. also adequate for the un-scattered electron beam, and so no saturation is expected.

- **Thickness:** Given the density and corresponding radiation length of GadOx, and the requirement that the screen perturb the electron energy spectrum as little as possible before measurement by the Cherenkov device, the screen must be adequately thin. The screen's thickness given in radiation lengths, using parameters defined in Table 5.1, is calculated as 2.8%. The manufacturing of the screen involves crushing the GadOx into a fine powder, which is then suspended in a plastic base. This ensures consistency in thickness and optical properties across the surface compared to a continuous crystal.

- **Radiation hardness:** Scintillators which are damaged by radiation can suffer a local decrease in scintillation efficiency. A material's response after deposition of

energy from ionising radiation is always specific to the particle type and energy profile of the radiation, as well as to the flux and frequency of exposures. This makes it difficult to quantify the radiation hardness with absolute confidence. The material's response to electrons of order 10 keV in the context of electron microscopy has been studied [80] and a threshold of noticeable change in the scintillation efficiency (of a very similar screen product) defined. This is calculated in terms of absorbed dose at around 3.3×10^8 Gy. Within simulation in GEANT4, as shown in Chapter 6, fluxes of up to $1 \times 10^8\, e^-\ \mathrm{mm}^{-2}$ are recorded in the e-laser mode at around $\xi = 3.0$, leading to a local maximum Dose per bunch-crossing of ~ 2 Gy constrained to a $0.04\,\mathrm{mm}^2$ area. For the calculated maximum dose, this allows up to $\sim 1.6 \times 10^8$ bunches or operation in LUXE up to 16 years, using the estimate of 10^7 shots made per year. This is a minimum lifetime, as the vast majority of interactions will be at a differing ξ, and so include a lower maximum charge flux.

This can only be an indicative calculation for now. This is especially true as the exact nature of the damage, and its dependence on incident radiation energy / exposure frequency remain unclear. The quality of the scintillation efficiency will be monitored in the experiment, in particular using cross-reference with the Cherenkov detector.

A light-yield calibration and investigation into short-term reductions in the efficiency of the GadOx scintillators is shown in Ref. [81]. Bunches of electrons of 50 pC and 150 pC within a rough $\sim 1\,\mathrm{mm}^2$ area were aimed at a GadOx screen, with frequency 1 Hz, for 1.5 and 0.5 hours respectively. Within this study a prompt reduction of scintillation efficiency with distribution of falling exponential decay is seen, converging down to $\sim 92\%$ for the 150 pC case (which is a factor 10 more intense than the maximum flux in the EDS at LUXE). Whether the efficiency continues to degrade, or whether its function has stabilised on a long-term basis, is not clear from the limited time available to the study.

Given the non-negligible risk of radiation damage adversely affecting the scintillator's response after some time taking data, the design of the frame holding the scintillators will be completed to include the possibility of expeditious exchange of the active material. As seen in Figure 3.2, there are regular short intervals each week in the EU.XFEL running plans which allow access to the experiment. In the case of unacceptable damage the inexpensive screen can then be exchanged. With

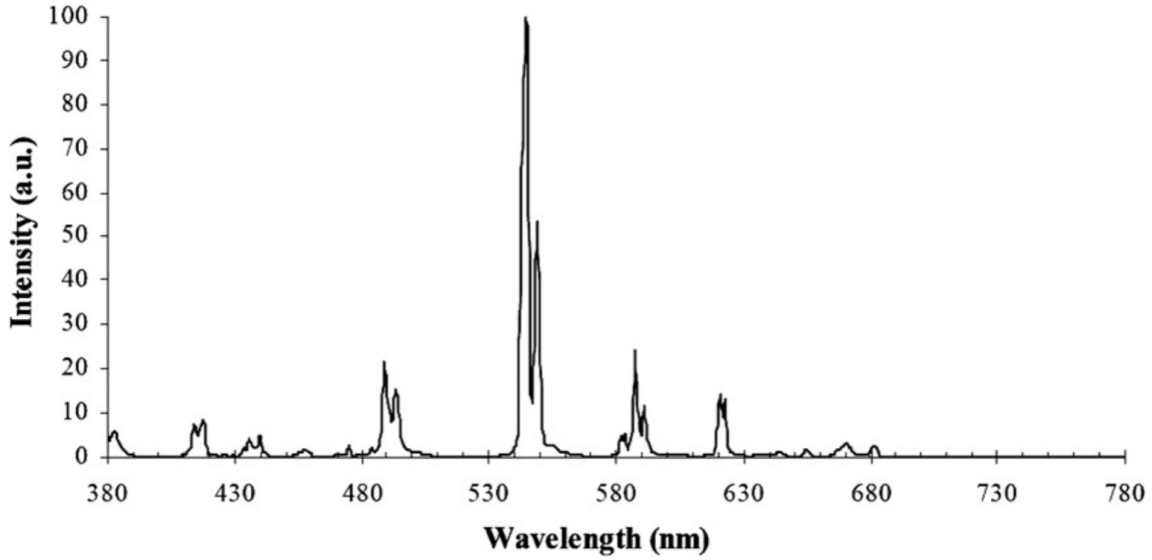

Figure 5.11.: Emission wavelength profile from a scintillator of chemical composition Gd_2O_2S : Tb [76].

a precisely machined groove in the aluminium frame to house the screen, this can be performed while keeping the components aligned within tolerance.

From the Bethe–Bloch formula for energy deposition over distance travelled in matter, the magnitude of signal response in this detector is related to the velocity of the particle, β, like so:

$$\frac{dE}{dx} \approx \frac{ne^6}{4\pi m_e c^2 \beta^2 \epsilon_0^2} \left[\ln\left(\frac{2m_e c^2 \beta^2}{I(1-\beta^2)} \right) - \beta^2 \right], \tag{5.5}$$

for electron number density n and mean excitation potential I, both constants specific to the material. Like in the case of the accompanying Cherenkov detector, which is always twinned with the scintillation screen in LUXE, the response of the screen is dependent on the β of the electrons, rather than energy, and thus the detection efficiency is relatively flat over the GeV energy range. Although the $\ln(1/1-\beta^2)$ term does imply a logarithmic dependence of dE/dx on γ, for a thin volume such as the screen a significant proportion of the radiation escapes and so the dependence remains flat. The reconstructed energy is solely determined by where the particle hits the screen, i.e. by the spatial distribution of the scintillation light observed by the camera. Unlike the Cherenkov device, the scintillator is somewhat sensitive to lower-energy (background) particles as in this regime $dE/dx \propto 1/\beta^2$.

Tables 5.2 and 5.3 give the position and energy acceptances for the EDS and IBM regions respectively. This is given for the EDS spectrometer dipole at B=1T, although this field strength is subject to vary to higher magnitudes, in particular to make high-energy-resolution measurements for values of ξ, where extremely few positrons from the multiphoton Breit–Wheeler process are expected. The γ-laser dipole will remain constant in γ-laser operation, at its maximum field strength.

Table 5.2.: Physical position and energy ranges within the acceptance of the scintillation screen in the EDS. These are calculated with the assumed EU.XFEL beam energy of 16.5 GeV. z denotes the position in the z dimension downstream from the IP. z_d is the approximate distance from the end of the B-field, and x the distance from the high-energy edge of the screen from the beam axis. z_m is the approximate length of the magnetic field in the z direction. The aluminium frame is characterised by the thickness of the wire of the frame, and the displacement of the loop of free air to allow the beam through unperturbed.

Scintillator Parameter	$B = 1\,T$
E_{max} [GeV]	15.04
E_{min} [GeV]	1.832
z [m]	4.85
z_m [m]	1.2
z_d [m]	2.8
x [mm]	66
Frame thickness [mm]	10
Frame loop extension [mm]	15

5.3.2. Cameras

The Basler camera models acA1920-40gm and acA4096-11gm are chosen to measure the scintillation light [82, 83]. Each come from the Basler Area Scan range, employing CMOS sensors to take a monochromatic image. The resolution of these cameras (hereafter referred to as "2K" or "4K" models, given the pixel resolution in the x dimension) are 1920×1200 and 4096×2160 respectively.

In both sites 3 cameras will be used – two of the 2K model, and one of the 4K model. The 2K models will cover each one half of the screen, with the images exceeding the

Table 5.3.: Physical position and energy ranges within the acceptance of the scintillation screen in the IBM. These are calculated with the assumed EU.XFEL beam energy of 16.5 GeV. z denotes the position in the z dimension downstream from the IP. The negative value implies the screen position is *upstream* from the IP. z_d is the approximate distance from the end of the B-field, z_m is the approximate length of the magnetic field in the z direction, and y the distance from the high-energy edge of the screen from the beam axis.

Scintillator Parameter	$B = 1.5\,T$
E_{max} [GeV]	7.5
E_{min} [GeV]	1.3
z [m]	-5.465
z_m [m]	1.2
z_d [m]	0.685
y [mm]	95
Frame thickness [mm]	10

screen by 5 mm in both dimensions and 6 mm overlap between in the middle. This assists with alignment.

The purpose of using an additional 4K camera is to increase the total multiple-camera-measurement dynamic range for the critical high-energy region of the image. In doing so we also introduce finer pixel resolution, although optical spread will limit the utility of this. As a result of the magnetic spectrometry mechanism, the high energy signal is more tightly bunched here in the x direction which motivates the resolution needs. Using the finer resolution, as well as a lens with longer focal length, also gives the 4K camera a lower per-pixel signal as each pixel covers a smaller section of the screen. This means the 4K camera sensor hits its upper dynamic range limit at a higher scintillator light flux, effectively boosting the dynamic range of the combined camera system.

For the two 2K cameras, their view is centred on the centre of the screen in y and at positions one quarter, and at three quarters along the length of the screen (x). The 4K camera at each site is positioned such that the image overlaps the screen in x at the high energy side by 5 mm. Again this image is aimed centrally in y, and 101 mm from the side in x. An illustration of this scheme of coverage is shown in Figure 5.12.

These cameras will be operated with 12-bit digital pixel depth. In order to preserve the 10 Hz functionality for the 4K camera, as for this choice of bit-depth and full

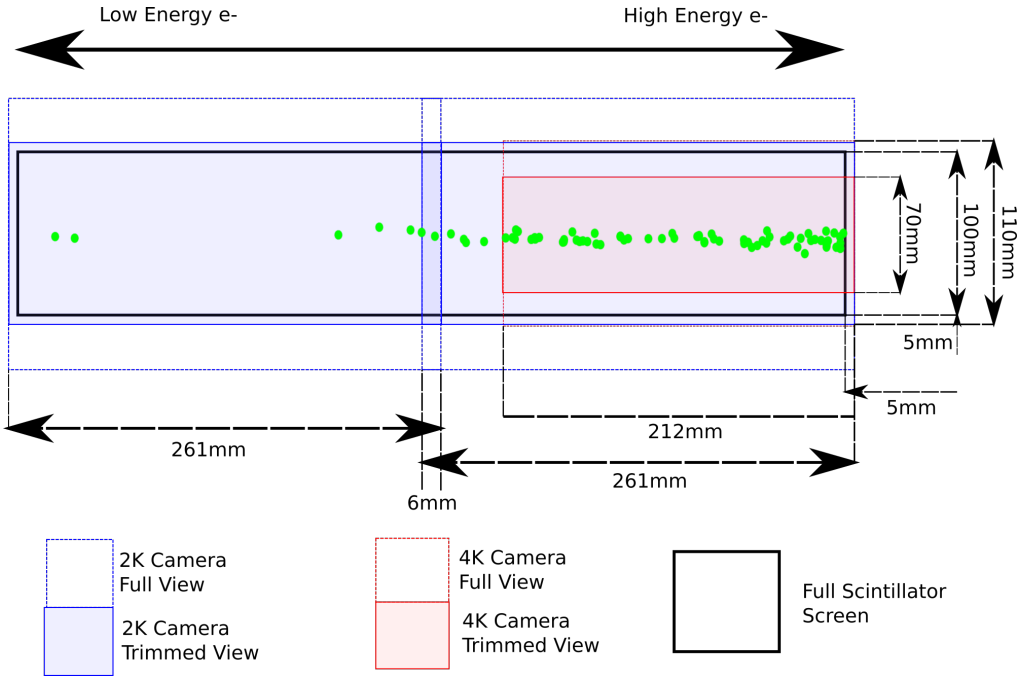

Figure 5.12.: An illustration of the coverage of the scintillation screen from each camera. Valid for both regions of the experiment.

resolution the interface bandwidth is insufficient, the image is cropped at top and bottom. Both models have a global shutter, required for this imaging technique to ensure consistency in timing pixel-to-pixel. Additional technical details for both models are given in Table 5.4.

In recent years, the CMOS pixel technology present in these cameras has become broadly equivalent to the quality of more typical CCD devices for scientific purposes, while still preserving a low cost. The profiles of relative quantum efficiencies for each model of camera are given in Figure 5.13. They both peak at around 545 nm, close to the GadOx characteristic emission wavelength, at a value of $\sim$70%. The linearity in response, in terms of digital pixel grey value per photons/pixel, of each camera model is shown in Figure 5.14. The actual response of specific cameras combined with the scintillation screen system will be measured specifically in high-rate test-beam in the future.

Trigger is handled for these camera models by Hirose 6-pin connections. These connections are only used for the Line 1 connection and common ground in order to trigger exposure start. The other pins are foreseen to remain unused. The trigger signal is a typical TTL (Transistor-Transistor Logic) signal, where an applied potential between 3 V and 5 V triggers the image. Actual activation of the sensor happens

roughly 5 µs after the trigger is applied. Shot-to-shot jitter of this quantity is lower, at ~ 100 ns [84]. This is of little concern as to losing much of the scintillation light as the time constant of the scintillation material is relatively long at ~ 600 µs. In fact, using the beam/laser clock of the wider LUXE experiment means that when the cameras open shutter consistently ~ 5 µs after the interaction, they can avoid the deleterious ambient light effects from Cherenkov radiation within the screen and the air in general, as well as interference from electromagnetic fields in the generation of the laser. The calibration of the screen/camera system will take into account any lost scintillation light emitted before opening sensor-exposure. This is the light-charge calibration curve measurement, which replicates the final experimental setup as much as possible.

Table 5.4.: Key camera model parameters. The nominal position resolution is true for both the vertical and horizontal dimensions.

Camera Parameter	4K camera f=75 mm lens	2K camera f=50 mm lens
Typical quantum efficiency at λ = 543 nm [%]	69	70
Typical sensor SNR [dB]	40	40
Typical power requirement [W]	2.7	2.7
Pixel size [µm^2]	3.45×3.45	5.86×5.86
Total sensor size [mm^2]	14.1×7.5	11.3×7.1
Typical read noise [e^-]	2.3	6.7

Although the cameras and their sensors are intentionally displaced from the beam-plane, they are not guaranteed to be safe from complex scattering events. The vast majority of such events originate from the beam-dump, and so with sufficient lead shielding the sensitive electronics will be protected from almost all typical harmful radiation emerging from the dump. The major exception is neutrons. Neutrons of all energies penetrate dense materials well, and it is therefore not feasible to try to design the region to protect components so. There remains the risk then, that a rare nuclear interaction from a relatively high-energy neutron will damage the electrical components. From Ref. [85], neutron damage of digital cameras is seen within the context of the Joint European Torus nuclear fusion experiment [86]. Near the magnetic confinement chamber, CMOS and CCD cameras are used for diagnostic activity in a chamber with a high neutron flux. A significant increase in 'hot pixels' in an uncooled CCD camera was seen over a running period which corresponds to $\approx 3.4 \times 10^{12}$ n cm^{-2} cumulative flux. The authors explained that the cameras must be replaced after

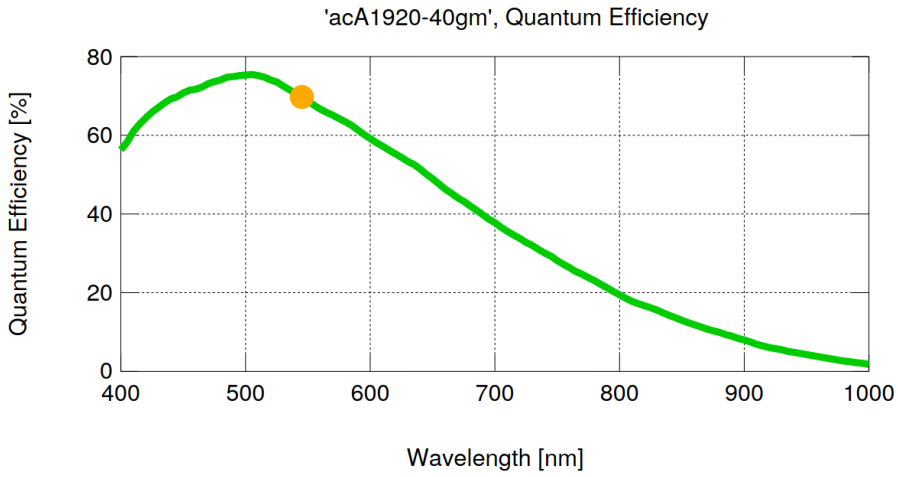

(a)

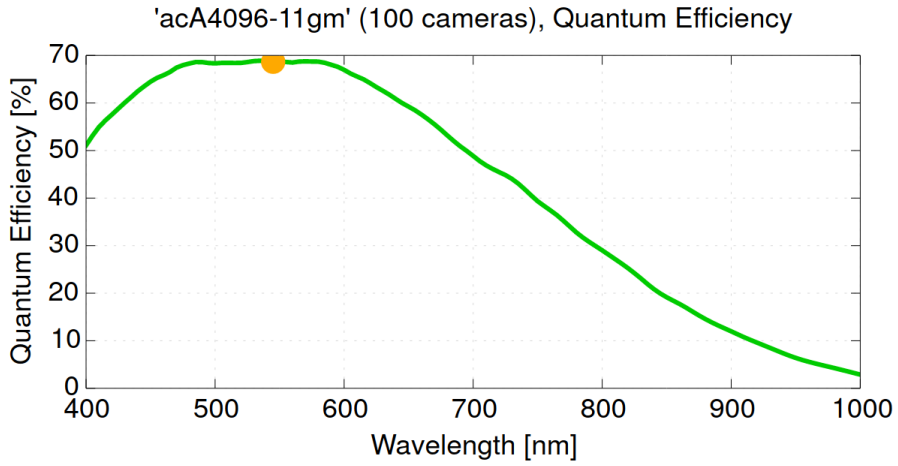

(b)

Figure 5.13.: **(a)** The measured quantum efficiency for the 2K camera for photons of varying wavelength. **(b)** The quantum efficiency profile for the 4K camera. Both exhibit a peak very near the target wavelength of 543 nm. $\lambda = 545$nm is marked in yellow [73,74].

such an accumulated flux, so for our cameras in the LUXE case we may use the same figure as estimate of the maximum tolerable accumulated neutron flux. The paper also calculates the 1 MeV neutron equivalent fluence, by weighting the energy distribution to the damage done to silicon by a 1 MeV neutron, at 1.06×10^{12} n cm^{-2} [87].

A simulation of the neutron flux has been calculated for the LUXE experiment geometry with the FLUKA package [88, 89], which, similar to GEANT4, simulates particle interactions in matter. As first estimate for the IP cameras, this is approximately

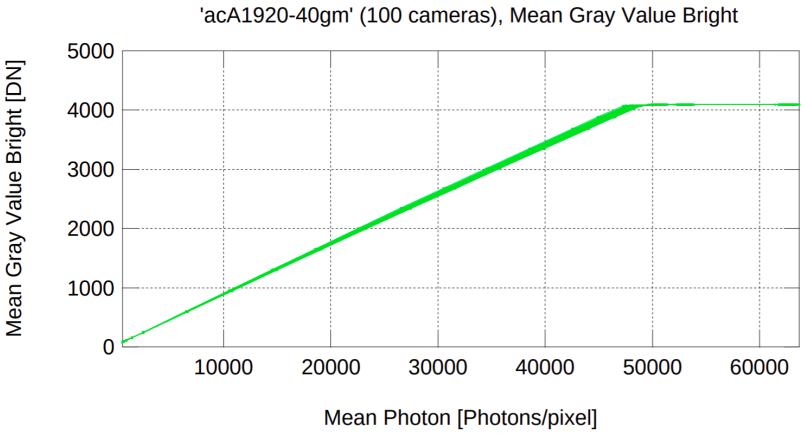

(a)

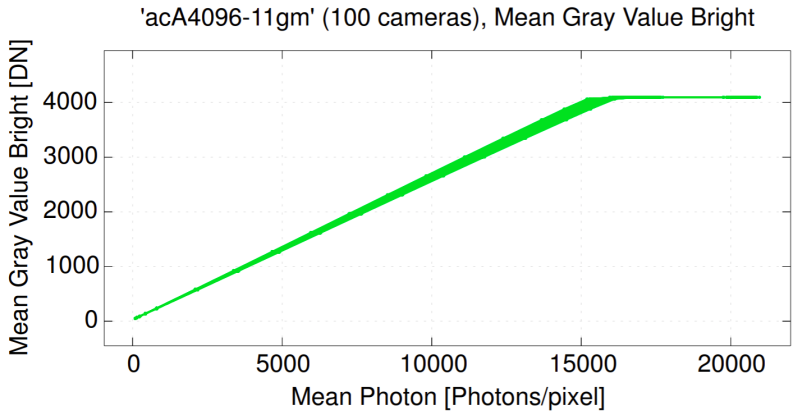

(b)

Figure 5.14.: **(a)** The measured grey value in digital ADC pixel response for the 2K camera for varying intensities of photons/pixel. 100 cameras of the same model are plotted. **(b)** The measured grey value for the 4K camera [73,74].

order 2.56×10^4 n cm^{-2} per electron bunch. The energy profile has been accounted for too, meaning the accumulated neutron flux is equivalent to 4.9×10^3 n cm^{-2} of 1 MeV-equivalent neutrons. Over a year of operation, up to 10^7 seconds of data-taking with beam delivery up to 10 Hz, the 1 MeV-equivalent accumulated flux rises to 4.9×10^{11} n cm^{-2}. This would imply an exchange of camera models every two years. Should the cameras begin to degrade from hot pixels (or radiation damage more generally) quicker than expected, this can be detected quickly and the camera will be exchanged for a back-up.

5.3.3. Lenses

The angle of view of the cameras is dictated by the sensor size and the characteristics of fitted lenses. Given the fixed position of each component, a fixed-focal length lens can be used. Lenses with a focal length of $f = 50\,mm$ suit the parameters well, where one 2K camera is trained upon a width in x on the screen of $\sim 260\,mm$. A lens with $f = 75\,mm$ fitted to the 4K camera allows for a tighter zoom in the interest of finer position resolution. Both these fixed focal lengths are readily available and models for use have been identified, from Edmund Optics [90] and Basler [91].

Each of the lenses have variable focus, from a minimum working distance of $250\,mm$ and $200\,mm$ for the $f = 75\,mm$ lens and $f = 50\,mm$ lens respectively, to a maximum infinite working distance for both. They also have variable aperture sizes, for which closing can in principle minimise the effect of optical disturbances/dust upon the lenses. Keeping the apertures maximally open maximises total light collection, and so this setting will be used. Further technical information is present in Table 5.5. This includes the view angles in the horizontal and vertical, which is the angle subtended by the image subject (the screen) from the sensor. The image circle is the radius of the circular edge of the image transmitted. The rectangular sensor must then remain inside the image circle. A nominal position resolution is calculated using the sensor pixel resolution and the corresponding on-screen image size. The position resolution is valid for both the horizontal and vertical dimensions of the image.

5.3.4. Optical Filters

The optical band-pass filter chosen also comes from Edmund Optics [72]. Its diameter of $50\,mm$ easily encompasses the diameter of both chosen lenses. A filter holder is required to secure them to either lens. The filter is optimised to accept light of central wavelength $543\,nm$, including a full-width-half-maximum of the peak of $22\,nm$. This encloses the main emission peak seen in Figure 5.11; the optical density as function of wavelength of the filter is given in Figure 5.15.

It has become clear that for certain parameters of ξ, the spectrum of electron flux may induce an intensity of light too bright to remain within the dynamic range of the cameras at the EDS site. Two easy solutions to reduce the light levels each have drawbacks: shortening the exposure time or closing the aperture, makes the

Table 5.5.: Key lens model characteristics.

Lens parameter	4K camera f=75 mm lens	2K camera f=50 mm lens
Working distance [mm]	1200	1200
Horizontal view angle [°]	10.8	12.9
Vertical view angle [°]	5.7	8.2
Horizontal image width at screen [mm]	212	261
Vertical image height at screen [mm]	112	164
Trimmed vertical image height [mm]	70	110
Nominal positional resolution [µm]	51.8	135.9
Typical optical distortion [%]	<0.1	0.06
Mass [g]	436	277.5
Image circle radius [mm]	21.6	17.6

measurement more susceptible to temporal jitter, or is difficult to precisely control, respectively. The solution chosen for these runs is to outfit the 4K camera with an additional neutral density filter. This effectively increases the total dynamic range and will be implemented when needed (when approaching the problematic running ξ_{max}) with a quick addition of the filter during short accesses to the hall. The filter can be included mechanically by attaching the filter to the end of the band-pass filter (or its holder). A suitable filter is identified in Ref. [92]. Its optical density of 0.6 implies a fraction of light transmitted compared to light incident of ~ 0.25.

5.4. Further Technical Details

Further work has been performed to ensure the suitability of this system for the requirements described. These are of limited physics interest, instead dealing with the technical details, including the computing and network requirements, as well as construction and installation projections. For completeness, material describing these considerations is given in the appendices.

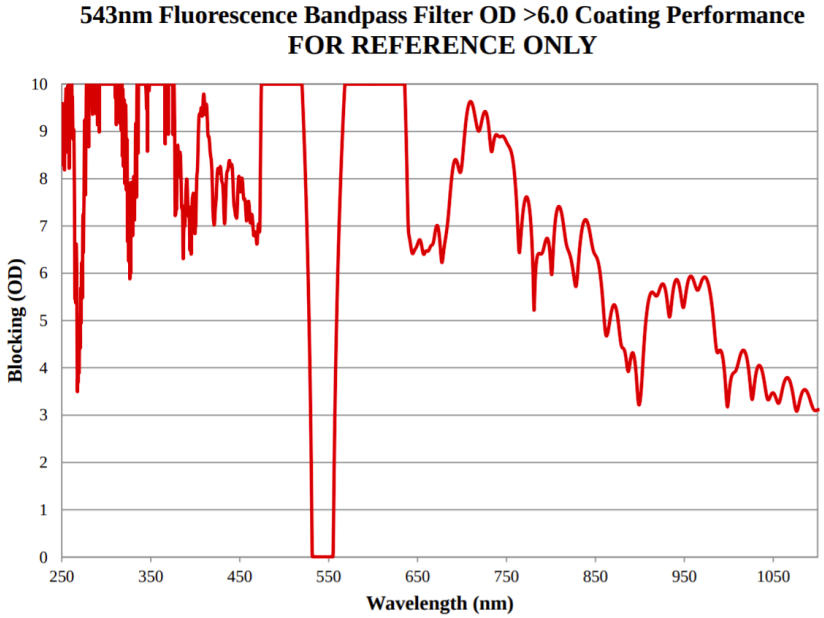

Figure 5.15.: Optical Density (OD) for the chosen band-pass optical filter. Outside the desired waveband, the OD is always greater than 3, meaning transmission is less than 0.1% [72].

5.5. Considerations for the Future

The system described here is a near-complete account of the required design of a scintillation screen & camera system for the measurement and reconstruction of a flux of high-energy electrons. In order to have complete certainty in the use of this system in these regions of the experiment, three major points remain outstanding:

- The optimisation here is made with the EDS in mind, as this is the mode of LUXE which will be installed and run first. The secondary site of this detector, the IBM, placed immediately downstream of the photon beam generation site and its dipole magnet, requires more work to optimise the response.
- The expected total resistance to disruption via radiation damage is not clear. Anecdotally, one can find a wide variety in the stability of similar systems in similar radiation environments. As shown in Section 5.3, despite the very modest 1-10 Hz bunch frequency, the peak localised on-screen electron flux can reach up to $10^8 e^-$ mm^{-2}, depositing up to $\sim$2 Gy in a small local area every shot. Testing the running scintillator screen & camera system in a similar environment directly should give more confidence with the consistency of the system, especially with

regards to neutron damage of the cameras. The dumping of the electron beam in the R-Weg facility at DESY provides a similar environment to that at LUXE, providing an option for such a test [93]. In such an experiment the benefits of self-annealing due to a cooled camera sensor, e.g. from a simple Peltier device, could be investigated. With regard to neutrons, a re-design of the EDS region to place the cameras on the other side of the screen in the z direction would reduce the neutron flux, should it appear to become a problem, with the assistance of the inverse-square law.

- A measurement will be made, once the detector is fully assembled, of the digital response of each camera with respect to varying on-screen flux. This should be performed at a facility with an electron beam with well-known variable bunch-charge. Each camera ideally would be measured independently, which is possible concurrently using the same light emitted from one screen. This is proven possible at facility such as CLEAR at CERN [94, 95], but may also be performed to a satisfactory accuracy at DESY [96].

Chapter 6.

Scintillation Screen & Camera Detector System in Simulation

6.1. Simulation

The LUXE experiment infrastructure, including in particular beam delivery and particle detectors, has been implemented in GEANT4. This is used in conjunction with the SFQED Monte Carlo simulation PTARMIGAN to simulate both the magnitude of harmful radiation throughout the experimental chamber, and also the expected signal and detector responses when running. Included in the simulation is the implementation of the EDS and IBM detectors and their supports. For analysis of the operation of these particular detectors, a breakaway simulation was developed which included the optical scintillation and Cherenkov physics processes of each of these particular detectors; unnecessary objects were removed to improve computation speed.

The relatively complete physics list of QGSP_BERT_HP [51] was used. This list utilises the typical quark-gluon string model (QGSP) to simulate high-energy hadron interactions. The Bertini cascade process is used to refine the effects of hadrons $< 10\,\text{GeV}$, excepting the high-precision neutron package (HP) which handles the transport of low-energy neutrons. Most important for the function of the detector are the electromagnetic interactions, which are simulated with the standard EM list. As input to the simulation of the EDS response, the resultant SFQED state from the PTARMIGAN simulation is used. Each resultant particle from these PTARMIGAN simulations was placed in the interaction chamber in the GEANT4 simulation, with the correct kinematics. The PTARMIGAN simulations do not typically output a total

number of particles consistent with the 1.5×10^9 bunch population, instead assigning each particle a weighting, such that one particle may represent many others. The weighting is equal to the full bunch-population expected in LUXE divided by the simulation-bunch-population (and so for a simulation bunch population of 10^6, the weighting is typically 1.5×10^3). The GEANT4 simulation then transports the electron flux, via the magnetic field, through the electron detectors. After the passing flux deposits energy, then scintillation light is produced (quantised into 'optical photons' in GEANT4) and recorded along the surface of the screen. A weighting is applied to this output in order to normalise consistently on a per-bunch-crossing basis, and also to account for an intentional reduction to the scintillator's yield (which reduces the computational load per event). Choosing the scintillation yield wisely, the profile of scintillation light on the screen is created, weighted correctly to normalise to one bunch-crossing, but with the total statistics equal to the total number of expected photons reaching the camera sensor(s).

With the simulation of one or many bunch-crossings complete, the reconstruction of the energy profile of the electrons from these light profiles can be performed. This can then be compared to the truth-level input electron spectrum which is also recorded at run-time in the simulation; after that, deeper analyses can be made of the reconstructed spectra. The reconstructed Compton edge energy can be compared to the true value (from PTARMIGAN) to evaluate the accuracy of the detector.

6.2. Reconstruction

6.2.1. Charged Particle Transport Through a Magnetic Field

To ascertain the energy of a charged particle due to its deflection in a magnetic field, a relation between this input energy and the particle's position must be derived. This subsection details the calculation of the intercept point for a charged particle in some 2-dimensional detector plane after a box-like constant magnetic field. This models particles as aligned with the z axis and incident at x=0, as in Figure 5.8.

Within this model, electrons undergo a simple circular motion for as long as they are within the field, and travel in a straight line as soon as they exit. Their path is therefore analysable entirely geometrically. The radius of the circular motion is

obtained by equating relativistic expressions for acceleration due to the Lorentz force and centripetal acceleration. Relativistically, the Lorentz force is described as:

$$\frac{dp^{\alpha}}{d\tau} = qF^{\alpha\beta}U_{\beta} \tag{6.1}$$

$$F^{\alpha\beta} = \begin{bmatrix} 0 & -E_x/c & -E_y/c & -E_z/c \\ E_x/c & 0 & -B_z & B_y \\ E_y/c & B_z & 0 & -B_x \\ E_z/c & -B_y & B_x & 0 \end{bmatrix} \tag{6.2}$$

$$U_{\beta} = (U_0, U_1, U_2, U_3) = \gamma(c, -\underline{v}) \tag{6.3}$$

which results in a proper acceleration $\alpha = F/m_e = \gamma qvB/m_e$, understood to be in the x direction (Figure 5.8). Converting to lab frame acceleration, understanding that all acceleration is orthogonal to the direction of travel and so $a = \alpha/\gamma^2$, it is found that:

$$\frac{\gamma^2 v^2}{R} = \frac{\gamma qvB}{m_e} \tag{6.4}$$

using the definition of centripetal acceleration. This simplifies to an expression for the circular motion radius:

$$R[m] = \frac{E[eV]}{B[T]\, c[ms^{-1}]} \tag{6.5}$$

where we use $v \approx c$ and $E = \gamma m_e c^2$ considering our highly relativistic particles, and substitute E/q for E in eV units. With the circular path known, the x position of the particle as it leaves the magnetic field at z_m is:

$$x_1 = R(1 - \cos(\phi)) \tag{6.6}$$

and ϕ, the angle the electrons travel thereafter, is equal to $\phi = \sin^{-1}(z_m/R)$. The additional distance in x it travels until it intersects a detector plane orthogonal to the z direction at z_d is:

$$x_2 = \tan(\phi) z_d \tag{6.7}$$

Finally we add a provision to account for the possible rotation of the detector in the y axis by an angle of θ.

$$x_3 = \frac{\tan(\theta)\tan(\phi)(x_{detector} - x_1 - x_2)}{1 + \tan(\theta)\tan(\phi)} \tag{6.8}$$

where $x_{detector}$ denotes the x-position of the centre of the detector screen. Summing these provides us with the x-position of a hit of an electron of a given energy.

$$\begin{aligned} x_{global} = x_1 + x_2 + x_3 = R(1 - \cos(\phi)) + \tan(\phi) z_d \\ + \frac{\tan(\theta)\tan(\phi)(x_{detector} - x_1 - x_2)}{1 + \tan(\theta)\tan(\phi)} \end{aligned} \tag{6.9}$$

From here transforming to the detector's local x coordinates is elementary:

$$x_{local} = (x_{global} - x_{detector})/\cos(\theta) \tag{6.10}$$

In the small angle approximation, one can simply replace the cosine, tan and sin functions with $1 - \frac{\phi^2}{2}$, ϕ and ϕ respectively. Then evaluating a simplified, approximate expression of only $x_1 + x_2$ (equivalent to assuming a detector plane orthogonal to the beamline):

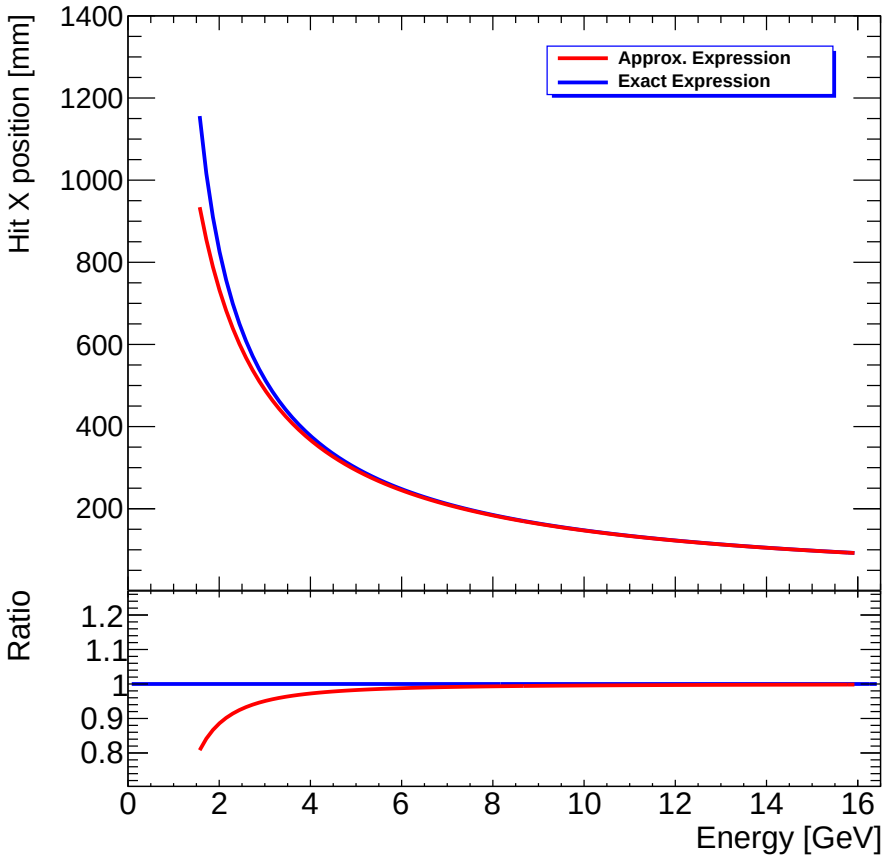

Figure 6.1.: The discrepancy between an approximative expression and the full expression for magnet bending of electrons in the case of the electron detection system. The functions are shown plotted between 1.5 GeV and 16 GeV, similar to the acceptance of the planned scintillator screen detector. The expressions are asymptotic for low energy.

$$x_1 + x_2 = \frac{Bcz_m}{E_{eV}} \left(\frac{z_m}{2} + z_d \right) \tag{6.11}$$

This results in a $x \propto 1/E$ and $E \propto 1/x$ relationship. For many purposes Equation 6.11 is satisfactory for calculations, but for the final reconstruction of the experiment the full expression 6.9 will be used. The discrepancy between the approximate expression and the full evaluation is shown in Figure 6.1 for the box-like magnetic field and a range of LUXE EDS electron energies.

The full expression compares well to results from a GEANT4 simulation, which iteratively solves its particle transport, ensuring agreement between two models. While it

is not assumed in the GEANT4 simulation that the incoming electrons are perfectly aligned with the z direction – the beam is modelled accurately as per EU.XFEL beam data – the constant, box-like magnetic field is replicated in GEANT4. In the near future, a measured field map of the magnet(s) at DESY will provide the realistic field function which can be implemented within the GEANT4 simulation. An implementation of a reconstruction process which can instead model the transformation from $E_{\text{electron}} \rightarrow x$ using the measured field-map is then required. This has been created and is described here.

Charged Particle Transport in a Mapped Magnetic Field

The formulae above are used in an iterative process, where the magnetic field map is modelled as a number of these small static fields, and the propagation of the particles calculated for one segment (or hereafter, *voxel*) of the field map at a time. The formulae give the particle's exit position and momentum vector as it enters the next, until the particle exits the field map entirely or it is proven to be theoretically trapped within the $x - z$ plane of the field map. Upon exiting the field map, having calculated the exit position and momentum vector, the particle is propagated forward to once more calculate the corresponding hit position upon the scintillator screen.

Only the dominant y component of these fields are used. An x or z component (within the coordinates of LUXE, where z denotes the beamline direction) will deflect only very slightly into the y dimension, irrelevant to the reconstruction of energy using the x coordinate. To be usable within the voxel-based approach of many small box-like field volumes, the formulae above are modified to account for a variance in angle of approach as well as non-zero point of inception (x_0, z_0). Thus the formulae:

$$\begin{aligned} x &= \sqrt{R^2 - (z_p + R\ \sin(\phi))^2} + x_0 - R\cos(\phi) \\ z &= \sqrt{R^2 - (-x_p - x_0 + R\ \cos(\phi))^2} - R\sin(\phi) \end{aligned} \tag{6.12}$$

are used for normal incidence, where the progression to the next voxel is in the z direction (and so $z = 0$ at the point of inception). A visual aide for the tracking, and in particular the meaning of the symbols in equations 6.12 & 6.13 are shown in Figure 6.2. For lateral incidence, the inverse is true ($z_0 \neq 0$ & $x_0 = 0$):

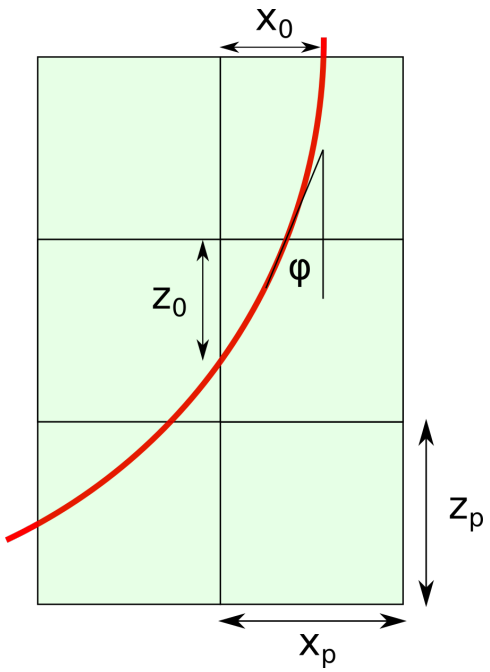

Figure 6.2.: A schematic of the voxel solution of tracking a charged particle through a field-map. R, the radius of turning of the particle in the field, is re-calculated for each voxel. The top-right, middle-right and bottom-left voxel shows a normal incidence, where the particle enters the voxel from the z direction. The middle-left pixel shows lateral incidence.

$$\begin{aligned} x &= \sqrt{R^2 - (z_p - z_0 + R\ \sin(\phi))^2} - R\cos(\phi) \\ z &= \sqrt{R^2 - (-x_p + R\ \cos(\phi))^2} + z_0 - R\sin(\phi) \end{aligned} \tag{6.13}$$

where x_p, z_p are the physical size (in the x and z direction) of the voxels. The change in ϕ ($\Delta\phi$) from step to step is calculated using the inception, exit points and the known radius of the magnetic curvature, with the trigonometric identity $\Delta\phi = 2\sin^{-1}(c/(2R))$. Propagating the charged particles through this plane of pixel-like volumes is simulated until the field map ends. Thereafter the position and trajectory of the charged particle is known, and as before is traced further to a hit point on the screen, modelled as a plane.

The transformation from x position to energy can be calculated for two types of binning. Either the binning intervals of the energy profile are kept regular, or the intervals of on-screen position x are. For the former, the known regular limits of each energy bin are used to calculate the corresponding limits in x with the formulae

previously detailed. The integrated light emission between each of these calculated x limits is required. The histogram of the measured light profile is then fit linearly in each small interval, and the integral of the function between the limits is calculated to return the flux within.

For the latter case, when the known limits of x correspond to the edges of the pixels (or some integer multiple), the light value intervals can be taken directly from summing neighbouring pixels of the simulated 'image'. These must then be represented in irregular intervals in energy. In order to calculate E for some x, instead of the inverse, the full algorithm is run iteratively with E increasing minutely, until the desired x is found. The approximative Equation 6.11, rearranged for E, is used as the starting point for this as it gives a consistent small offset from the true value for E. This iterative process can then require considerable time to calculate, particularly for a fine voxel field map, but once calculated the values can be stored. They are not expected to change regularly during the running of LUXE. They depend purely on the alignment of the elements and in particular the magnetic field.

6.2.2. Digital Signal to On-Screen Charge Conversion

With the energy / x correlation calculated, the other half of the reconstruction is the conversion of the recorded image light profile to the on-screen charge flux. This will be gathered for the specific full system in the future in a test-beam experiment, the purpose of which is to establish a calibration curve of the CMOS digital signal per unit on-screen charge. For the purposes of this reconstruction, the expected conversion is gathered from a small, separate GEANT4 simulation which fires a known number of GeV-energy electrons at an instance of the screen of Gadolinium Oxysulfide. The resulting number of photons per on-screen electron is calculated and used. This simple process does not satisfactorily simulate an entire test-beam setup, including error propagation, and so the final expected error of the conversion between the on-screen charge and resultant light flux (and finally digital signal) can only be gathered from reference to past efforts [95] and should be kept in mind (at approximately 2%).

The generation of light in the scintillation process is suppressed by a variable in the GEANT4 simulation we call the scintillation yield. As noted this can be chosen to only generate as many scintillation photons as are expected to reach the sensor (and be detected), thereby emulating the statistics available to the detector in one

bunch-crossing. The expected on-lens light per incident electron is calculated using the photons-per-electron, the expected solid angle covered by the lens, and the quantum efficiency of the sensor. Other factors, such as the transmission of the lens, the transmission of the light through the band-pass optical filter, and the reduction in emitted light when viewing the screen at an oblique angle, are estimated and incorporated. As mentioned in the previous chapter the mean energy deposition in the thin screen from electrons across the GeV range is effectively constant – the energy deposition is not exactly flat across the screen, however, as the angle of incidence that the particle hits the screen elongates its path length and therefore increases the mean energy deposited. The angle of attack from the electrons, relative to the screen normal, is calculated alongside its x position and then weighted to normal incidence with a $\cos(\phi)$ factor.

Regardless of the underlying statistics, the light-profile histograms are overall weighted such that they are normalised to one bunch crossing. The calibration from the separate test-beam GEANT4 simulation gives the photon-per-electron calibration (for 1 GeV electrons incident on the screen of 0.31 mm GadOx), and this is used to finally recover the electron energy spectrum.

As briefly mentioned in Chapter 5 the performance of the scintillation efficiency thereafter will be monitored, most of all with cross-reference to the Cherenkov detector covering the same spectrum. If the results from the detectors start to drift with respect to one another, this can be detected (although further tests required to isolate the sources in either detector). Replacements will be kept in storage for both screens and cameras, each with their detector efficiency measured. Between regular data-taking periods, when the electron energy is comparatively low (see Fig. 3.2), the un-scattered beam can be deflected directly onto the screen (and through Cherenkov detector) by altering the strength of the magnetic field. Here the total charge on-screen is the well-known full charge within the bunch, and so the detector response checked. Its exact position also functions as a check of the magnetic map (Appendix B).

6.2.3. Noise

Background from the multiple scattering of radiation (typically from the un-scattered electron beam), interacting and inducing light with the screen, is inherently modelled in the GEANT4 simulation. The contribution is expected to be small, as shown later in Figure 6.5, inside the central signal band. Electron-beam-only events were generated

to create the background profile, which was subtracted from the generated signal light profile. The bands above and below the central signal band are also averaged and subtracted from the central signal band.

Electronic noise from the camera sensor is implemented in the reconstruction using real, dark images recorded from the camera sensor and optical setup we anticipate for LUXE. This is better detailed in Chapter 7. In brief, for the purposes of the reconstruction, a single-shot noise-map is created from one of the dark images, which includes ambient light from a darkened but not light-tight experimental area. The specific noise-map-image is chosen randomly for each new bunch-crossing reconstruction. This is added pixel-by-pixel to the reconstructed light-map from the GEANT4 simulation; the digital noise and the simulated light profile are normalised to one another from test-beam results (Chapter 7). A subtraction of the average noise is also emulated, using an averaged noise-map which is the aggregate of 100 dark images. Doing so then gives us the realistic effect of noise for a single shot / image, but also emulating a subtraction of a dark noise map. Each individual image has its own deviations from the mean noise map, and these deviations appear in the final reconstructed spectra.

6.3. Performance

The expected performance for the two sites of the scintillator and camera systems differ. Although the requirements and environments for the two sites are similar, the objectives are not quite the same: for the EDS, the energy spectrum of electrons within the detector acceptance is desired. For the IBM, the energy spectrum of the corresponding photon beam is required. As previously noted this involves correlating the electron energy roughly to the photons by subtracting the electron energy distribution from the beam energy. Multiple-emission events obscure this by softening the electron spectrum and breaking the exact relation. To account for this, simulation of the Bremsstrahlung (and pair creation) effects in the tungsten target will be performed, and the results used to deconvolve and achieve the photon signal (using GEANT4). This comes with the caveat of additional errors associated for the corrections, which are expected to be not insignificant for a target of 35 µm. In addition, the region of the photon spectrum most important to characterise – the high energy limit – corresponds to the lowest energy electrons, which are not detectable as they do not escape the downstream dipole exit. For these reasons emphasis is placed on the 'monitoring'

function of the scintillator & camera system in this region, although the quality of the straightforward electron energy reconstruction is anticipated to be similar in both regions.

The uncertainty of measurements of rates (or fluxes) of electrons within the energy acceptances for each detector (see Tables 5.2 and 5.3) are expected to be at the few-percent level, dictated by the light–charge calibration to be performed in test-beam. Comparison can be made to Ref. [97], for a similar light–charge calibration which provided approximately $\pm 2\%$ uncertainty.

Of great interest for the EDS, and visible in Figure 5.1, is the measurement of the energy of Compton edges. The goal for the detector system is below 2% uncertainty on energy. This is approximately the uncertainty of the edge position due to a $\pm 2.5\%$ uncertainty of the underlying ξ, at the IP, as measured by the laser diagnostics [1]. The energy resolution as percentage with the magnetic spectrometer can be approximated as:

$$\frac{\sigma_E}{E} = \frac{\Delta x}{eBz_m(\frac{z_m}{2} + z_d)} \times E \tag{6.14}$$

from Equation 6.11; here e is the dimensionless charge $\sqrt{4\pi\alpha}$, as natural units are employed, with the terms z_m, z_d shown in Figure 5.8. Or, condensing the expression:

$$\frac{\sigma_E}{E} = \sigma_0 \times E/\text{GeV} \tag{6.15}$$

The expected position resolution derived for 2 camera models from the camera & screen system (shown earlier in Table 5.5) and what they mean for the relative energy resolution are shown in Figure 6.3. Both camera models – detailed in the technical description of Section 5.3 – nominally remain more than an order of magnitude below the 2% level throughout the energy acceptance. The position resolution is also limited by the point spread of the signal through the vacuum-chamber-exit-window and intervening air, before the energy deposition spread and optical point spread of the screen. The spread due to the environmental scattering and stochastic energy deposition within the screen has been simulated in GEANT4 for several simulation-perfect mono-energetic signal sources from 2.5 to 15 GeV. The full-width-half-maximum

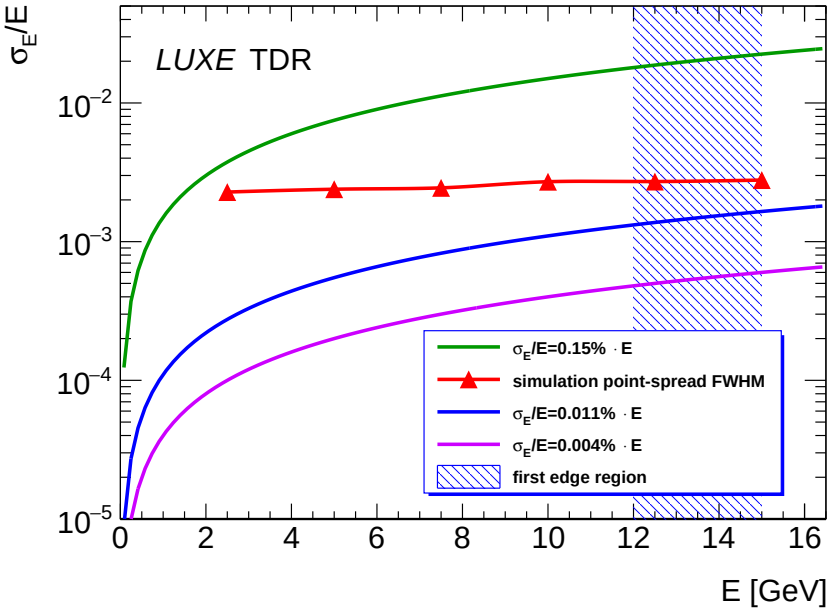

Figure 6.3.: Energy resolution, as function of energy, of the nominal resolutions of the Cherenkov detector and camera resolutions. The functions of 0.004% E and 0.011% E represent the inherent position resolution of the camera setup(s); the 4K and 2K camera respectively. The function of 0.15% E represents the minimum energy resolution to achieve accuracy of 2% within the expected first edge region of Compton spectra. The dispersion of signal sources due to the geometry of the system are plotted using the full-width at half maximum of the point spread of the scintillation response of the screen from mono-energetic sources in GEANT4 simulation. The associated trend-line of these points is only empirical and not the fit of any function.

value of the resulting scintillation responses have been used to represent the resulting energy uncertainty due to environmental scattering and plotted too in Figure 6.3. There one can see that the nominal position resolution expected from the cameras is finer than that expected of the point-spread action of the scintillation screen; exceeding the resolution requirements is useful, as it can aid in deconvolution of the smeared signal in post-analysis, and gives margin for the optical line to be redesigned without troubling the energy resolution limit or requiring a change in camera. Uncertainty in the final measured B-field map will also highly affect this energy determination. The uncertainty of any field-map is expected to be at 1% or lower, and so is actually likely to be the dominant uncertainty when reconstructing energy, and within the required 2%. The final uncertainty for this measurement over many bunch-crossings is not expected to be significantly affected by statistics.

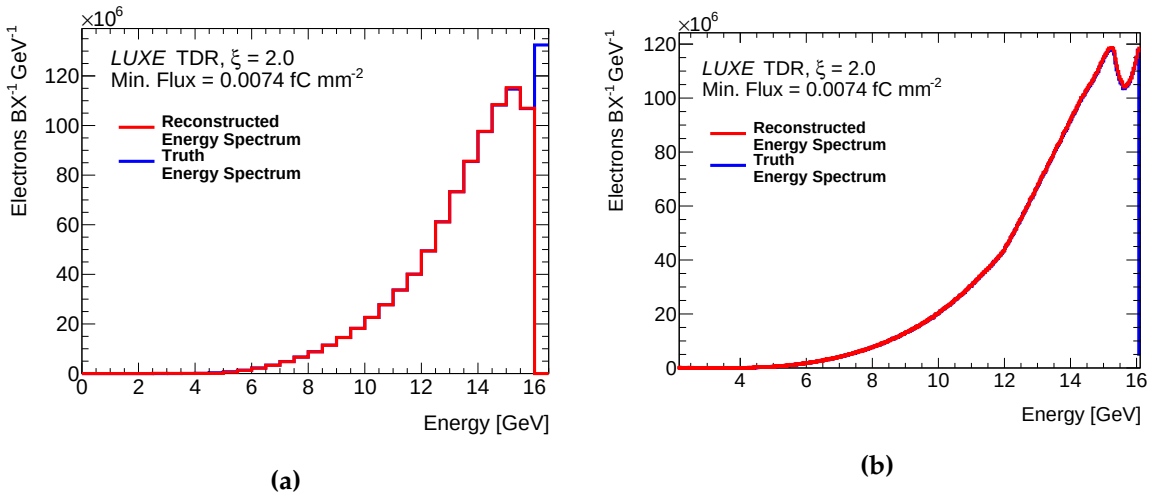

Figure 6.4.: Reconstructions of electron energy spectra from a $\xi_{max} = 2.0$ SFQED interaction, using the simulated screen & camera and reconstruction algorithm. This includes the relevant backgrounds and noise characteristics of the detection. **(a)** is a reconstruction with regular energy binning. **(b)** shows a reconstruction of the same data for the finer, non-regular energy binning corresponding to a position resolution of 0.2 mm. The reconstructions represent the statistics of the sum of 100 bunch-crossings, or accumulated data for 100 seconds. Note the upper limit of the reconstruction is at or very near 16 GeV in both plots.

Reconstructions for the entire simulation, reconstruction and noise emulation process are shown in Figure 6.4. Each represents the sum of 100 bunch-crossing simulations (each with noise emulation), where the PTARMIGAN simulation maximum intensity (ξ_{max}) is set to 2.0, for the LUXE baseline laser parameters in phase-0. Both plots exhibit a small difference between the total reconstructed and truth integral, within the acceptance of the detector, of $\sim 0.5\,\%$. The sum of background (beam-induced stray radiation), which is accounted for in these simulations and reconstructions, fluctuates between $\sim 1\%$ and $\sim 0.1\%$ of signal levels for all regions of the screen. This is seen in Figure 6.5.

6.3.1. Analysis Using Finite-Impulse-Response Filters

The previously described process of simulation and then energy reconstruction of the scintillation screen & camera system uses the output of SFQED PTARMIGAN simulations as input electron spectrum. The ideal, nominal ξ parameter of each simulation is known, as is the distribution of ξ values at the point of each instance of non-linear Compton scattering.

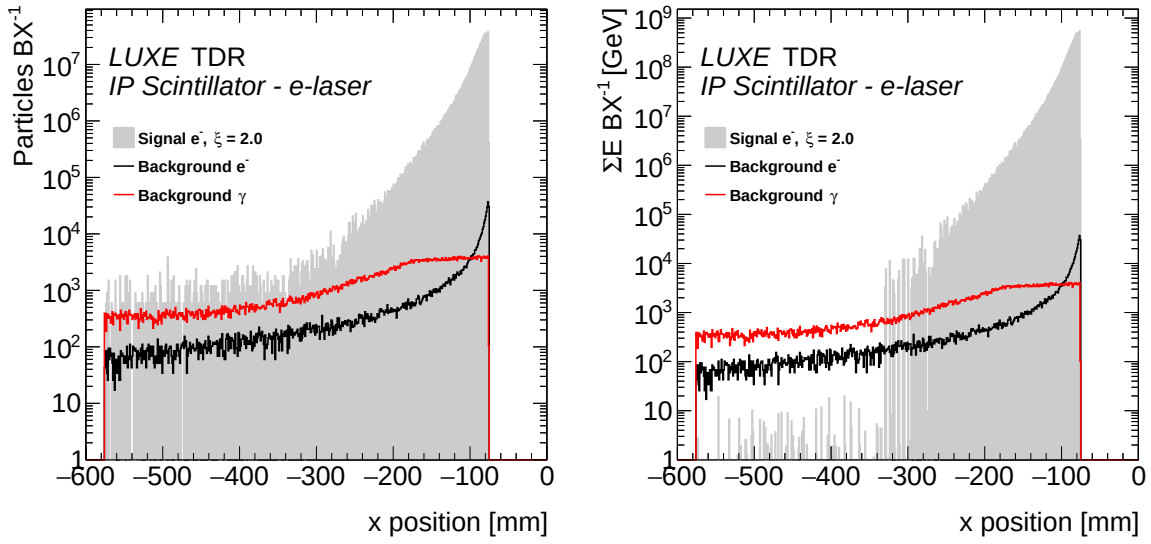

Figure 6.5.: The signal vs background rates for the EDS for phase-0 of the experiment with $\xi_{max} = 2.0$. Particles per bunch-crossing within mm bins is given in **(a)**, and the integral of energy of the particles is shown in **(b)**. The statistics of the signal dataset was considerably less than that of a full bunch-crossing, evidenced by the seeming discontinuity within **(b)**.

As mentioned in LUXE literature [1] and Chapter 2, the position of the Compton edge feature depends on the ξ value at the point of non-linear Compton emission. Briefly, this point in the electron energy spectrum can be expressed with:

$$E_{Compt.} = E_{Beam} - E_{Beam}\left(\frac{2\eta}{2\eta + 1 + \xi^2}\right) \tag{6.16}$$

with:

$$\eta = (\hbar\omega_L E/m_e^2 c^4)(1 + \beta\cos(\theta)) \tag{6.17}$$

where, in addition to $\hbar$ and c with their usual meanings, E and β denotes the energy and speed of the electron, m_e is the mass of the electron, and ω_L denotes the frequency of the laser background. θ is the angle between the laser and the electron beam, where zero is a head-on collision, equal to 17.2° in LUXE.

The edge shifts – in the electron spectrum – closer to the beam energy with increasing ξ. Measurement of the Compton edge then becomes more challenging for the EDS

detectors, as due to the mechanics of the magnetic spectrometry the absolute energy resolution degrades (roughly linearly increasing as per Figure 6.3). As can be seen in Figure 5.1 the clarity of the edge in the truth spectrum degrades too. There are two facets to the smearing of the edge:

- There is no constant ξ in the laser spot, but rather a distribution. In order to reach a higher nominal ξ_{max}, the laser must be focussed tighter, meaning a greater proportion of the finite-sized electron beam passes through a region of the 3-dimensional ξ distribution significantly lower than ξ_{max}. The effective ξ experienced by the electron beam is smeared, and so the Compton edge also smeared.
- As the distribution of ξ increases, so too does the general rate of scattering. In turn the proportion of the electron spectrum which has radiated multiple times increases, spreading the edge feature.

Figure 6.6 shows the results of reconstructions of one-shot simulations (including only the statistics one expects from one bunch-crossing), with the realistic scattering, statistics and noise characteristics of the system included. They use various values of nominal ξ, dictated by the focussing of the phase-0 JETI40 laser. The pixel resolution here is set at 200 µm, similar to the nominal resolution of the 2K camera defined in Table 5.4.

The highest nominal ξ_{max} achieved in the IP is reconstructed using the position in energy of these Compton edges. This can be simply analysed as the local maximum of the energy distribution. This is then compared to the expected Compton edge, calculable from the ξ_{max} known from the PTARMIGAN simulation using Equation 6.16. In Figure 6.7 one can see the result of this simple analysis, for a range in ξ_{max} values between 0.15 and 4.0. Above this value of $\xi = 4.0$, the Compton edge is shifted beyond the acceptance of the scintillator screen. Each point represents the measurement of one bunch-crossing (6.7a) or 10 bunch-crossing (6.7b) reconstructions. The measurements are repeated (100 and 10 times respectively) to gather a mean and standard deviation for each point in ξ. The 100×1BX therefore denotes analysis of a single simulated shot; 10×10BX means the analysis of 10 shots aggregated together. These measurements are compared to the theoretical ideal, plotted alongside upper and lower bounds for $\pm 5\%$ uncertainty in ξ. The error bars of the reconstructed points are the sum in quadrature of a 1% systematic energy uncertainty estimate and the standard deviation of the distribution of reconstructed edge positions. As one might expect, the results

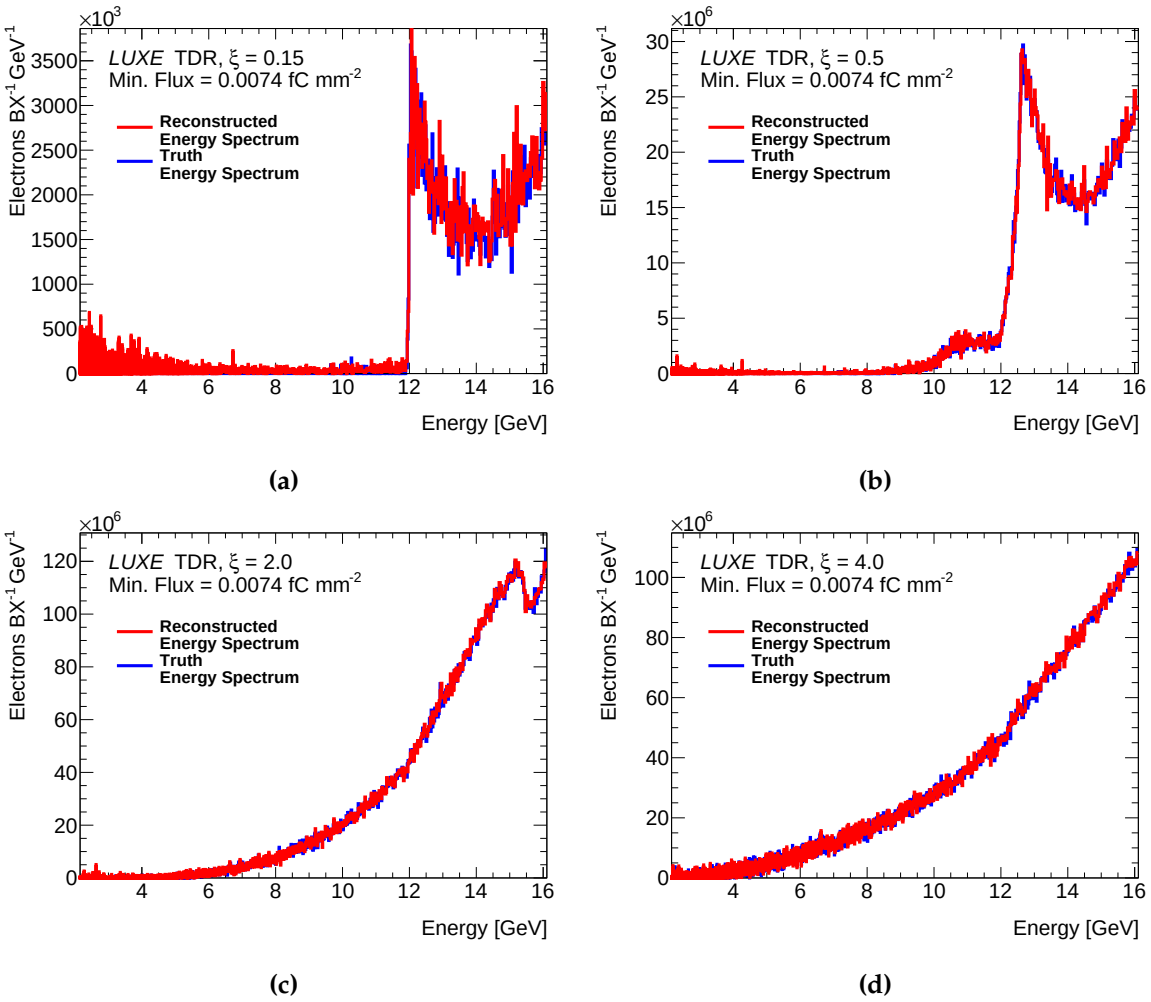

Figure 6.6.: **(a)** A reconstruction of a single-shot example SFQED electron spectrum, from PTARMIGAN, with $\xi_{max} = 0.15$ using the GEANT4 simulation of the screen and camera system. This uses a threshold-of-sensitivity value of $0.0074\,\mathrm{fC\,mm^{-2}}$ in the reconstruction (see Chapter 7). The effective resolution used for this simulation is 200 µm. **(b)** Shows a similar analysis for a PTARMIGAN simulation with larger value of $\xi_{max} = 0.5$. **(c)** and **(d)** show reconstructions for the $\xi_{max} = 2.0$, 4.0 PTARMIGAN simulations respectively.

for only one bunch-crossing are poorer than the sum of ten, represented in the larger errors.

The best single-shot resolution of this edge is desirable to be able to discriminate between bunch-crossings and therefore shot-to-shot variations of the ξ, distribution (due to possible timing or spatial inconsistency). Fluctuations due to statistics and noise inhibit these reconstructions. One technique to recover subtle edges in kinematic distributions, particularly above noise, is the finite-impulse-response of a matched filter

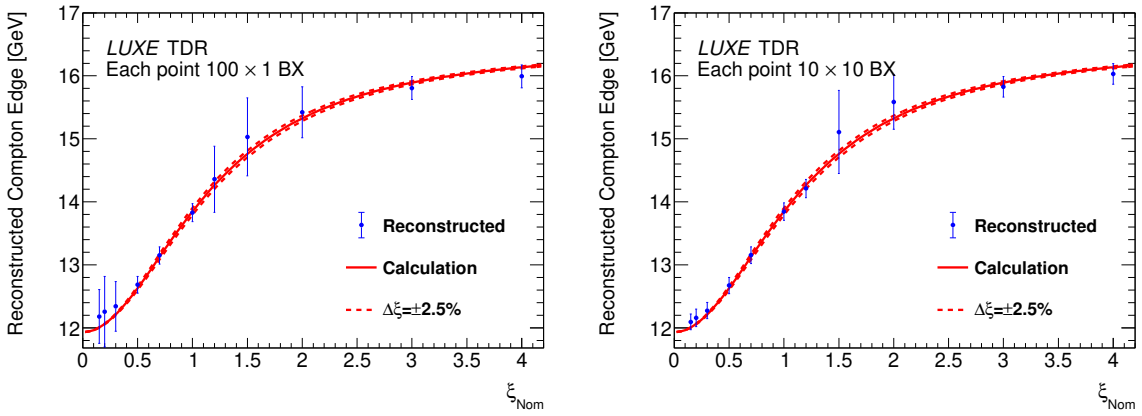

(a) **(b)**

Figure 6.7.: **(a)** The reconstructed Compton edges for simulations of one bunch crossing for each point in ξ. The measurement is made 100 times for each point to find a mean and standard deviation. The reconstruction is performed with the energy of the center of the maximum bin in the reconstructed energy spectra. **(b)** Shows a similar analysis, instead for the spectra of 10 accumulated bunch-crossings. Each point shows the mean of ten of these 10 BX spectra.

function. This has been already studied in the context of the Cherenkov detector [70], but eminently also has use in this context with the scintillation screen & camera detector system.

The application of various finite-impulse-response (FIR) filters is exemplary in Ref. [69]. Elucidated in this publication is the use of convolutions between a discrete observed distribution, and a discrete matched filter, in order to recover any non-continuous or sharp rises or falls in the distribution, known as a kinematic 'edge'. The location of edges can be obtained by finding the local extrema of the derivative of the filter convolved with the desired kinematic distribution. Consequently, for a finite edge feature, the maximum of the edge in the kinematic spectrum may be recovered from the zero-crossing immediately after the local maximum in the finite-impulse-filter response. The response $R(x)$ can be expressed in the continuous form with:

$$R(x) = \frac{d}{dx}(f(x) * g(x)) = (f'(x) * g(x)) \tag{6.18}$$

for some function to be analysed $g(x)$ and chosen filter $f(x)$. This uses $(f * g)' = f' * g = f * g'$, a result from the properties of the convolution. As is typical in physics, the real data expected are in a discrete form. The equivalent discrete form is:

$$R(i) = \sum_{k=-N}^{N} \left[\frac{h_d(k+1) - h_d(k-1)}{2\Delta k} \right] \cdot g_d(i-k) \tag{6.19}$$

for integer i, k. h_d is the discrete form of $f'(x)$ and g_d the discrete data. Within the aforementioned Ref. [69], it is seen that the matched filter distribution – above denoted with $f'(x)$ – of the First Derivative Of a Gaussian (also written as FDOG) provides the best results. For the analyses contained in this work, this FDOG construction of a matched filter is used. This function has a discrete form:

$$h_d(k) = -k \exp\left(-\frac{k^2}{2\sigma^2} \right) \tag{6.20}$$

If the edge has a finite, non-zero width W, then a characteristic scale factor σ (the standard deviation of the original Gaussian form) similar to W gives the best results in terms of filter efficiency.

The finite-impulse-responses for each of the spectra in Figure 6.6 are shown in Figure 6.8. The clarity of the primary peak is shown as degrading with increasing ξ_{max}, as explained. To find the maximum point of the finite edge, and therefore the ξ_{max}, the point that these distributions cross the x axis after the maximum in the spectra is used as the Compton edge position.

The results of the reconstruction of the nominal ξ, using the FIR technique, again for a range of nominal ξ, are shown in Figure 6.9. Shown left are the results of samples of single-bunch-crossing energy spectra. Right shows the analysis for the application of the filters to reconstructions which are the sum of ten bunch-crossings. Again the measurement of both are repeated to find a mean and standard deviation. Compared to the simple reconstructions of nominal ξ, in Figure 6.7 the 10 bunch-crossing spectra results are similar, with a slight systematic underestimate coming from the finite-impulse-response analysis at higher ξ, (notable at $\xi, = 3.0, 4.0$). For this reason, in both plots in Figure 6.9, the points at $\xi, = 3.0, 4.0$ simply use the maximum of the distribution and do not use the finite-impulse-response. The application of finite-impulse-response filters has markedly improved the stability and mean accuracy of the lower-ξ, (and so higher relative noise) reconstructions. These analyses are for particular values of the

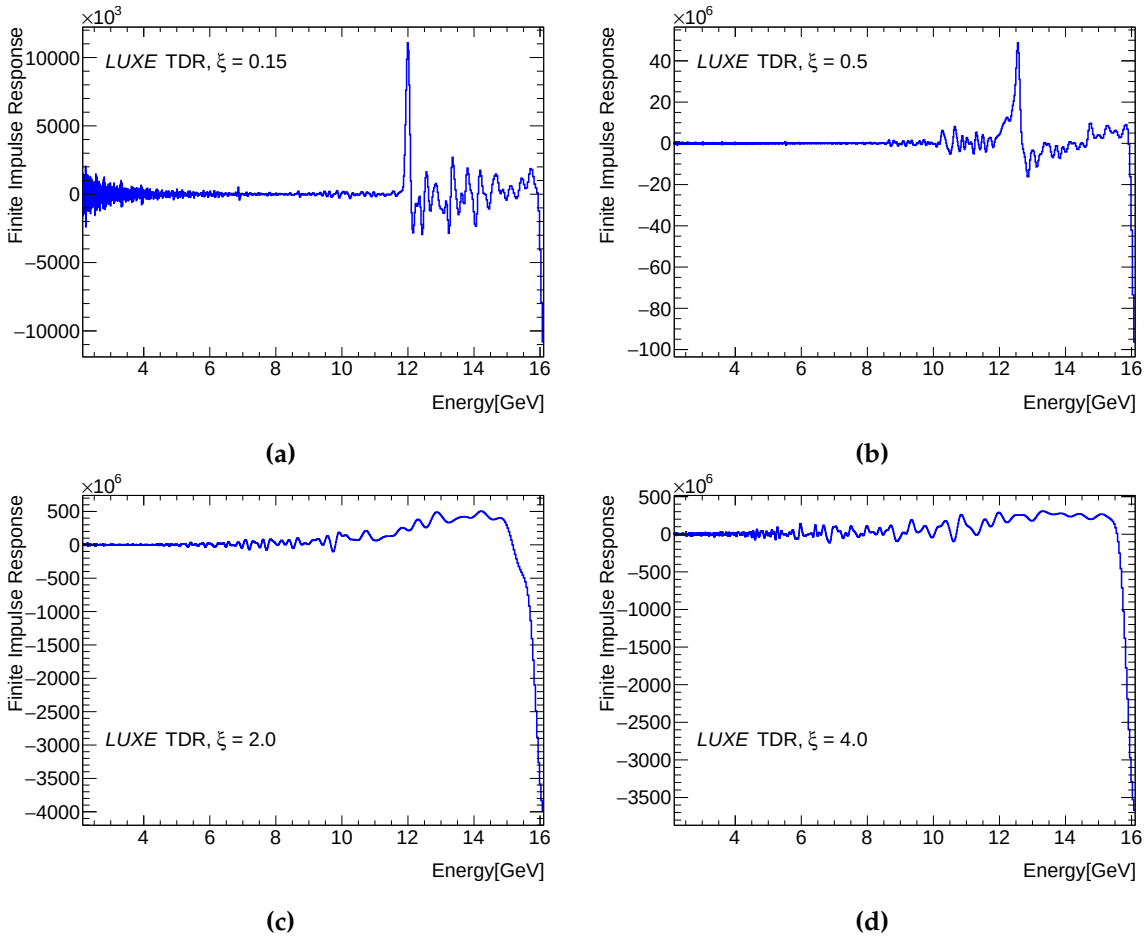

Figure 6.8.: **(a)** The finite-impulse-response for spectrum **(a)** in Figure 6.6. The y axis in each of these plots is arbitrary. **(b)**, **(c)** and **(d)** similarly show responses for the same filter of spectra **(b)**, **(c)** and **(d)** of Figure 6.6 respectively.

characteristic width of the matched filter σ, which have been iteratively optimised for each point in ξ. The error bars are again the sum in quadrature of a 1% systematic energy uncertainty and the standard deviation of the reconstructed edge positions.

The quality of the single-shot reconstructions as fraction of the calculated theory trend (implemented in the original PTARMIGAN simulation) are shown in Figure 6.10. For each of the points, the reconstructed edge is within (or very nearly within) one percent of the theoretical expectation from the simulations. Accounting for the given uncertainties, any single measurement of just one bunch-crossing is very likely to be made to an accuracy of order 1 %, satisfying the 2 % energy uncertainty goal for the case of reconstructing Compton edges; but here, proven in the case of single bunch-crossings. The statistical error of each point is small, and the error bars visible in Figure 6.10 are dominated by the $\pm 1\%$ systematic error estimate.

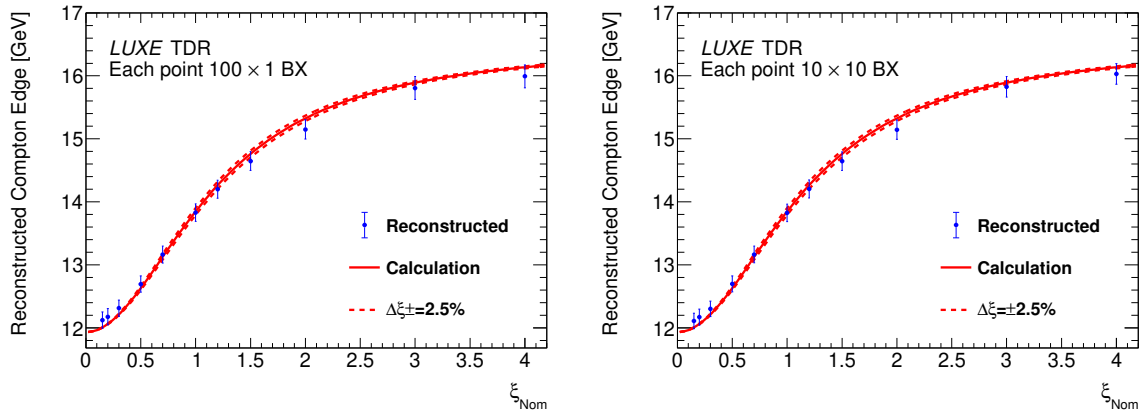

(a) **(b)**

Figure 6.9.: **(a)** The reconstructed ξ_{max} values for single-bunch-crossing reconstructed spectra for each point in ξ. The measurement is made 100 times for each point to find a mean and standard deviation of the measurement. The reconstruction here is performed with the finite-impulse-response technique. This is compared to the theoretical ideal alongside upper and lower bounds for $\pm 2.5\%$ uncertainty on ξ. **(b)** Shows a similar analysis, instead for the spectra of 10 accumulated bunch-crossings. Each point shows the mean of ten of these 10 BX spectra.

The expected position of the Compton edge at the value of $\xi = 4.0$ is at the limit of the scintillator detector acceptance, seen to be within 400 µm from the edge of the screen. The results for the $\xi = 4.0$ points are therefore not meaningfully different from using the high-energy limit of the reconstruction in the case of a smooth, edge-less, rising energy distribution. In practice, we can expect to lose the ability to identify the Compton edge for some ξ_{max} between 3.0 and 4.0 simply due to its shifting too close to the limit of the detector acceptance.

6.3.2. Reconstruction of ξ Distributions

Returning to higher statistics, a slightly deeper analysis of the edges within the spectra can be made. Within each edge feature one can retrieve information, through the use of the FIR filters or not, of both the maximum and point of maximum gradient – the point of steepest ascent – of the edge. The maximum turning point has been used thus far as equivalent to the ξ_{max} of the initial simulation. The point of maximum gradient can be hypothesised to correspond to that region of the ξ distribution where the most Compton interactions have occurred. This is equivalent to the peak of a histogram of such a distribution, also hereafter referred to as the mode of the ξ profile or ξ_{mode}.

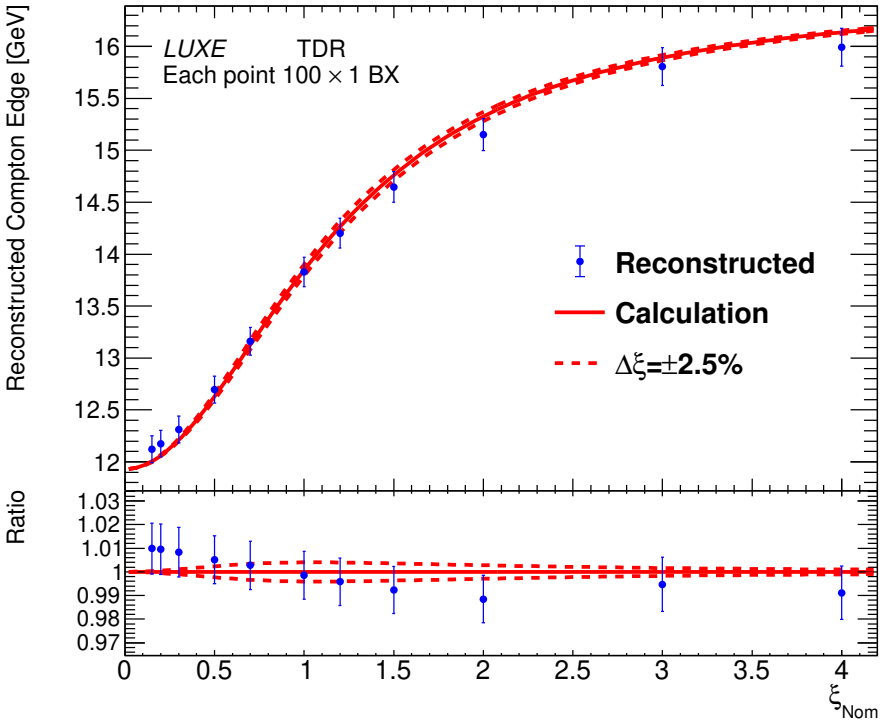

Figure 6.10.: Optimised reconstructions of Compton edges with comparison to theoretical expectation for each ξ_{max}. The Compton edge measurement is made for the reconstruction of one bunch-crossing. This is performed 100 times for each point to find the mean and a statistical standard deviation of each measurement.

This is too subtle to perform with the statistics of one bunch-crossing, but is possible even with the sum of the reconstructions from one hundred bunch-crossings. With improved statistics the analysis no longer requires – or indeed benefits from – the FIR analysis technique. Finding the point of maximum gradient is performed simply by choosing the largest positive increase from one bin to another. The limit between these two bins is used as the point of steepest gradient.

The reconstructed ξ, from these two values, ξ_{max} and ξ_{mode}, can be recovered using a rearrangement of Equation 6.16:

$$\xi = \sqrt{\frac{2\eta}{1 - E_{Compt}/E_{Beam}} - 1 - 2\eta} \tag{6.21}$$

The distribution of real ξ at the very point in space and time of the non-linear Compton interactions, i.e. the ξ at the vertex of creation of the resultant photon, is recorded and can be displayed from the output of PTARMIGAN. This distribution is displayed in four plots for four simulations of differing ξ_{max} in Figure 6.11, alongside reconstructions of ξ_{max}, ξ_{mode}. The recovered values for Figure 6.11a are a poor match. With reference to the Compton edge shifting with ξ, visible in Figure 6.10, at low ξ the shallow gradient means that even a small discrepancy in the edge measurement leads to a large relative error in the reconstructed ξ values. A similar effect is true for larger ξ, visible in Figure 6.11d, where in particular the edge becomes more and more 'washed-out', making finding the ξ_{mode} difficult. Between the smaller and larger ξ regions, there exists a goldilocks zone where the reconstruction is broadly possible (Figure 6.11b, 6.11c). Numerical values of both these reconstructed values are shown later in this chapter in Table D.1. Of note in particular is the high variance of the ξ_{mode} values for higher simulation ξ_{max}, uncorrelated almost entirely from the actual position of the edge, implying the edge is smeared enough that no significant steep edge can be found.

6.3.3. The Fitting of Complete Functions to Spectra

An advanced analysis of data from LUXE will involve the fitting of full functions describing the energy distributions of the electrons. This can be done using the analytic function generating the photon energy spectrum expected for non-linear Compton scattering. For given electron and laser photon energies and ξ parameter, this can be given in the form of the differential interaction probability per unit volume per unit time [20] :

$$\frac{dW}{dx} = \frac{1}{(1+x)^2} \sum_{n=1}^{\infty} \left[-\frac{4}{\xi^2} J_n^2(z_x) + \left(2 + \frac{x^2}{1+x}\right) \left(J_{n+1}^2(z_x) + J_{n-1}^2(z_x) - 2J_n^2(z_x)\right) \right] \tag{6.22}$$

where x is a Lorentz-invariant dimensionless energy parameter. Hereafter using natural units, in the case of a strong-field it is defined as:

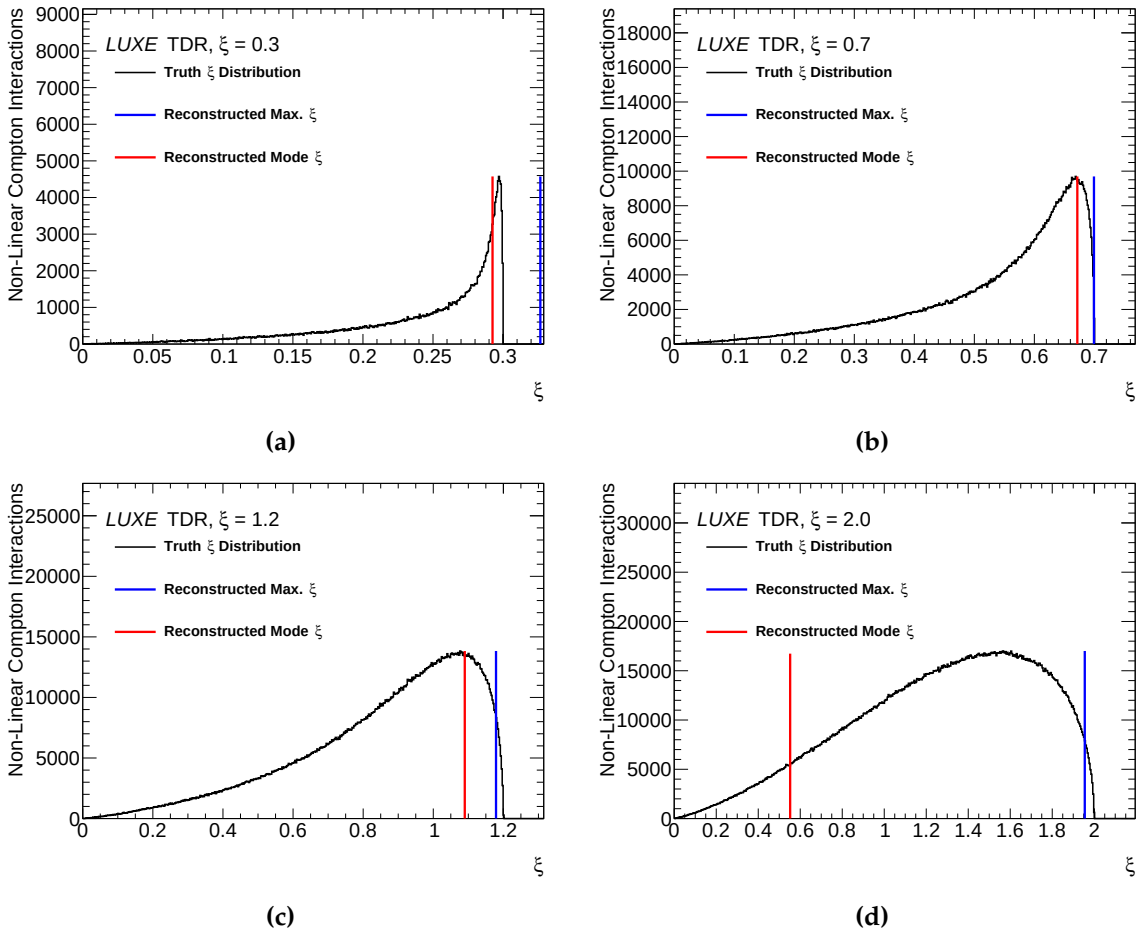

Figure 6.11.: **(a)** The distribution of ξ values at the vertex of the non-linear Compton interactions as simulated by PTARMIGAN, accompanied by the reconstructed values of ξ_{max}, ξ_{mode}. The nominal ξ_{max} value of this simulation is equal to 0.3. **(b)**, **(c)**, **(d)** show the equivalent for $\xi_{max} = 0.7,\ 1.2,\ 2.0$ respectively.

$$x \equiv \frac{k \cdot k'}{k \cdot p'} = \frac{t_n}{u_n - m_*^2} \tag{6.23}$$

using modified Mandelstam variables s_n, t_n, u_n and the effective mass m_*:

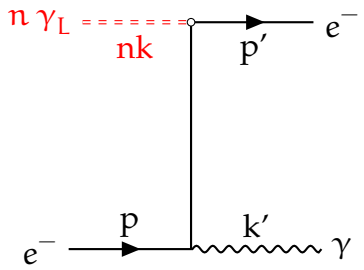

Figure 6.12.: Non-linear Compton scattering, including labels for momenta of participating particles.

$$m_* = m_e\sqrt{1+\xi^2} \tag{6.24}$$
$$s_n = m_*^2 + 2nk\cdot p \tag{6.25}$$
$$t_n = -2nk\cdot k' \tag{6.26}$$
$$u_n = m_*^2 - 2nk\cdot p' \tag{6.27}$$

k, k' and p, p' are momentum vectors of the initial and final photon(s) and electron, respectively; this is understood to be in the case of circular laser photon polarisation, baseline for LUXE. A reminder of the Feynman diagram, including labels for these momenta, is shown in Figure 6.12. The expression 6.22 is a sum over the integer n, which refers to the order of the harmonic - or the number of laser photons absorbed - before the real photon emission. J_n are Bessel functions of the first kind, ξ has its usual meaning, and the term z_x is defined below.

$$z_x \equiv \frac{m_e^2\xi\sqrt{1+\xi^2}}{k\cdot p}[x(x_n - x)]^{1/2}, \quad x_n \equiv \frac{2n(k\cdot p)}{m_e^2(1+\xi^2)} \tag{6.28}$$

where x_n represents the maximum kinematically allowed x transfer for a given harmonic n. It enforces the Compton edge effect. The $m_e^2(1+\xi^2)$ term corresponds to the effective mass and so the 'mass-shift' of the Compton edge for changing ξ.

With the expectation of both electron and photon being highly collinear, monochromatic beams, and the crossing angle between them well-known, this quantity can be calculated with prior knowledge. In particular, the $k\cdot p$ term can also be written using the dimensionless η parameter:

$$k \cdot p = \eta m_e^2, \quad \eta = |p||k|(1 + \cos(\theta))/m_e^2 \tag{6.29}$$

In LUXE the crossing angle, θ, is 0.3 rad (17.2°). In order to shift from the Lorentz-invariant x quantity to the measurable photon / electron energies in the lab frame, the following relation can be used:

$$x = \frac{n\nu - \nu'}{\kappa_n - n\nu + \nu'} \tag{6.30}$$

where ν, ν' are dimensionless frequency parameters for the incident and resultant photons. They are defined as $\nu \equiv \omega/m_e$, which reduces to E_γ/m_e when using natural units. The κ_n constant is:

$$\kappa_n = n\nu - \beta\gamma(1 - \beta^2)/2 \tag{6.31}$$

using the relativistic β, γ values for the incident electron from the reference frame of the lab. So, in order to correctly transform from x to ν', one requires:

$$\begin{aligned} \frac{dW}{d\nu'} &= \frac{dW_n}{dx}\frac{dx}{d\nu'} \\ &= \sum_{n=1}^{\infty} \frac{-1}{\kappa_n} \left[-\frac{4}{\xi^2} J_n^2(z_x) + \left(2 + \frac{x(\nu')^2}{1 + x(\nu')} \right) (J_{n+1}^2(z_x) + J_{n-1}^2(z_x) - 2J_n^2(z_x)) \right] \end{aligned} \tag{6.32}$$

Of course this is the rate per unit time, per unit volume. A correct normalisation with respect to LUXE simulations would require analysis of the laser spot size and electron-beam bunch size, and their mutual overlap. This is not attempted for this analysis. A free global scaling parameter is added for the purposes of the fitting to the reconstructed electron spectra. We convert from the photon energy to electron energy, using $E_\gamma = E_{beam} - E_{e^-}$. The only remaining free parameter for fitting is ξ. We attempt to fit the spectrum, and then can read the best-fit-ξ, and compare the performance to

the truth-level Monte Carlo ξ distribution. First, the plotted functions (for harmonics $n \leqslant 20$) are shown for four ξ points of 0.15, 0.5, 1.0, 2.0 in Figure 6.13. The dW/dE_{e^-} scale is arbitrary, including with respect to each of the other plots in the same figure. With rising ξ, one can of course see the shifting of the Compton edge to increasing energy (a red-shift in the photon spectrum). Within these analytical spectra the higher harmonic edges are visible and their size compared to the $n = 1$ edge increases too.

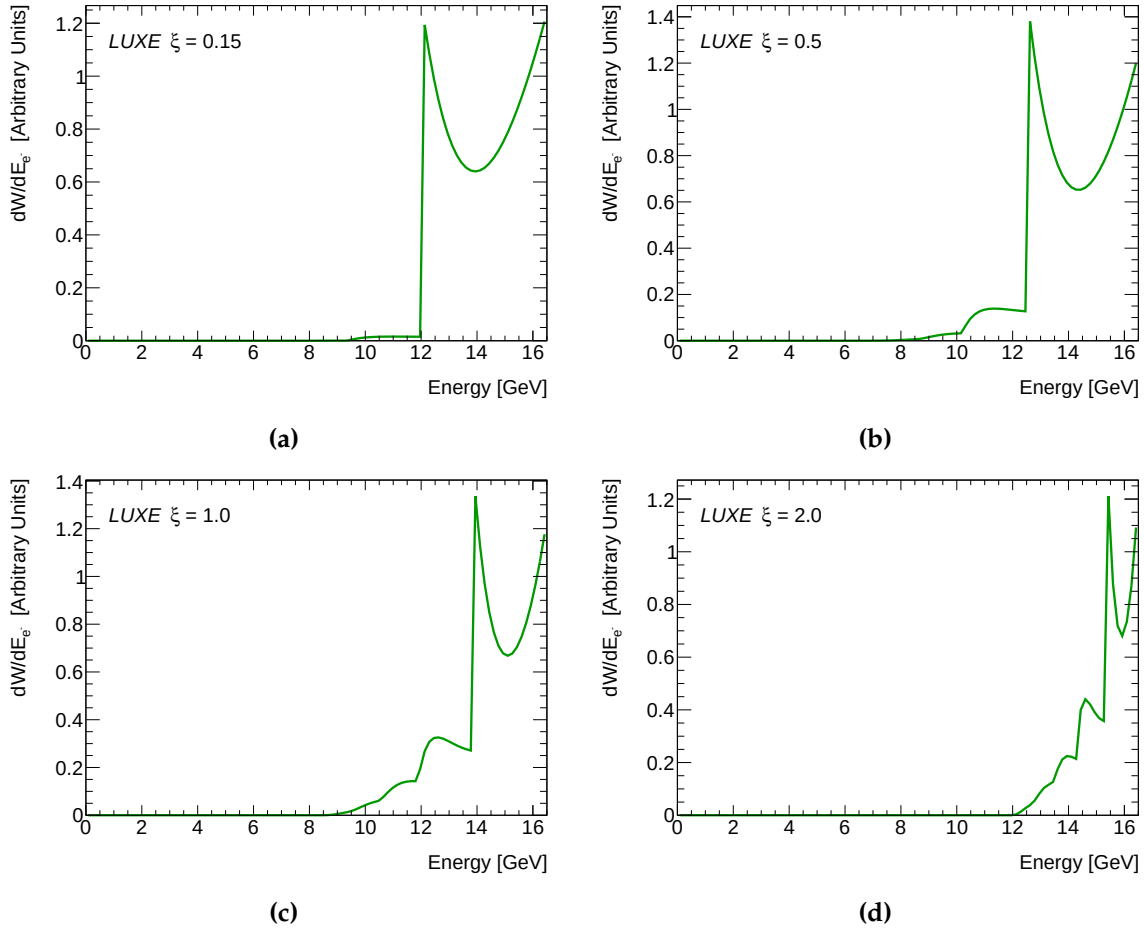

Figure 6.13.: Plots of the differential probability (per unit time, volume) of non-linear Compton scattering with respect to scattered electron energy. Shown for four different ξ values of 0.15, 0.5, 1.0, 2.0 in **(a)**, **(b)**, **(c)**, **(d)** respectively.

The function is fit to the results of the PTARMIGAN MC simulation passed through the GEANT4 scintillator detector simulation and reconstruction, as before. Each of the following is the fit to the accumulated reconstructions of 100 bunch-crossing simulations. There is no foreseeable advantage to making these full-function fits on a shot-by-shot basis, and (the current implementation of) the fitting process requires far more time than 1 Hz allows. Fits are made to these reconstructions, simulating the

LUXE IP at a ξ_{max} of 0.15, 0.2, 1.0, 2.0 (as was seen in Figure 6.13), among others. The fits are shown in Figure 6.14. The only fits which were found to be convergent, and so sure that a minimisation had been reached, were for $\xi_{max} = 0.15,\ 0.2$. It should be noted that this is not unexpected; the actual distribution being reconstructed by the detector is a distortion of this ideal single-ξ function. The actual distributions are represented in Figure 5.1. Nevertheless we try to make the fit in the assumption that for some simulations, especially at low ξ, the distribution of ξ experienced by the electron beam is relatively constant and so the spectrum approximately fits.

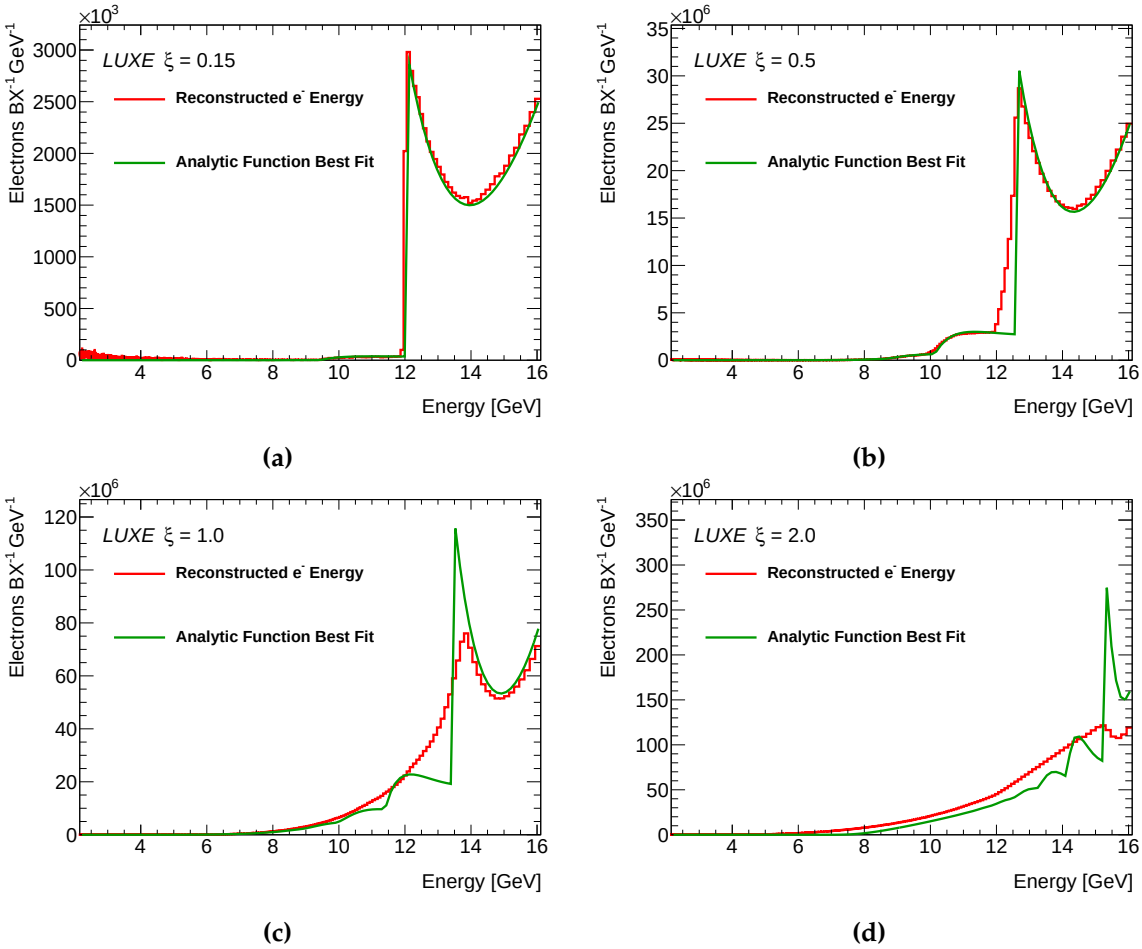

Figure 6.14.: Reconstructions of 100 bunch-crossing spectrum reconstructions from the GEANT4 scintillator screen and camera system, fit with the differential non-linear Compton scattering probability function for final electron energy. Shown for four different ξ_{max} values of 0.15, 0.5, 1.0, 2.0 in **(a)** **(b)**, **(c)**, **(d)** respectively.

Although these efforts have only found convergence in the fitting process for $\xi_{max} = 0.15,\ 0.2$, by eye the fits of some other spectra look relatively close - in particular, as seen in Figure 6.14b. This is evidenced by the fact that the retrieved ξ parameter

of the fit was 0.4675; a discrepancy to the true ξ_{max} of 6.5%. A plot of the results of reconstructions for each of ξ_{fit}, ξ_{max} and ξ_{mode} for 11 truth ξ_{max} points is included in Figure 6.16. We cannot expect the best-fit result to perfectly track the ξ_{max} of the simulation; this is by definition the maximum intensity achieved, and the rest of the actual distribution at the point of non-linear Compton emission will affect the fit, and it will strictly do so by pulling down on the ξ fit parameter, such that $\xi_{fit} < \xi_{max}$. As was shown in Figure 6.9, there are distributions of the ξ value at the vertex of each Compton interaction from PTARMIGAN. These are shown alongside the ξ_{fit} parameter retrieved from the fits for a selection of simulations in Figure 6.15.

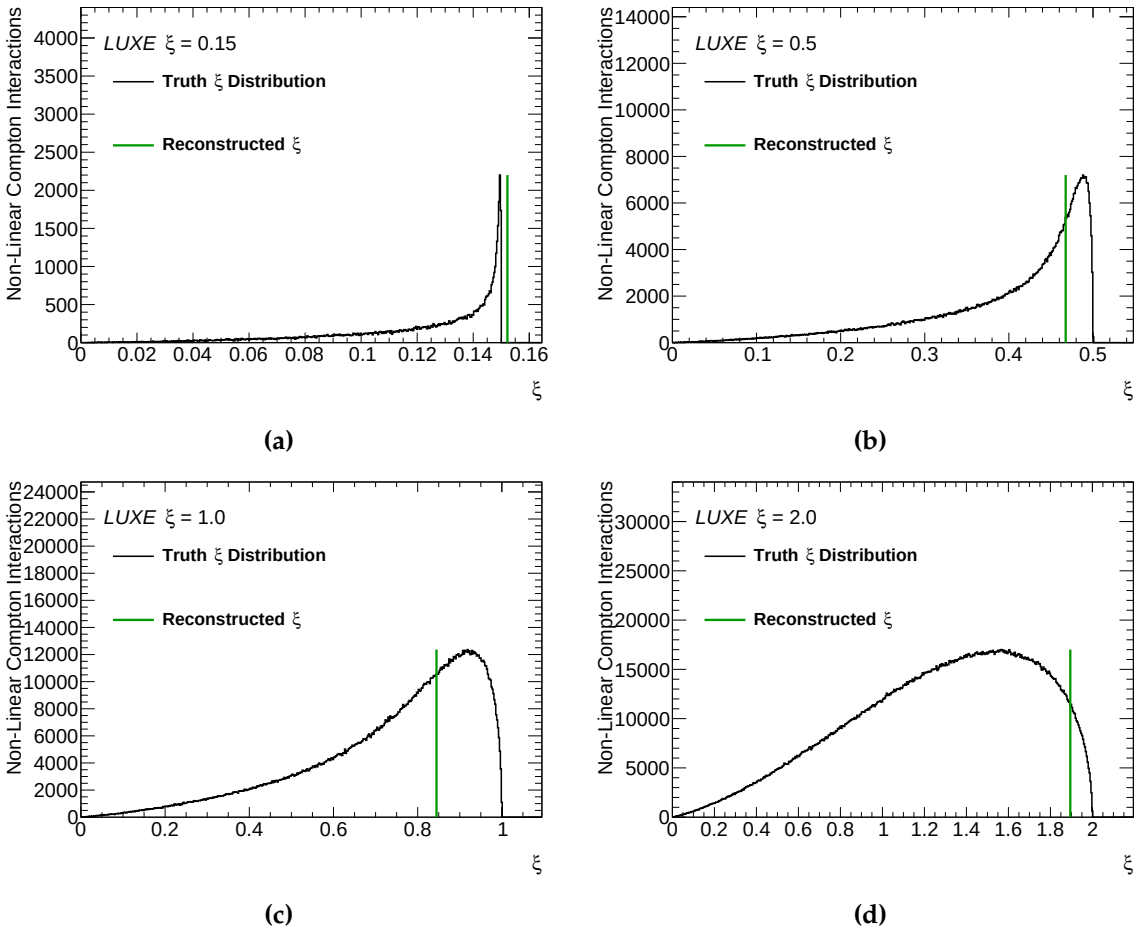

Figure 6.15.: Truth-at-Monte-Carlo-level ξ distributions at the vertex of Compton interactions from PTARMIGAN, for the sum of 100 bunch-crossings at a specific ξ_{max}. The extracted ξ_{fit} parameter is also shown, from the full-function fit of (100 bunch-crossings of) detector reconstructions of the electron spectra. Shown for four different ξ_{max} values of 0.15, 0.5, 1.0, 2.0 in **(a) (b)**, **(c)**, **(d)** respectively.

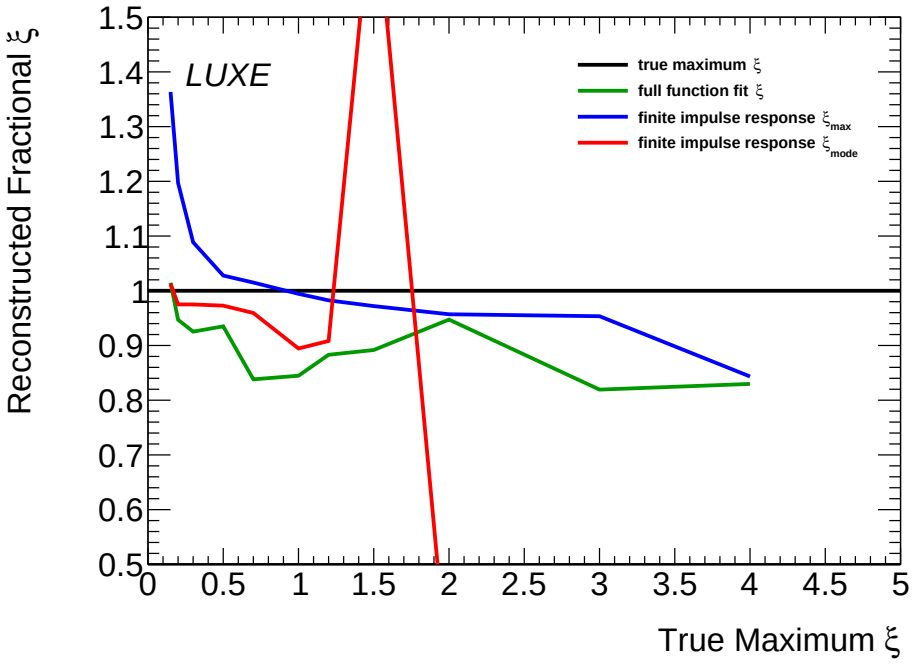

Figure 6.16.: Reconstructed ξ values as fraction of a true ξ_{max}, for simulations of various ξ_{max}. These values are those resulting from attempts to fit the reconstructed electron energy spectrum with a function, and a finite-impulse-response analysis of the same spectrum. Each distribution was the sum of 100 bunch-crossings of data, using PTARMIGAN simulations with the phase-0 laser.

6.4. Phase-I Laser Interactions

The majority of analysis performed using the simulations here deal with use of phase-0 of LUXE, using the lower-power 40 TW JETI-40 laser system. The reason for this is simply that the phase-0 comes first, and so simulation efforts started in this regime.

The phase-I laser improves on the total shot energy by a factor of ~ 8. This allows attainable values of ξ_{max} much higher than possible with the JETI40 laser. As we have seen, these higher values do not allow for reconstructions of the electron spectra to be analysed well; whether that means analysing the shifting Compton edge (which leaves the detector acceptance at $\xi_{max} \sim 4.0$) or fitting smeared energy-differential spectra. This can be further exacerbated in phase-I simulations as the contribution to smearing from beam electrons emitting multiple times increases. Of course, the electrons which have already emitted once no longer share the same initial momentum and so the spectrum calculated for a monochromatic beam is not valid. On the other hand, with more energy available in a single shot, the problem of a non-constant ξ distribution

is ameliorated compared to the JETI40 laser, if they are focussed for similar ξ_{max} (noticeable when the laser spot in phase-I is larger than the electron beam).

An example of reconstructions of the electron energy spectrum for various SFQED interactions, using the previously described PTARMIGAN to GEANT4 to reconstruction pipeline, and with the superior phase-I laser, are shown in Figure 6.17. Each of the reconstructions are for one single bunch-crossing and plotted alongside the incident simulation 'truth' spectrum. The selection of ξ_{max} is the same as Figure 6.6, allowing a direct comparison. Though the spectra are essentially unchanged for lower ξ_{max}, in the plot shown in 6.17c at $\xi_{max} = 2.0$, the primary Compton edge is far more pronounced in the phase-I case.

Fitting of the previously derived energy-differential probability rate can be performed with the phase-I simulations. These are shown in Figure 6.18. Many of these fits are as poor as the phase-0 attempts, highlighting the distortion of the spectra from multiple-emission electrons. Yet, for the low-ξ region, convergence is found in the fitting process up to $\xi_{max} = 0.7$. As we expect given the improved prominence of the edge, analysis of the Compton edge in these phase-I laser simulations gives superior reconstructions of the ξ_{max}, particularly in the mid-ξ range. These are shown in Figure 6.19, alongside the full-function-fit ξ parameters and the underlying truth ξ distribution. The exact values can be seen in Table D.2.

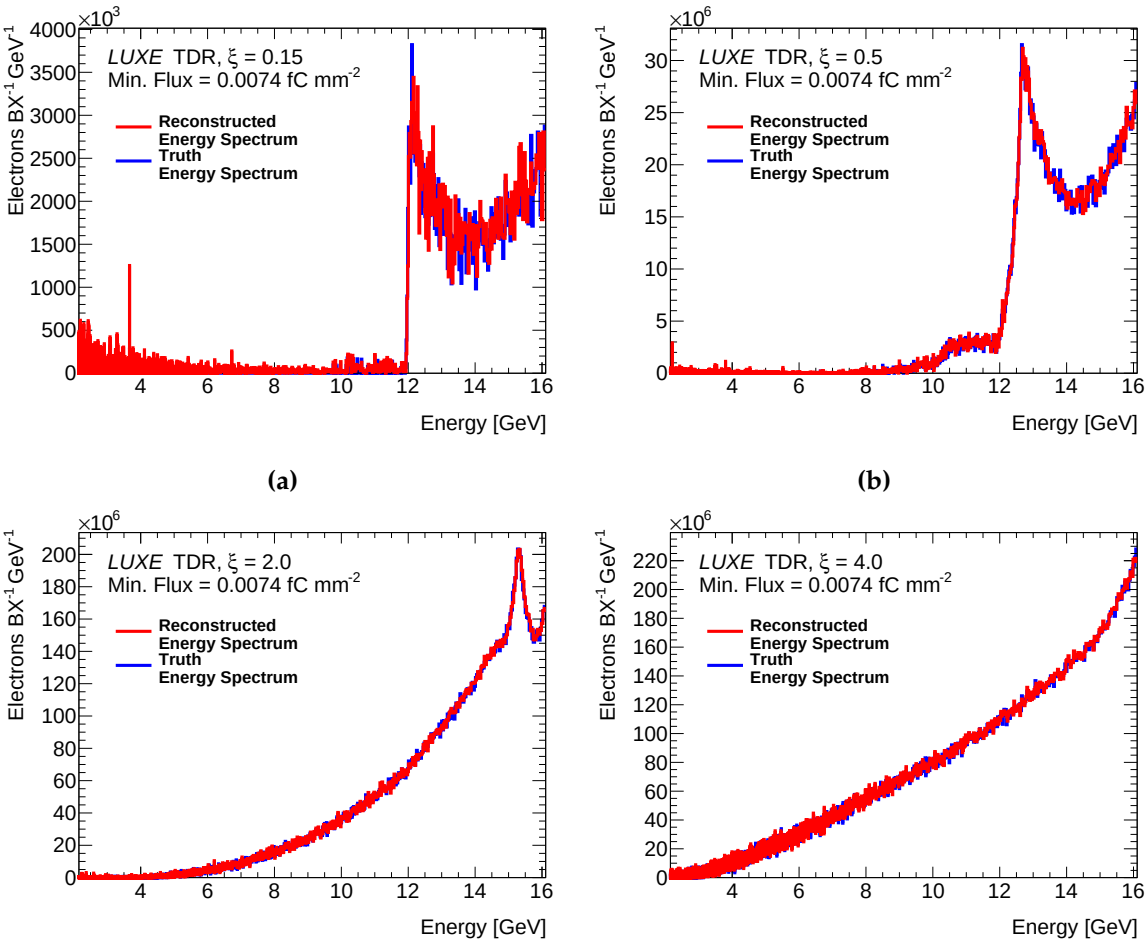

Figure 6.17.: **(a)** A reconstruction of a single-shot example SFQED electron spectrum, from PTARMIGAN, in this instance using the phase-I laser, with $\xi_{max} = 0.15$ using the GEANT4 simulation of the screen and camera system. This uses a threshold-of-sensitivity value (wherein no signal data at on-screen flux lower than this is used) of 0.0074 fC mm^{-2} in the reconstruction. The effective resolution used for this simulation is 200 µm. **(b)** Shows a similar analysis for a PTARMIGAN simulation with larger value of $\xi_{max} = 0.5$. **(c)** and **(d)** show reconstructions for the $\xi_{max} = 2.0,\ 4.0$ PTARMIGAN simulations respectively.

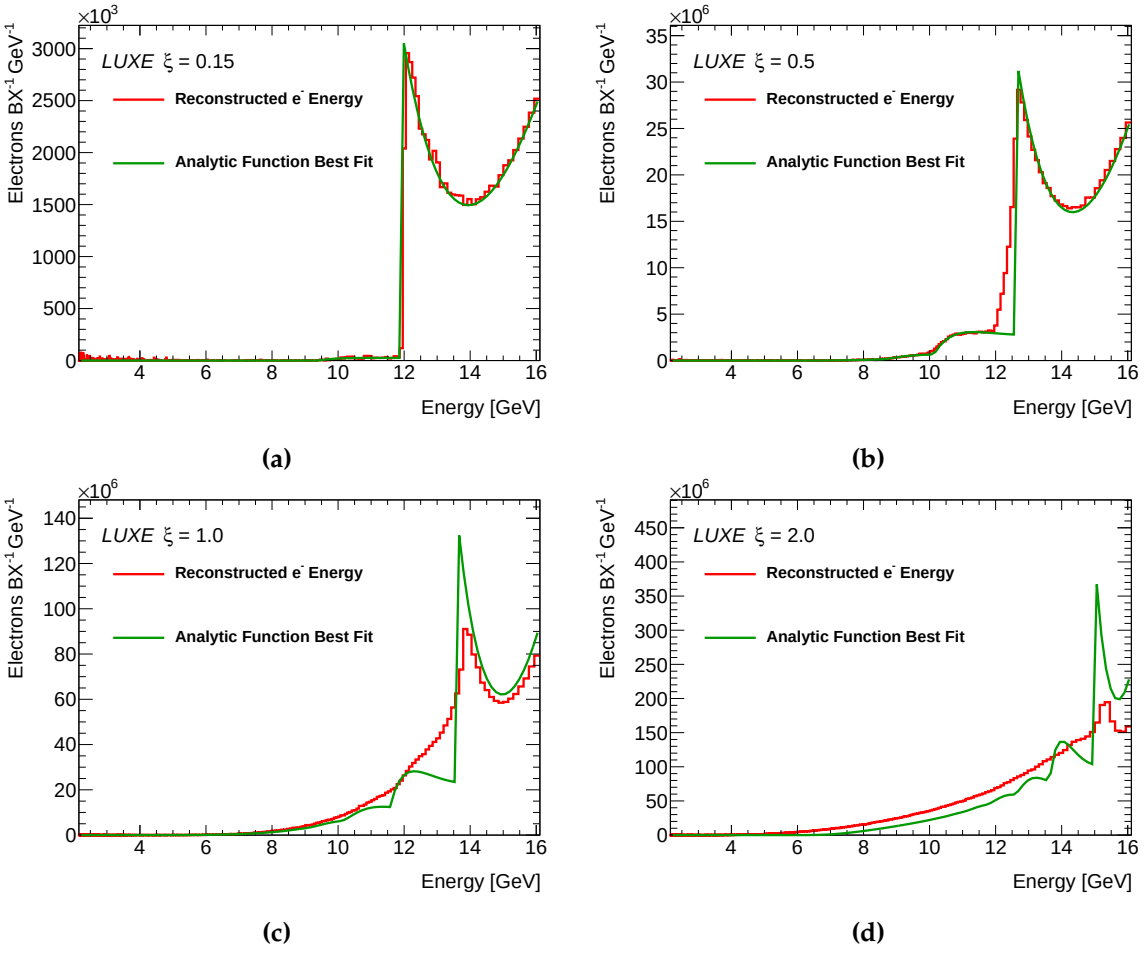

Figure 6.18.: Reconstructions of the electron energy with the sum of 10 bunch-crossing spectrum reconstructions from the GEANT4 scintillator screen and camera system, fit with the differential non-linear Compton scattering probability function for final electron energy, using PTARMIGAN simulations of the phase-I laser. Shown for four different ξ_{max} values of 0.15, 0.5, 1.0, 2.0 in **(a)** **(b)**, **(c)**, **(d)** respectively.

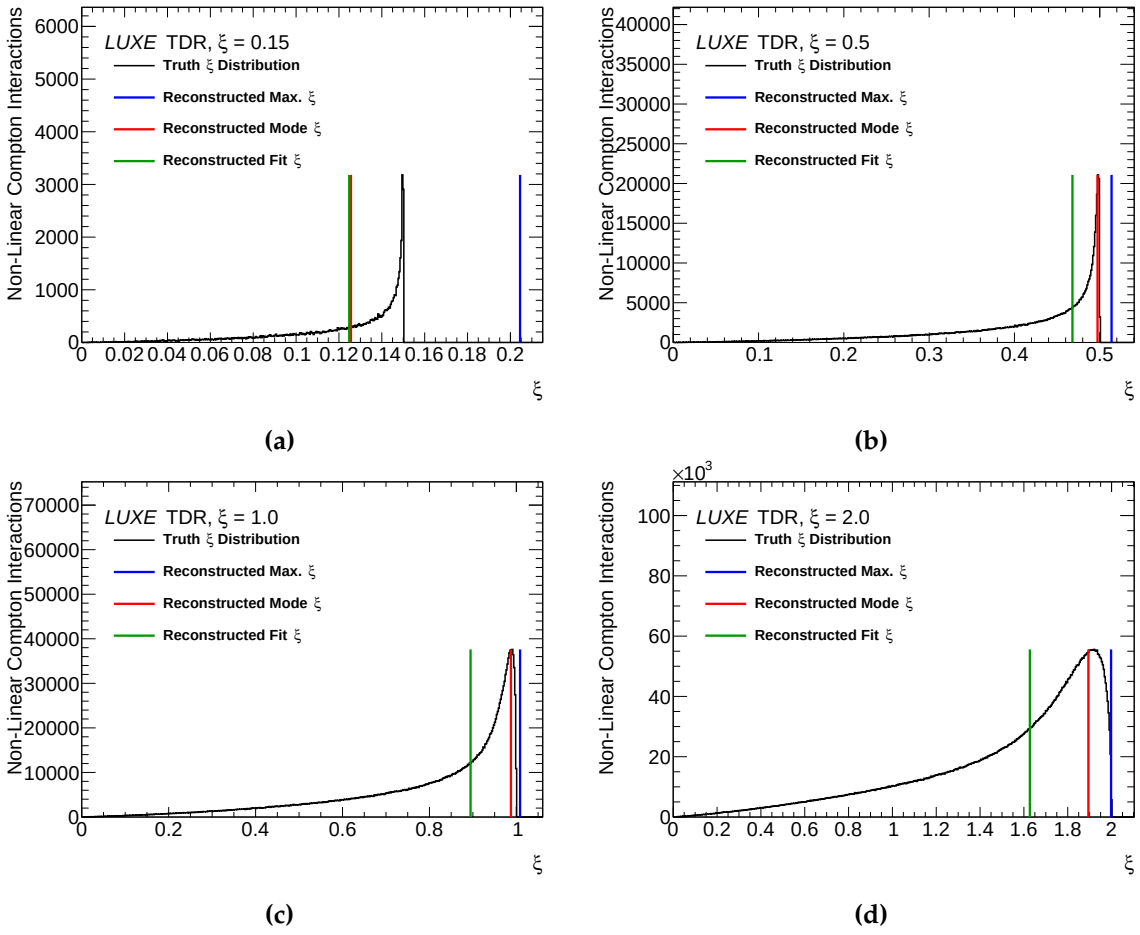

Figure 6.19.: Truth-at-Monte-Carlo-level ξ distributions at the vertex of Compton interactions from PTARMIGAN, for the sum of 100 bunch-crossings at a specific ξ_{max} for the phase-I laser. The extracted $\xi_{\texttt{fit}}$ parameter and ξ_{max}, ξ_{mode} from the Compton edge are also shown, from the analysis of (100 bunch-crossings of) detector reconstructions of the electron spectra. Shown for four different ξ_{max} values of 0.15, 0.5, 1.0, 2.0 in **(a)** **(b)**, **(c)**, **(d)** respectively.

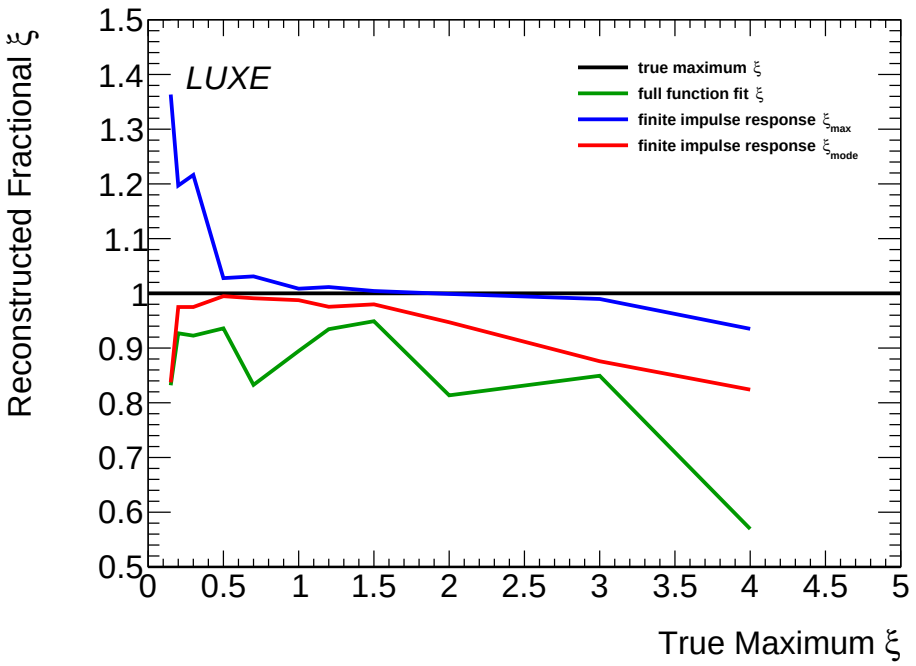

Figure 6.20.: Reconstructed ξ values as fraction of a true ξ_{max}, for simulations of various ξ_{max}. These values are those resulting from attempts to fit the reconstructed electron energy spectrum with a function, and a finite-impulse-response analysis of the same spectrum. Each distribution was the sum of 10 bunch-crossings of data, using PTARMIGAN simulations with the phase-I laser.

Chapter 7.

Scintillation Screen & Camera Detector System in Test-Beam

A prototype of the scintillator screen and camera system was constructed. This involved two each of the relevant components defined in Chapter 5:

- the GadOx screen, in a $10\,\text{cm} \times 10\,\text{cm}$ square;
- the cameras, of models both 2K and 4K;
- the lenses, of focal length $f = 50\,\text{mm},\ 75\,\text{mm}$;
- and the band-pass optical filter.

Unlike the rigidly defined geometry in Chapter 5, the cameras (with attached lens and filter) remain dynamic with respect to the screen's position – this prevents conflicts with the space constraints of testing areas.

7.1. 2022 Test-Beam Overview

The prototype of the scintillation screen & camera system was tested in a non-user-facility electron beam – hereafter referred to as 28m – at DESY [98]. This facility used the laser-plasma technique to create electrons via ionisation and then, using the wakefield of the plasma stimulated by laser propagation, accelerate a bunch of electrons. A photograph of the experimental setup within 28m – alongside other detectors sharing the same beam-time – is given in Figure 7.1, and a top-down view of the apparatus (including select dimensions) is in Figure 7.2.

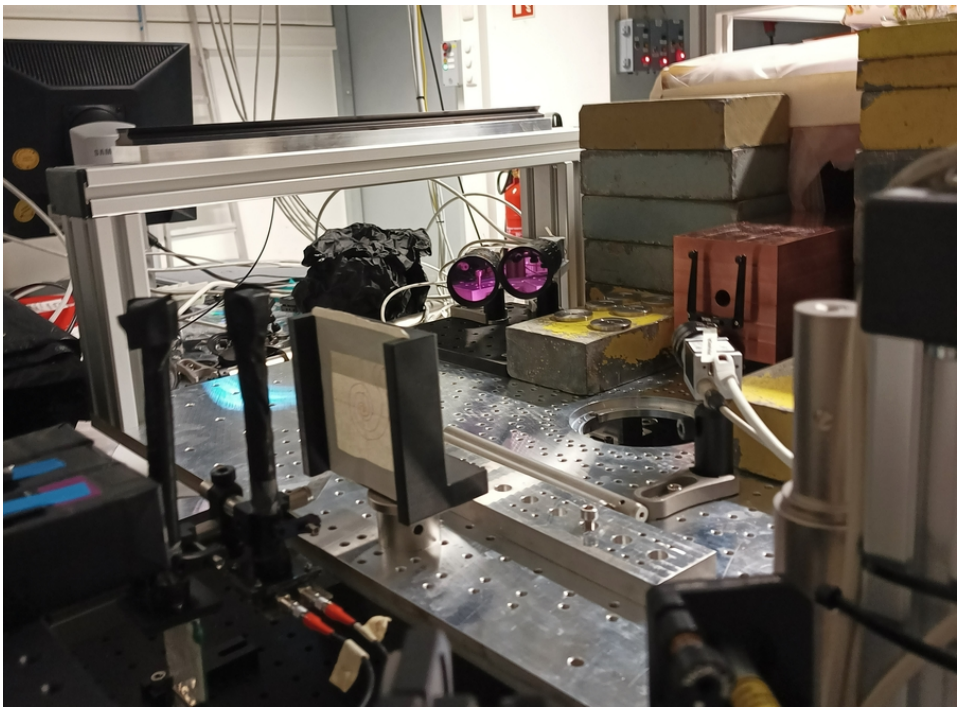

Figure 7.1.: A photograph of the experimental setup in the DESY laser-plasma accelerator 28m lab. On the right hand side lies a 1cm-diameter collimator, from which the beam emerges, before reaching the screen in a black plastic frame, in front of Cherenkov detector straws [70] and lead-glass calorimeter blocks [99]. Two cameras, triggered by the accelerator laser-clock and fitted with filters which appear purple, collect the light.

The four components of note are:

- the accelerator and beam (including an internal beam charge diagnostic detector);
- a lead collimator, with diameter of 1 cm;
- the scintillator screen, 396 mm downstream, kept in a plastic holding frame, with its normal in the centre of the beamline;
- the two cameras, one 2K and one 4K model, with their respective lenses and band-pass optical filters, aimed at oblique angles at the screen.

Bunches of electrons, with associated trigger from the laser, were generated at a rate of 3.3 Hz. Upon the delivery of each bunch, the trigger was passed to each camera and an image of exposure time 3 ms was recorded. An example of accumulated signal image and a profile in one dimension are given in Figure 7.3; these represent the sum of 4000 bunches / images. The full-width at half-maximum (FWHM) of the profile in the y dimension in Figure 7.3b is measured as 343 pixels. Using the working

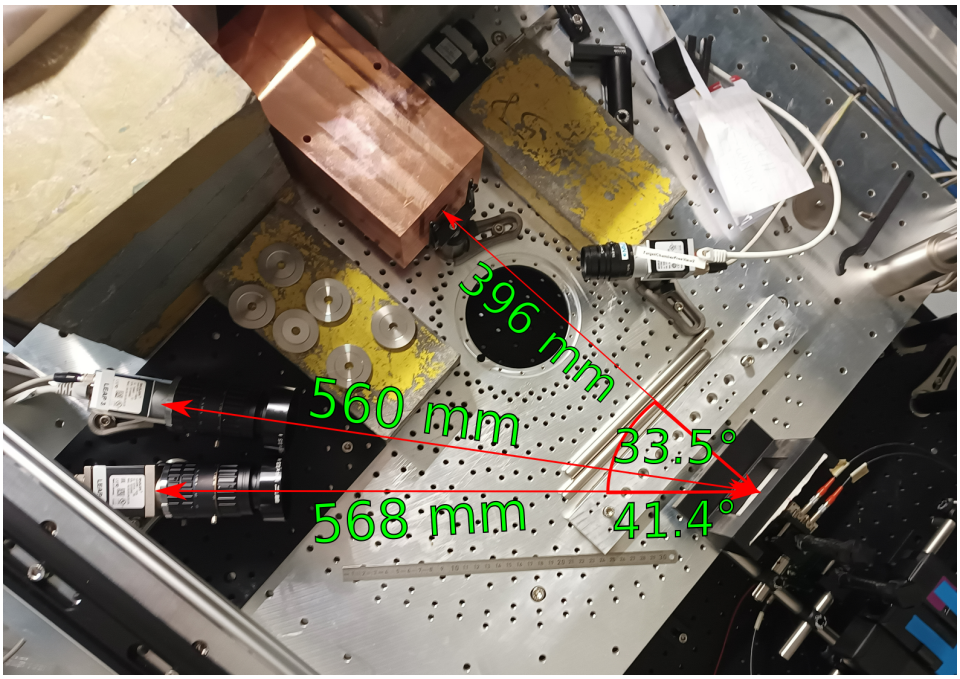

Figure 7.2.: A top-down view of the setup in the DESY laser-plasma accelerator 28m lab. Alongside are measurements of the distance (and angle) between the centre of the screen (or its normal) and lens of the cameras.

distance(s) shown in Figure 7.2 the resolution of the images in terms of area of the screen's surface per pixel is calculable. The pixel pitch in the camera used for Figure 7.3b (2K) corresponds to 46.54 µm distance on the screen covered per pixel (with the 4K camera covering 17.5 µm on-screen). This gives a calculated full-width at half-maximum of the peak of signal distribution of around 1.6 cm. Given the diameter of the collimator is just 1 cm, this represents some considerable beam-spread between the collimator and screen.

The aim of the beam-time was to ascertain, as much as possible within the set-up, two items: the charge-flux incident on-screen which would induce signal in the camera sensor similar to noise levels; and the effective dynamic range of the combined two-camera system in terms of on-screen charge-flux.

7.2. Beam Characteristics

The bunches from this beam exhibited some variance in energy between 60-70 MeV, but the average response of the screen is not expected to depend on energy in this

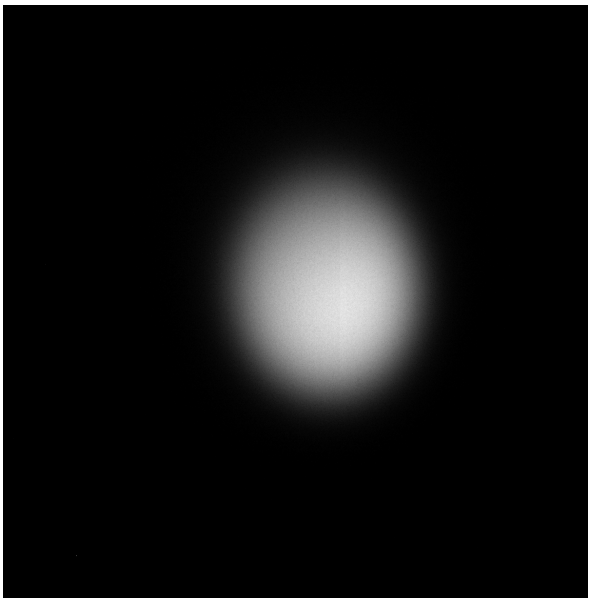

(a)

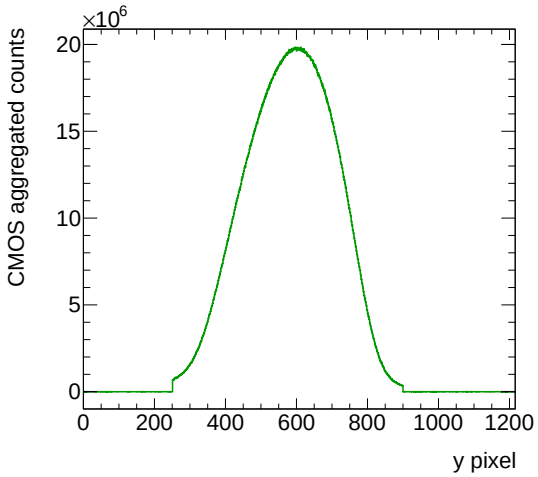

(b)

Figure 7.3.: **(a)** shows an accumulated image for 4000 beam bunch events, having subtracted dark-noise images, as taken by the 2K camera. The intensity scale is arbitrary for visibility. In **(b)** are the aggregated CMOS counts in each pixel of the same data set in the y dimension, having subtracted a background profile. Here the limits of the Area Of Interest, a selection of a portion of the image containing the beam-induced light, are visible.

range (explained by Equation 5.5 and evidenced by tests in simulation in GEANT4). The bunch-to-bunch charge varies much more, and the screen response then varies linearly with the incident charge.

In the beam area two charge diagnostics were running, allowing reconstruction of the charge of individual bunches. The technology chosen is a Damon dark-current detector, which measures the charge non-destructively, and is located within the beampipe upstream of the collimator [100].

This detector uses the principle of resonant potential differences appearing in a metal cavity; often this is stimulated by radio-frequency photons in order to accelerate charged particles. In this detector, passing charge bunches induce a sinusoidal potential difference, the peak amplitude of which depend on the total charge. Using electrical antennae to measure this potential difference the passing charge is reconstructed.

The measurement consists of two antennae, one configured to measure, in principle, charges above 1 pC; and a second antenna intended for detection below this value. Reconstructions of the charge from the raw current data from the antennae have some

significant tension; in the region where both antennae are sensitive, the reconstructions from the antenna intended for lower charges presented a roughly 60% higher value. One or both of the two reconstructions then has drifted from their once-accurate calibration parameters. Hereafter the calibration correlating to the higher-charge-range-antenna is used for calculations, as this exhibited a saturation effect at an absolute value as expected around 0.5 pC (and therefore is less likely to have suffered major drift in its detection response). This tension still represents a large qualitative uncertainty in the charge reconstructed bunch-to-bunch. This is in addition to the considerable shot-to-shot variance of the measurement itself, and the loss of some unknown fraction of the charge due to the edges of the collimator. In light of these compounding effects, an effective upper and lower bound are given to the calculation of values dependent on the bunch-charge. These are chosen as $\pm 50\%$.

The pointing of the laser-plasma accelerated beam was unreliable. Because the beamline is outfitted with a collimator of diameter 1 cm, the on-screen charge was highly dependent on this pointing, and had an inextricable effect invisible to the charge diagnostics due to the fact they were positioned before the collimator. The laser-plasma acceleration pointing problem was mitigated in some of the runs performed, using a plasma-lens within the accelerator to better align the beam. This came at the drawback of a lower maximum bunch charge. Plots showing the correlation between the screen and camera system signal – integrated over an Area Of Interest (AOI) within the image – versus the charge diagnostic measurements are shown in Figure 7.4. The difference between the two cases is very clear, with very little correlation between the measured camera signal and bunch-charge in the no-plasma-lens case; but an acceptable correlation is seen in the case when the plasma-lens is used. The improved reliability of the pointing of the beam proved to be be essential, and only data taken when using the plasma-lens was chosen for analysis.

7.3. Analysis

It should be noted that, specifically for the analysis pertaining to on-screen charge flux, the geometry of the cameras with respect to the screen is unimportant. The reconstructed minimum detectable flux is independent of the screen-to-lens distance, as well as the angle between the normal of the screen and the optical line. Increasing the optical distance reduces the solid angle covered by the lens by factor $1/r^2$, reducing

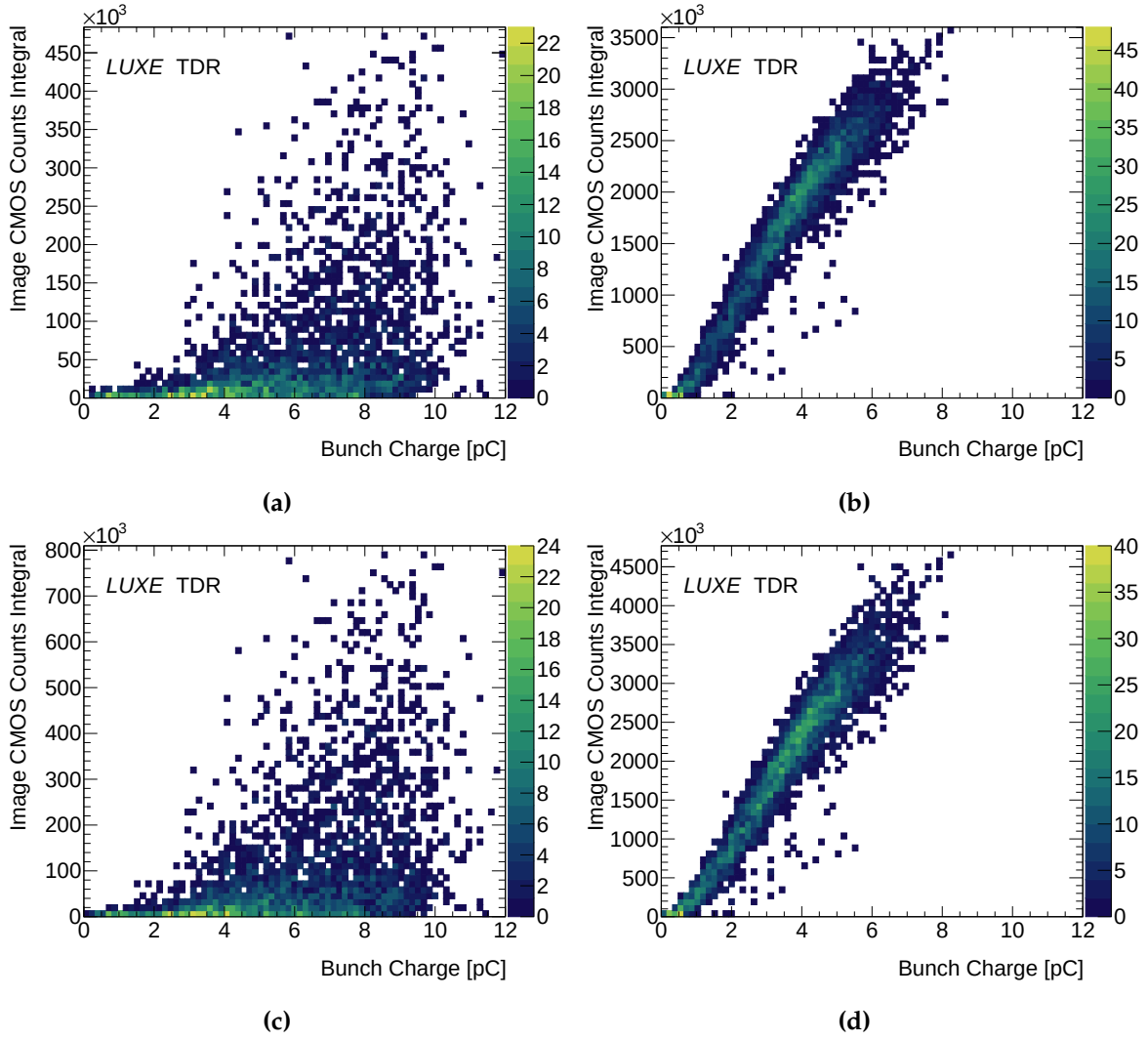

Figure 7.4.: The correlation between the integral of digital signal, in terms of CMOS counts within each camera, with the reconstructed incident bunch charge. Plots **(a)** and **(c)** do not use the focussing plasma-lens element, while **(b)** and **(d)** do. The 2K camera data are given in **(a)** and **(b)**; **(c)** and **(d)** follow the same pattern for the same beam-runs but as measured by the 4K camera.

signal levels; but the area of the screen covered by one pixel, or some AOI of the sensor, increases by a factor r^2, and so they cancel. The light emission of a flat screen is described by a Lambertian distribution, meaning it reduces with factor $\cos\theta$, where θ describes the angle between the optical line and the normal of the screen. At the same time, the shape of the beam-spot in the camera image compresses in one dimension, again effectively increasing the light-per-pixel by a factor $1/\cos\theta$. With this in mind the value for threshold-of-sensitivity on-screen charge flux deduced from this test-beam is applied directly to the system in LUXE, as it is independent of r & θ. This

value does still depend on the optical and electronic components, and so different values for the 2K and 4K camera are presented.

7.3.1. Background Subtraction

In each of the graphics in Figure 7.4 the measurement of the integral of CMOS counts is calculated with sufficient background subtraction, thereby centring the measurement of no beam to equal (on average) zero. The background evaluation was performed by taking simple dark images. The integral of CMOS counts in the AOI of these dark images (actually not in complete darkness, but rather directly in the same experimental setup but with no beam) are plotted in histograms in Figures 7.5a & 7.5b for each camera model. These represent the trend of 500 images each. The ambient light of the dim experimental area is present and therefore automatically accounted for. It is clear to see that the sum of this noise in all the pixels follows a Gaussian distribution; the several million pixels' noise is highly correlated with one another, as one might expect for microscopic active elements extremely close to one another, and do not act independently. For all measurements of the 'signal', that are sums of the CMOS counts, a subtraction of the mean of the Gaussian fit as seen in Figures 7.5a & 7.5b is performed. This is done only with dark and signal images of identical optical and electronic settings, and of course only with identical AOIs defined between them. As explained, slices of Figure 7.4 are fit with a Gaussian function; examples of such fits for the charge interval between 4 and 5 pC in each camera are shown in Figures 7.5c & 7.5d.

7.3.2. Signal per pC On-Screen Charge

The equation for integrated CMOS counts per pC on-screen charge is calculated by fitting slices of the data in Figure 7.4 in the x axis with a Gaussian function. Given the pointing of the beam will lead to the loss of some portion of the charge, likely proportional to bunch size, and there will continue to be charge loss along the beamline, an estimate of the signal/charge is taken slightly above the mean of the distribution. The best estimate for the true CMOS-counts-integral for some on-screen charge is estimated as the mean of the Gaussian plus one standard deviation. These values are fit with a linear expression. The profile of this sum for the slices throughout the bunch-charge is shown in Figure 7.6. The fit is made to each point, with a weighting

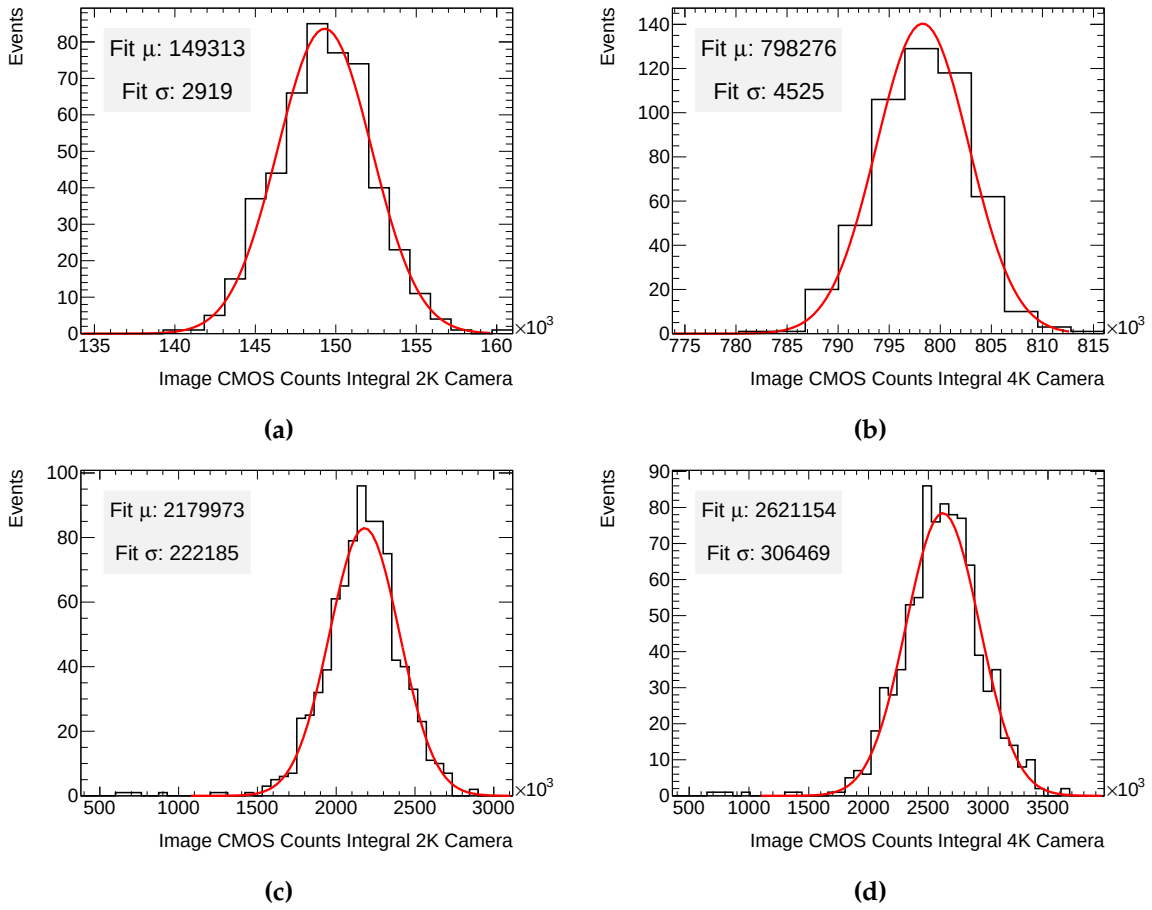

Figure 7.5.: Distributions for the integral of CMOS counts in dark (top) and signal images (bottom), for both camera models. **(a)** and **(c)** show the data from the 2K camera; **(b)** and **(d)** give the 4K camera results. They are each fit with a Gaussian function in red. The central value and standard deviation, μ and σ respectively, are parameters of the fit. The signal distributions include the subtraction of the central value of background for each camera.

inversely proportional to the point's error bar, which is generated from the quality of the original Gaussian function fit. The linear fit is used to gather a single value for the gradient. It is expected the non-linearity in the profile in Figure 7.6 is principally due to effects from the beam, collimator, and charge measurement, rather than the scintillator screen and cameras. Such non-linearity is reasoned to be due to the increasing bunch charge resulting in a physically larger bunch, being trimmed more by the physical limits of the collimator. As explained the calibration of the charge reconstruction may have drifted, which will contribute too to non-linearity. It is seen in simulation that there is very good linearity in the response of the screen to on-screen charge, and from

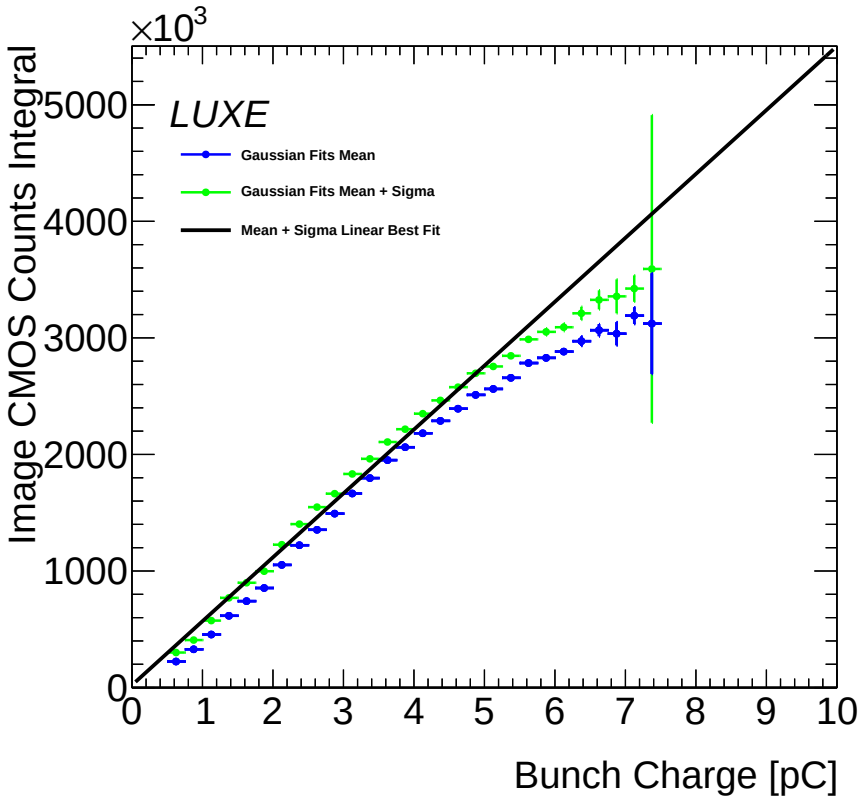

Figure 7.6.: The profile of the means, plus 1 standard deviation, of the Gaussian fits of slices of the 2K camera's response to on-screen charge. This sum, used for the linear fit, is represented by the green points. For comparison only the central value of the Gaussian function is plotted in blue. The fit is performed with weightings for each point inversely proportional to the size of the error bars, and not fixed to the 0,0 point, in order to best estimate the overall gradient of the data.

the documentation it is expected the camera sensors exhibit good linearity too (Figure 5.14).

The correlated response of both cameras to one another event-by-event is shown in Figure 7.7, showing the improved closeness to linearity. This is the response, minus the relevant dark image pedestal, of each camera event-by-event. This does not account for the response of the screen to incident charge, as each image from each camera is recording the same light from the screen in response to one electron bunch. Perfect linearity will not ultimately be necessary for the combined system, so long as the actual response is well-described by a light-charge calibration curve.

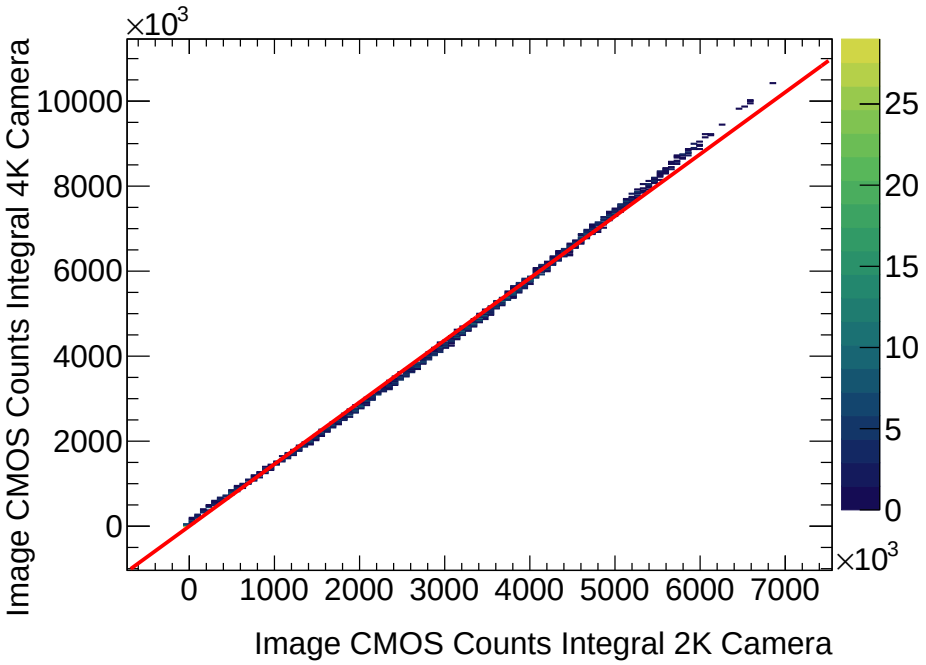

Figure 7.7.: The correlation of the two camera models in response to shot-by-shot on-screen charge. A simple linear fit is shown for comparison, constrained to intercept the 0,0 point, expected in the ideal case of this relationship (and the line is displayed for comparison, not to extract quantitative results).

7.3.3. Minimum Detectable Flux Calculation

The gradient of the linear fit of Figure 7.6 is then compared to the variance of the integrated CMOS count of the AOI in dark images in Figure 7.5. The required charge to equal the standard deviation of the integrated CMOS counts (i.e. the point at which signal to noise ratio equals one) is then calculated. This is divided by the screen area covered by the AOI to retrieve an estimate for the flux at threshold of sensitivity. However, charge-flux incident on the screen at or above these values are not necessarily visible in the image; that depends on whether the flux falls within the window of dynamic range, which is dependent on the gain of the sensor(s).

The reconstructed values for the minimum detectable flux are shown in Figure 7.8, with the associated uncertainty of $\pm 50\%$, for various values of electronic gain. It is expected that the trend through the gain is relatively flat. The linear trendlines in Figure 7.8 shown follow this understanding approximately, but the limits of the data available do not allow more conclusive statements to be made. Upper and lower bounds on the threshold-of-sensitivity flux (the mean for all values of gain) are also

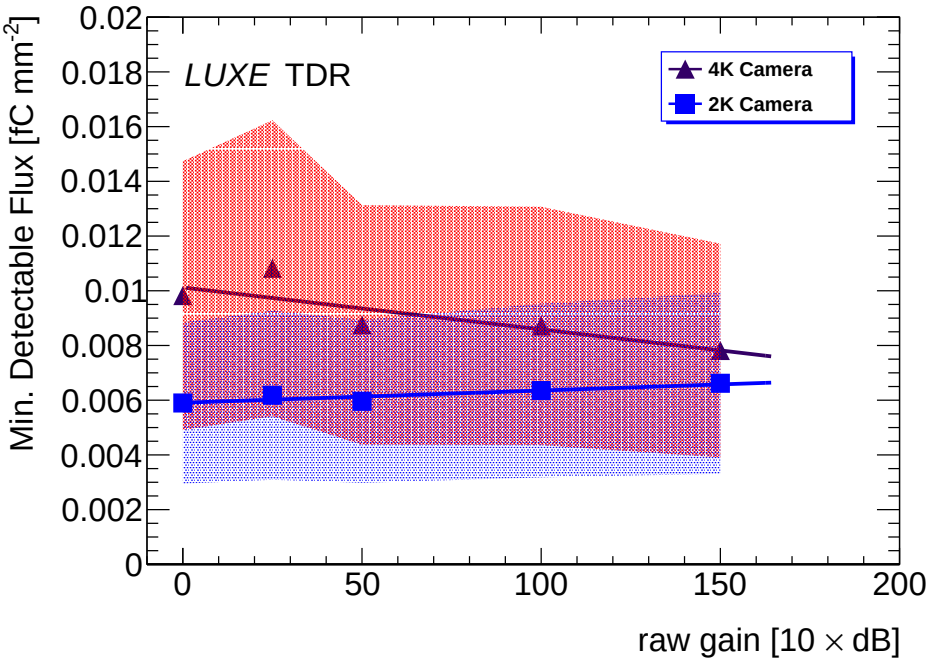

Figure 7.8.: Plotted values for the reconstructed values of minimum detectable on-screen charge flux. The red/blue shaded areas show the estimated region for the 4K/2K camera (respectively) including the $\pm 50\%$ error bands. This is performed with the plasma-lens-enabled data set, for varying values of electronic gain. The 'raw gain' value is equivalent to the power-gain in dB multiplied by ten.

given in Table 7.1. The 2K camera and its optics are shown to be more sensitive (resulting in a lower threshold) in this respect.

Table 7.1.: Reconstructed minimum detectable flux for each camera.

Minimum Detectable Flux	Upper Bound	Central Estimate	Lower Bound
4K Camera [fC mm^{-2}]	1.398×10^{-2}	9.32×10^{-3}	4.662×10^{-3}
2K Camera [fC mm^{-2}]	1.11×10^{-2}	7.397×10^{-3}	3.698×10^{-3}

7.3.4. Optical Filters Comparison

A simple comparison of the use of the optical band-pass filters, intended to reduce ambient light, was made. The result of the calculated value of the integrated CMOS counts per pC charge were compared for: the high-quality optical filter chosen for

this system in LUXE at central wavelength 543 nm; a less expensive filter of the Machine Vision filter [101] range from Edmund Optics; and no filter fitted. Unlike the absolute values of these reconstructions, when comparing the results of differing filters relative to one another the problem of a consistent unknown charge calibration factor effectively cancels. The relative comparison for each case is given in Table 7.2. Comparing the band-pass 543 nm filter to no filter used, roughly 42% of the original scintillation light is transmitted when using the filter. This is compared to the reduction in CMOS counts in dark images of $\sim$22% when using the filter. A proportion of this value is electronic noise rather than ambient light, so the rejection of ambient light by the filter is strictly better than 78%, and so more ambient light is absorbed compared to the scintillation light (58%).

Table 7.2.: Relative camera CMOS counts per pC and dark image pedestals for optical filter variations.

Signal	543 nm Filter	Machine Vision Filter	No Filter
4K CMOS counts per pC	6.98×10^5	-	1.67×10^6
2K CMOS counts per pC	5.46×10^5	6.96×10^5	-
Relative cc pC^{-1} Signal	1	1.27	2.4
4K dark CMOS counts pedestal	7.98×10^5	-	3.56×10^6
2K dark CMOS counts pedestal	1.49×10^5	1.93×10^5	-
Relative dark CMOS pedestal	1	1.29	4.46

7.3.5. Dynamic Range

By using the calculated CMOS counts per pC charge, and incorporating the optical parameters listed in Table 5.5, the effective upper and lower detectable flux at the limits of each camera's dynamic range were calculated. The ranges of the two cameras, which invariably share most of one another's flux-range, can be combined now into one system of effective dynamic range greater than the 12-bits associated with each camera. Dynamic ranges of the system for cameras at several gain values (where the 2K and 4K camera share a raw gain value) are given in Table 7.3, alongside the absolute upper and lower limits of flux in the range. The final entry gives an extrapolated example of the maximum achievable dynamic range, where the 2K camera is at full gain, and the 4K at the lowest setting. Each of these values, similar to the threshold-

of-sensitivity, are dependent on the charge reconstruction, and so have the associated $\pm 50\,\%$ uncertainty. As detailed in Chapter 5, there remains the option in the final system to fix the 4K camera with a further neutral-density filter, increasing the upper limit of measurable flux by a factor 4, bringing the absolute maximum dynamic range of the combined system in LUXE to 61.9 dB ($\approx 1.5 \times 10^6$).

Table 7.3.: Reconstructed dynamic ranges and the upper & lower detectable limits of flux within the range, for various values of electronic camera gain.

Raw Gain $[10 \times \text{dB}]$	Dynamic Range [dB]	Flux Lower Limit [fC mm^{-2}]	Flux Upper Limit [fC mm^{-2}]
0	44.18	2.911×10^{-1}	7.615×10^{3}
50	43.63	1.653×10^{-1}	3.816×10^{3}
100	43.33	9.914×10^{-2}	2.136×10^{3}
150	42.68	5.808×10^{-2}	1.077×10^{3}
Max. Range	55.85	1.978×10^{-2}	7.615×10^{3}

7.4. Re-application to Simulation

The results from these data were applied to the simulation of the scintillation screen and camera system and its reconstruction algorithm. This comes in the form of enforcing the dynamic range visible to the combined camera system, and emulating the sensor noise, the magnitude of which is normalised using the minimum detectable flux. The resulting effects on the reconstructed signal possible due to the noise / dynamic range emulation are plotted, using the upper, central and lower estimates for the minimum detectable flux and dynamic range (see Table 7.1). This is performed for ξ_{max} values of 0.15 and 2.0, shown in Figure 7.9.

To perform the noise emulation, a noise map is taken from real, dark images from the prototype in test-beam. The noise from one (randomly chosen) single image is added, and the normalised sum of the average of 100 of these images is subtracted, to emulate the realistic noise characteristics in the process of reconstructing one bunch-crossing. Given some value of minimum detectable flux, the corresponding dynamic range is calculated, which forms an absolute cut-off on a per-pixel basis. If the flux is below the dynamic range at one pixel, it is set to zero; if it lies above, the value is set to the top of the dynamic range. The lower limit in the reconstructions is chosen as

the lower 2K limit at gain=100; the upper limit is the 4K camera at gain=0 with the additional neutral density filter applied, increasing it by factor 4.

The absolute percentage difference between integral of the reconstruction and truth are shown in Table 7.4. In each case, the discrepancy between reconstruction and truth due to threshold-of-sensitivity / dynamic-range is low, below 1%. The only visible change to the spectra in Figure 7.9 due to changing minimum detectable flux is at the low-energy region of the $\xi_{max} = 0.15$ reconstructions. The inaccuracy of the actual value of minimum detectable flux ($\pm 50\%$ due to the charge measurement) then is shown to have little effect on the analysis of the energy spectra, as in each of the three cases reconstructions look good, and regardless of the true value the results in the previous Chapter 6 will remain accurate. The system in total is then proven to be suitable for the environment, in terms of reconstructing electron signal, of the EDS of the IP region of LUXE.

Table 7.4.: Percentage absolute difference between reconstructed spectra integral and truth integral, for the statistics of one single bunch crossing. The upper, central and lower estimates for the minimum detectable flux are used to normalise the noise emulation.

PTARMIGAN Parameters	Upper Bound	Central Estimate	Lower Bound
$\xi = 0.15$	-0.277%	0.0382%	0.353%
$\xi = 2.0$	0.42%	0.426%	0.431%

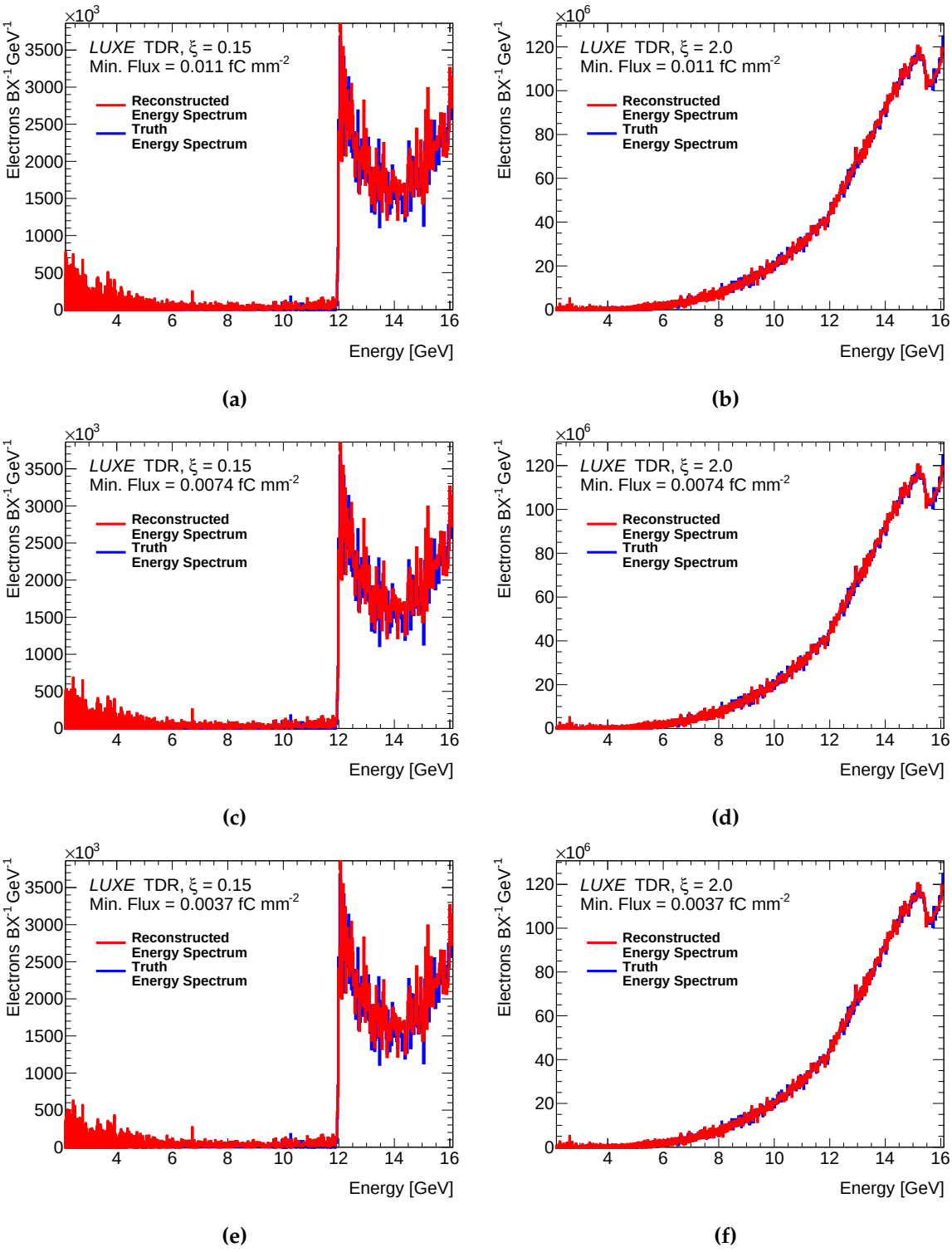

Figure 7.9.: Reconstructions from the scintillator screen and camera simulation of electron spectra from PTARMIGAN interactions of $\xi_{max} = 0.15, 2.0$ on the left and right respectively. The top, center, and bottom rows show the reconstructions with noise emulation normalised to the upper, central, and lower minimum detectable flux estimates (respectively) calculated from the 28m test-beam.

Chapter 8.

Conclusions

With the growing costs of expanding the energy frontier, particle physics must make more creative and perhaps subtle measurements to have insights into the fundamental theories describing the universe around us. The LUXE experiment allows just such an insight. This thesis showed the work undertaken chiefly to prepare a key detector for the upcoming experiment, and in Chapter 4 analysis was presented of an experiment designed to guarantee a satisfactory photon beam for the γ-laser mode of LUXE.

The high-energy Bremsstrahlung experiment presented in Chapter 4 proved to be more difficult than anticipated. The high precision of the MIMOSA detector planes leads one to believe a very precise, useful result could be returned when reconstructing the polar angle of the Bremsstrahlung photon. In reality the difficulties associated with the setup, elucidated in the chapter, gave a highly distorted result compared to the expected true Bremsstrahlung polar angle distribution. With extensive use of comparison to an involved Monte Carlo simulation of the entire setup, an estimate of the underlying beam divergence was made but the accuracy of the resulting flux projection was only of the same order magnitude as the QED-calculated beam. This was a reduction in the flux of 63%. This photon flux will be used in the γ-laser mode to generate a yield of positrons per bunch-crossing for detection in LUXE. Due to the steep gradient of the relationship between the Breit-Wheeler interaction rate and the ξ parameter, for a fixed lower bound in the detectable rate of 10^{-3} positrons per bunch-crossing, the resulting detectable ξ lower bound only increased by 12.8% and 10.8% for phase-0 and phase-I respectively. Ultimately this is comparable to the ξ uncertainty expected in the final experiment from laser diagnostics ($\pm 2.5\%$).

The development of the scintillator screen and camera detector system for its use in LUXE, the work of which was here presented over the previous three chapters, has

formed crucial work for the experiment. At the start of this project, the system did not exist, and detection of the electrons were envisaged to be handled entirely by the Cherenkov detector. The chapters 5, 6 and 7 present a thorough design, simulation and analysis campaign which successfully proved the utility of the detector, in particular showing a superior position resolution (and therefore energy resolution) to the Cherenkov detector. It was shown that this detector and its reconstruction give an accuracy in energy below the 2% level required (when in combination with an estimate for the magnetic field uncertainty). It was also proven that, with the aid of the finite-impulse-response filter technique, this could be done on a single-bunch-crossing basis. Fits of the reconstructed energy spectra with a full differential function allowed reconstruction of the ξ value for low ξ better than simple edge analysis could provide. A prototype of the system was assembled and successfully tested in test-beam, where an estimate for the calibration of on-screen charge and digital signal was gathered. This was implemented into the simulation and reconstruction environment to prove the system's suitability for the e-laser EDS case of LUXE.

This work presents a relatively complete account of the scintillator screen and camera system appropriate for this point in LUXE's development. Although the system's design is finalised, it can change should new information come to light, often the case when construction takes place. Before the final construction, proving its long-term resistance to the radiation environment, measuring a light-charge calibration curve, and integration into the wider experiment data acquisition system, remain the only obstacles in the way of its readiness for the progressing LUXE experiment.

Appendix A.

Networks & Interfaces of the Scintillation Screen & Camera Detector System

A.1. Network

Each of the described cameras uses ethernet to transmit data, and are powered through that same data ethernet connection (Power over Ethernet, or PoE). Similar cameras with alternate interfaces exist, offering in the case of USB or CameraLink a greater maximum bandwidth. Ethernet is chosen as the interface for data transmission given its universality, cost-effectiveness and crucially the possible length of the cable – up to $\sim 100\,\mathrm{m}$ – while USB and CameraLink are known to exhibit problems at lengths greater than 10 m. The ultimate cable length for each camera-to-DAQ-PC link will for both sites exceed 10 m. This is shown in Table A.1.

Table A.1.: Distance separating the service room to the relevant experimental areas.

Experimental region	Length
Bremsstrahlung target [m]	22
Interaction Point [m]	10

To assist in monitoring, the data acquisition and data handling programs will send a small number of histograms to the central LUXE DOOCS [102] slow-control, wherein the software parameters of the cameras will be alterable. These histograms are, per

camera, one sum of the pixels in the x dimension and one sum in the y dimension, and possibly simple live energy reconstructions.

A.2. Data Streaming and Storage

The images themselves are 12-bit in bit-depth, and as noted this actually limits the transmission of the 4K camera to smaller than the full resolution at 10 Hz. The rest of the screen is covered by the 2K cameras. The vertical range of the 2K cameras too are trimmed down to the screen plus some 5 mm buffer. This slightly reduces data bandwidth requirements.

The anticipated data streaming bandwidth requirements are estimated using this bit-depth, image size and frequency: each 2K camera then will transmit at $\sim 185\,\mathrm{Mb/s}$ or $\sim 23\,\mathrm{MB/s}$. The 4K camera in each instance transmits nearer the bandwidth of the ethernet interface, using the parameters in Table 5.5, at $\sim 83\,\mathrm{MB/s}$. This still preserves bandwidth to ensure safety in the quality of streaming. Summed together for one site, this is 128 MB/s of data-streaming capacity needed.

This offers an effective upper limit, but it remains likely the 4K image can be binned (data from two neighbouring pixels combined into one) within the y dimension. The nominal resolution of 50 µm for the 4K camera represents finer fidelity than may be necessary. Although for deeper analyses it may be well-motivated to retain this resolution, a binning function to combine 2 pixels to one in either the y dimension, or both x and y dimension, can reduce data rates of the 4K camera by a factor of two or four respectively. These options would provide a total $\sim 87.5\,\mathrm{MB/s}$ or $\sim 67\,\mathrm{MB/s}$ of data rates per site respectively.

This will be retained locally in the control room at the experimental hall location from run to run, until flushed to the file-systems at DESY and other institutes between runs. The two sites of this detector system are not expected to run concurrently and so the total required write speed remains equal to that of one site. The relatively high rate for the 4K camera motivates the need for more than a standard hard disk drive, as it exceeds typical reliable HDD write speeds alone, and so saving data to one disk per camera is ruled out. The excessive cost of solid-state drives (which feature higher write speeds) mean this technology is not planned to be used. Instead HDDs will be written to in parallel, in a RAID 1+0 array, increasing the write speed by a factor of

the number of drives used. Since this comes with the drawback of one drive failing resulting in the corruption of all the data, each of these drives are mirrored. RAID6 could prove suitable too, resistant to 2 drive failures with a more efficient use of space, but is inferior with respect to the high read-speeds (multiplied by a factor of all drives present) available with RAID1+0.

Table A.2.: Estimates for the data streaming/storage requirements of the scintillator & camera system (one site).

Quantity	no 4K binning	2-pixel 4K binning	4-pixel 4K binning
Data Streaming Rate [MB/s]	128	87.5	67
Approx. On-site Storage Rate [MB/s]	12.8	8.8	6.7
Max. Single Run Storage [TB]	2.2	1.5	1.15
Typical one-year Storage [TB]	64	44	34

The sum total cost of long-term storage becomes large over the lifetime of the experiment. Compression techniques can quickly help to mitigate the high volumes of data. In particular, the content of many images can be aggregated into a single image of higher bit-depth. Conversion from images of 12-bit depth to 32 bits offers a higher dynamic range by factor 10^6, allowing this number of images to be aggregated together. This is appropriate for the background measurements of the EDS and measurements at the IBM site, but for the signal measurement at the EDS the shot-to-shot variation is of interest, giving reason not to aggregate them entirely, and keep the individual images. For a run lasting 24 hours, this sums to $\sim$ 1.1 TB of signal images, where the non-signal measurements data requirement is small in comparison. The aggregation of the background images is performed immediately, so the minimum value of 6.6 TB per run (given the weekly access window to the EU.XFEL chamber, the maximum time of one data-taking run will be around 6 days) is the requirement for on-site storage for this detector. Regular flushing of the data off-site is possible throughout the run, so there is little to no down-time post-run.

It has been observed in tests that simple desktop PCs can process the treatment of the camera's images (one camera being processed by a single CPU thread), so there are no concerns with processing power when the final experiment runs.

It is anticipated that standard lossless compression algorithms will reduce the long-term storage requirements further by at least 50%. To run and gather data at the

target rate of 10^7 events per year, this gives 64 TB in long-term off-site storage per year, not counting backups. This is the largest data requirement of any detector at LUXE but is taken to be manageable. This reduces to 44 TB or 34 TB using the 4K camera images, binned in y or x & y respectively.

The images are used for reconstruction as described previously. Once the parameters of the magnetic action have been computed, the algorithm of reconstructing the energy spectrum from the image data is relatively fast. This is likely to be analysable to return shot-to-shot spectra at a rate of 1 Hz, or at least 0.1 Hz, suitable for live monitoring. The lossless algorithmic compression of the raw data is not likely to take excessive processing time. As comparison, compression of raw image data from the detector prototype into a zip file is processed at 11 MB/s with a single desktop PC thread. This compression can then be performed essentially at pace with the 1 Hz signal images. Table A.2 shows a summary of the data streaming/storage estimates.

A.3. Triggering

Trigger comes from one of the TLUs used in LUXE [103]. Each trigger comes from the accelerator clock – so images are triggered with every bunch. Trigger generated from the laser at the same time for beam-laser events, delivered to the DAQ PC, can be used to then validate those images which have recorded a laser interaction, and categorised correctly, separating signal events from beam-only events.

A.4. Cabling

The installation of cabling requires one gigabit ethernet (cat6 and above) and one coaxial cable connection between the service room and each camera. Keeping the cables out of the beam-plane helps to protect the cables from electromagnetic interference, and they are shielded in addition. The cables must also be halogen-free in any plastic coating for safety. These requirements are modest, and available commercially at low cost.

In the EDS region the ceiling mount allows the cables to be routed through the supporting tube, and thereafter attached to the ceiling before entering the service room.

Appendix B.

Installation, Calibration and Decommissioning of the Scintillation Screen & Camera Detector System

B.1. Installation

The installation and commissioning should be comparatively straightforward, although there is complication in securely fastening the ceiling mount planned for the EDS region. The main challenge is the physical alignment of 4 total components on two platforms at both sites. The envisioned setup requires both accurate alignment of the screen with respect to the beamline and B-field, and equally the cameras and their field of view to the screen(s).

Limited access to the experimental hall at installation means the shortest time possible may be required. The following estimate assumes as much preparation as reasonably possible is performed beforehand, including practice installations aboveground. Work on the two sites is possible in parallel, shortening the total time, or since the e-laser mode is envisioned to run first, the IBM site can be postponed until a later access window.

Item-by-Item Installation Plan:

1. Installation of ceiling mount infrastructure – 3 days – technicians/engineers required

2. Placement/alignment of IBM region components including cabling – 3 days – technicians/engineers required
3. Placement/alignment of EDS region components including cabling – 5 days – technicians/engineers required
4. DAQ stress tests of data streaming, triggering and running temperature (in conjunction with other detectors) – 3 days
5. Final calibration of imaging parameters due to light levels – 3 days

This gives an estimate of 8 days of access required to the experimental hall, for items 1 and 3, and item 2 performed in parallel (or at a later date), and then roughly 6 days of testing and commissioning for the last two items. The majority of this testing and commissioning comes previous to the installation.

An anticipated possible shutdown within the winter of 2024, lasting between 4 and 6 weeks, would prove adequate time to install, align and commission this detector in each location. This is only true under the assumption that the last two items can be controlled remotely, which is in principle true, but leaves open the risk of incomplete commissioning if a mistake is made within the installation window.

The possible installation within the summer of 2025 of only 2 weeks is in principle possible. In order to ensure the installation is completed with a large contingency, the choice of effectively removing one of the alignment procedures from each site could be employed. This possibility requires a redesign where the position of the cameras are rigidly connected to the screen within the same, large aluminium frame. This would remove the ceiling mount for the EDS, and remove one half of the positional alignment, at the cost of increased material budget within the beam-plane in the region.

B.2. Calibration Strategy

Calibration and tests of the scintillation response of the screens and detection characteristics of the cameras and associated optical components can be completed outside the experimental hall. The main challenge when calibrating within the experimental hall comes from alignment – the position of both the screen and camera components must be independently accurately aligned and securely fixed.

The physical alignment of the screen can be tested for a short time using any beam-time from the EU.XFEL below 16.5 GeV, for example 11.5 GeV, using a magnetic field tuned for 16.5 GeV. The beam will then directly impinge the screen, and its location/reconstructed energy can be compared to the well-known beam parameters. At this point the entire well-known bunch-charge is incident on the screen too, and so the combined detector's response per pC charge checked. This will form a useful check for the evolution of the detection efficiency over time, and can even be scanned through various values for the x position on the screen by varying the magnetic field strength, although only for some portion (less than one fifth) of the screen's full span.

The light-charge calibration curve will be measured with the geometry as close to that of the final experiment as possible at a high-flux test-beam. A standardised well-known source of light - a calibration lamp - will be used to further calibrate and test the quality of the optical line. An example product can be seen in Ref. [104]. With an optical pattern of regular line spacings the modulation transfer function independent of the resolution of the screen and its scintillation function can be ascertained. This can be done with or without the calibration lamp to help illuminate. Only one instance of each of these are required between the two sites. The lamp must output light within the wavelength range accepted by the optical filter ($\sim$545 nm).

B.3. Decommissioning

The components of this system are not heavy, toxic or dangerous. The cameras will have to be safely removed from the ceiling with DESY technical help, at which point they can be returned to the institution which owns them, if this is not DESY. The screens will directly be irradiated, and the accumulated dose for any single screen will dictate if it too is returned to the owning institute or disposed of via DESY Radiation Protection [105].

Appendix C.

ORAMS: Operability, Reliability, Availability, Maintainability, Safety of the Scintillation Screen & Camera Detector System

- Operability – The system is proven to be operable and not prohibitively difficult to operate. It is highly automatable, requiring only typical monitoring. The scintillating detector element is fully passive and the cameras standard, proven commercial equipment. The system requires a consistent, reliable, strong magnetic field to operate, but once set this field strength is unchanged during a run.
- Reliability – Similar systems have proven to be reliable within similar experiments [106], but there is always a small chance of radiation or mechanical damage. For the case of radiation damage replacements are possible. Small disruptions in position, alignment or scintillation efficiency are detectable using outside correlation with other detectors. It has been noted that scientific cameras can develop 'hot pixels', that is greater electronic noise within a single pixel, as a result of stochastic stray particles in high-radiation environment [85]. These hot pixels can be permanent, but consistent, and therefore mitigated when subtracting noise. Too many of these, particularly in the central signal bands, would motivate an exchange of cameras. The probability they will need to be replaced, or the frequency they are, is being investigated.

- Availability – Every piece of equipment is available commercially within a period of several months, or is custom-made at DESY from standard materials, in particular aluminium for the supports.
- Maintainability – Each sensitive component is comparatively inexpensive and easily replaceable. Replacements for the mechanical supports will also be constructed, in the unlikely case of mechanical damage to these supports. Damage to these may require a full re-alignment, however, requiring up to several days to do so. Replacement cameras can be attached to the same lens, fixed in place and correctly set for aperture and focus, meaning an exchange is quick and easily performed within a one-day access period, which is typically available once per week [47]. The design of the screen support will also allow for easy exchange of the screens, which are manufactured to be similar as possible, and again this swap can be performed within one day.
- Safety – Over some long integrated time the scintillation screens, like all components in the area, may absorb enough dose to be regarded as activated. To better make an estimate of this requires detailed radiation maps. If the components become activated, like the rest of the experiment, they would then require handling and disposal at the end of the experiment or the end of use of the specific screen, along guidance and consultation with the DESY D3 Radiation Protection group [105]. There are no hazardous materials or high-voltage equipment.

Appendix D.

Scintillator Detector Simulation Compton Edge Reconstruction Values

Tables D.1 and D.2 show the reconstructed ξ values using the simulation and reconstruction method described in Chapter 6, where the meanings of these values are explained. Table D.1 shows these reconstructions for discrete simulations using the LUXE phase-0, and D.2 of phase-I.

Table D.1.: Retrieved ξ_{fit}, ξ_{max}, ξ_{mode} parameters from the best-fit functions and edge analysis, applied to reconstructed spectra from Monte Carlo simulations of a particular ξ_{max}.

ξ_{max} Monte Carlo	ξ_{fit} full-function-fit	ξ_{max} finite-impulse	ξ_{mode} finite-impulse
0.15	0.1522	0.2045	0.1519
0.2	0.2894	0.2394	0.195
0.3	0.2776	0.3266	0.2925
0.5	0.4675	0.5139	0.4864
0.7	0.5867	0.7105	0.6716
1.0	0.8447	0.9944	0.8945
1.2	1.0596	1.179	1.0899
1.5	1.3376	1.458	2.6277
2.0	1.8947	1.9141	0.552
3.0	2.4581	2.8604	0.7616
4.0	3.319	3.3734	1.519

Table D.2.: Retrieved ξ_{fit}, ξ_{max}, ξ_{mode} parameters from the best-fit functions and edge analysis, applied to reconstructed spectra from Monte Carlo simulations of a particular ξ_{max} with the phase-I laser.

ξ_{max} Monte Carlo	ξ_{fit} full-function-fit	ξ_{max} finite-impulse	ξ_{mode} finite-impulse
0.15	0.1248	0.2045	0.1256
0.2	0.1854	0.2394	0.195
0.3	0.2768	0.3649	0.2925
0.5	0.468	0.5139	0.4974
0.7	0.5829	0.7217	0.6937
1.0	0.8946	1.0085	0.9875
1.2	1.1214	1.2138	1.1705
1.5	1.4236	1.5064	1.4698
2.0	1.6272	1.9978	1.8943
3.0	2.5481	2.9691	2.6277
4.0	2.2778	3.7404	3.2959

Colophon

This thesis was made in LaTeX 2_ε using the "hepthesis" class [107]. The mathematical expressions use the Euler-VM font [108]. Feynman diagrams have been generated using the TikZ-Feynman package [109].

Bibliography

[1] H. Abramowicz *et al.*, Eur. Phys. J. Spec. Top. **230**, 24452560 (2021).

[2] B. Abi *et al.*, Phys. Rev. Lett. **126**, 141801 (2021).

[3] D. Hanneke, S. Fogwell Hoogerheide, and G. Gabrielse, Phys. Rev. A **83**, 052122 (2011).

[4] R. Bouchendira, P. Cladé , S. Guellati-Khélifa, F. Nez, and F. Biraben, Phys. Rev. Lett. **106**, 080801 (2011).

[5] M. E. Peskin and D. V. Schroeder, *An Introduction to Quantum Field Theory* (Addison-Wesley, Reading, USA, 1995).

[6] R. P. Feynman, *QED: The Strange Theory of Light and Matter* (Princeton University Press, 2006).

[7] F. Jegerlehner *et al.*, Phys. Lett. B **767**, 485 (2017).

[8] F. Sauter, Z. Phys. **69**, 742 (1931).

[9] D. Seipt, *Strong-Field QED Processes in Short Laser Pulses*, PhD thesis, Tech. U. Dresden, ITP, 2012.

[10] M. Born, Z. Phys. **38**, 803 (1926).

[11] D. M. Wolkow, Z. Phys. **94**, 250 (1935).

[12] F. Karbstein, H. Gies, M. Reuter, and M. Zepf, Phys. Rev. D **92**, 071301 (2015).

[13] M. Bell and J. S. Bell, Part. Accel. **24**, 1 (1988).

[14] S. Meuren, *Exploring Strong Field QED with ILC Beams*, `https://indico.cern.ch/event/995633/contributions/4273729/attachments/2209037/3738211/SFQED_AT_THE_ILC.pdf`, 2021, Presented at International Workshop on Future Linear Colliders.

[15] K. Hurley *et al.*, Nature **434**, 1098 (2005).

[16] P. Zhang, S. S. Bulanov, D. Seipt, A. V. Arefiev, and A. G. R. Thomas, Physics of Plasmas **27**, 050601 (2020), https://pubs.aip.org/aip/pop/article-pdf/doi/10.1063/1.5144449/15874129/050601_1_online.pdf.

[17] I. Pomeranchuk and Y. Smorodinsky, J. Phys. USSR **9**, 97 (1945).

[18] T. Heinzl and A. Ilderton, *Corrections to Laser Electron Thomson Scattering*, 2013, arXiv:1307.0406.

[19] T. Koffas, *Positron Production in Multiphoton Light by Light Scattering*, PhD thesis, Rochester U., 1998.

[20] C. Harvey, T. Heinzl, and A. Ilderton, Phys. Rev. A **79**, 063407 (2009), arXiv:0903.4151.

[21] J. Schwinger, Phys. Rev. **82**, 664 (1951).

[22] V. I. Ritus, J. Sov. Laser Res. **6**, 497 (1985).

[23] N. B. Narozhny, Phys. Rev. D **21**, 1176 (1980).

[24] J. Adam *et al.*, Phys. Rev. Lett. **127**, 052302 (2021).

[25] G. Aad *et al.*, Phys. Rev. Lett. **123**, 052001 (2019).

[26] L. Schoeffel *et al.*, Prog. Part. Nucl. Phys. **120**, 103889 (2021).

[27] C. Bamber *et al.*, Phys. Rev. D **60**, 092004 (1999).

[28] S. Meuren, *Probing Strong-field QED at FACET-II (SLAC E-320)*, `https://conf.slac.stanford.edu/facet-2-2019/sites/facet-2-2019.conf.slac.stanford.edu/files/basic-page-docs/sfqed_2019.pdf`, 2019, Presented at FACET-II Science Workshop 2019.

[29] S. Meuren, *E-320 FY22 Progress and Plans for FY23*, `https://facet-ii.slac.stanford.edu/sites/default/files/E320_smeuren_2022_PAC_0.pdf`, 2022, Presented at FACET-II Program Advisory Committee Meeting 2022.

[30] J. M. Cole *et al.*, Phys. Rev. X **8**, 011020 (2018).

[31] K. Poder *et al.*, Phys. Rev. X **8**, 031004 (2018).

[32] T. N. Wistisen, A. D. Piazza, H. V. Knudsen, and U. I. Uggerhøj, Nature Commu-

nications **9** (2018).

[33] C. F. Nielsen *et al.*, Differential measurement of trident production in strong electromagnetic fields, 2023, 2307.03464.

[34] G. Grittani, *Photon Physics at ELI-Beamlines User Facility*, `https://indico.cern.ch/event/1139676/contributions/5049430/attachments/2513267/4375898/Grittani_Photon_Physics_At_ELI_Beamlines_User_Facility.pdf`, 2022, Presented at New Vistas in Photon Physics in Heavy-Ion Collisions EMMI Workshop.

[35] S. Meuren *et al.*, *On Seminal HEDP Research Opportunities Enabled by Colocating Multi-Petawatt Laser with High-Density Electron Beams*, 2020, arXiv:2002.10051.

[36] R. Abela *et al.*, *XFEL: The European X-Ray Free-Electron Laser - Technical Design Report* (DESY, Hamburg, 2006).

[37] European X-Ray Free-Electron Laser, *XFEL Operation*, `https://www.xfel.eu/facility/operation/index_eng.html`, Accessed 2022.

[38] D. Strickland and G. Mourou, Optics Comm. **55**, 447 (1985).

[39] A. Sävert and M. Zepf, *JETI40 Laser*, `https://www.hi-jena.de/en/helmholtz_institute_jena/about-the-institute/experimental-facilities/local/jeti40-laser`, Accessed 2023.

[40] L. Helary, S. Boogert, and R. Jacobs, *LUXE Technical Note: Technical Coordination*, 2022 (unpublished).

[41] G. Pariente *et al.*, Nature Photon. **10**, 547 (2016).

[42] M. Mager, Nucl. Instrum. Meth. A **824**, 434 (2016).

[43] P. Billoir and S. Qian, Nucl. Instrum. Meth. A **294**, 219 (1990).

[44] H. Abramowicz *et al.*, Eur. Phys. J. C **79**, 579 (2019), 1812.11426.

[45] K. Fleck, N. Cavanagh, and G. Sarri, Sci. Rep. **10**, 9894 (2020).

[46] Z. Bai *et al.*, Phys. Rev. D **106**, 115034 (2022).

[47] LUXE Collaboration, *LUXE Technical Note: Executive Summary and Physics Prospects*, 2022 (unpublished).

[48] T. G. Blackburn, *Ptarmigan Github*, `https://github.com/tgblackburn/ptarmigan`.

[49] Particle Data Group, Prog. Theor. Exp. Phys. **2022**, 083C01 (2022).

[50] H. Messel and D. Crawford, *Electron-Photon Shower Distribution Function Tables for Lead, Copper, and Air Absorbers*, 1970.

[51] The Geant4 Collaboration, *Geant4 Reference Physics Lists*, `https://geant4-userdoc.web.cern.ch/UsersGuides/PhysicsReferenceManual/fo/PhysicsReferenceManual.pdf`, 2022.

[52] Y.-S. Tsai, Rev. Mod. Phys. **46**, 815 (1974).

[53] Y.-S. Tsai, Rev. Mod. Phys. **49**, 421 (1977).

[54] P. L. Anthony *et al.*, Phys. Rev. D **56**, 1373 (1997).

[55] H. D. Hansen *et al.*, Phys. Rev. D **69**, 32001 (2004).

[56] A. Schälicke, V. Ivanchenko, M. Maire, and L. Urban, *Improved description of Bremsstrahlung for high-energy electrons in Geant4*, in *2008 IEEE Nuclear Science Symposium and Medical Imaging Conference and 16th International Workshop on Room-Temperature Semiconductor X-Ray and Gamma-Ray Detectors*, pp. 2788–2791, 2008.

[57] R. Diener *et al.*, Nucl. Instrum. Meth. A **922**, 265 (2019).

[58] DESY, *Generation of the DESY Test Beams*, `https://particle-physics.desy.de/test_beams_at_desy/beam_generation/index_ger.html`, Accessed 2023.

[59] A. Himmi *et al.*, *MIMOSA26 User Manual*, 2011.

[60] P. Ahlburg *et al.*, J. Instrum. **15**, P01038 (2020).

[61] T. Bisanz *et al.*, J. Instrum. **15**, P09020 (2020).

[62] *EUTelescope Github*, `https://github.com/eutelescope/eutelescope`, 2022.

[63] J. Baudot *et al.*, *First Test Results of MIMOSA-26, a Fast CMOS Sensor with Integrated Zero Suppression and Digitized Output*, in *2009 IEEE Nuclear Science Symposium Conference Record (NSS/MIC)*, pp. 1169–1173, 2009.

[64] H. Jansen *et al.*, EPJ Techn. Instrum. **3**, 7 (2016).

[65] DESY, *DESY II Description & Status*, https://particle-physics.desy.de/test_beams_at_desy/desy_ii_description__status/index_ger.html, 2022.

[66] S. Spannagel *et al.*, Nucl. Instrum. Meth. A **901**, 164 (2018).

[67] H. Abramowicz *et al.*, Eur. Phys. J. C **79** (2019).

[68] K. Fleck, N. Cavanagh, M. Streeter, and G. Sarri, *LUXE Technical note: Gamma Spectrometer*, 2022 (unpublished).

[69] M. Berggren, S. Caiazza, M. Chera, and J. List, Nucl. Instrum. Meth. A ***1010***, 165555 (2021).

[70] R. Jacobs, L. Helary, S. Schmitt, and B. Heinemann, *LUXE Technical Note: Cherenkov Detector*, 2022 (unpublished).

[71] Basler AG, *Basler Area Scan Camera Range*, https://www.baslerweb.com/en/products/cameras/area-scan-cameras/, Accessed 2021.

[72] Edmund Optics, *543nm CWL 50mm Diameter 22nm Bandwidth OD 6 Fluorescence Filter*, Accessed 2021.

[73] Basler AG, *Basler acA4096-11gm Camera Specification - Document Number: BD001167, v.01*, Accessed 2021.

[74] Basler AG, *Basler acA1920-40gm Camera Specification - Document Number: BD000940, v.01*, Accessed 2021.

[75] MCIO Optonix, *DRZ Screens*, http://www.mcio.com/Products/drz-screens.aspx, Accessed 2021.

[76] I. D. Jung *et al.*, J. Micromech. Microeng. **19**, 015014 (2009).

[77] Mitsubishi Chemical, www.m-chemical.co.jp/en/products/departments/mcc/ledmat/product/1201037_7550.html, Accessed 2021.

[78] R. Morlotti, M. Nikl, M. Piazza, and C. Boragno, J. Lumin. **72-74**, 772 (1997).

[79] J. Bauche *et al.*, Nucl. Instrum. Meth. A **940**, 103 (2019).

[80] El-Mul Technologies Ltd., *ScintiMax Data Sheet*, Accessed 2021.

[81] J.-P. Schwinkendorf *et al.*, J. Instrum. **14**, P09025 (2019).

[82] Basler AG, *Basler Product Documentation - acA1920-40gm*, https://docs.

baslerweb.com/aca1920-40gm, Accessed 2021.

[83] Basler AG, *Basler Product Documentation - acA4096-11gm*, https://docs.baslerweb.com/aca4096-11gm, Accessed 2021.

[84] Basler AG, *I/O Timing Characteristics*, https://docs.baslerweb.com/io-timing-characteristics, Accessed 2021.

[85] A. Huber *et al.*, Fusion Eng. Des. **123**, 669 (2017), Proceedings of the 29th Symposium on Fusion Technology (SOFT-29) Prague, Czech Republic, 2016.

[86] P. Rebut, R. Bickerton, and B. Keen, Nucl. Fusion **25**, 1011 (1985).

[87] A. Vasilescu and G. Lindstroem, *Displacement Damage in Silicon, On-line Compilation*, https://rd50.web.cern.ch/NIEL/, Accessed 2023.

[88] G. Battistoni *et al.*, Ann. Nucl. Energy **82**, 10 (2015), Joint International Conference on Supercomputing in Nuclear Applications and Monte Carlo 2013, SNA + MC 2013. Pluri- and Trans-disciplinarity, Towards New Modeling and Numerical Simulation Paradigms.

[89] C. Ahdida *et al.*, Front. Phys. **9** (2022).

[90] Edmund Optics, *Edmund 75mm DG Series Fixed Focal Length Lens*, https://www.edmundoptics.co.uk/p/75mm-dg-series-fixed-focal-length-lens/11371/, Accessed 2021.

[91] Basler AG, *Basler Lens C11-5020-12M-P f50mm - Lens*, https://docs.baslerweb.com/c11-5020-12m-p, Accessed 2021.

[92] Edmund Optics, *0.6 OD 50mm Diameter Reflective ND Filter*, https://www.edmundoptics.eu/p/06-od-50mm-dia-uv-nir-nd-filter/46588/, Accessed 2023.

[93] D. Kim, *R-Weg: A New High-Intensity Electron Beamline at DESY II*, https://indico.cern.ch/event/1058977/contributions/4865303/, 2022, Presented at Beam Telescopes and Test-Beams (BTTB) 10.

[94] K. Sjøbæk *et al.*, *Status of the CLEAR Electron Beam User Facility at CERN*, Proceedings from the 10th International Particle Accelerator Conference (IPAC2019), JACoW, 2019.

[95] M. Wing *et al.*, *The AWAKE Electron Spectrometer*, Proceedings from the 9th

International Particle Accelerator Conference (IPAC2018), JACoW, 2018.

[96] DESY, *ARES Accelerator Reaches Design Energy*, https://www.desy.de/news/news_search/index_eng.html?openDirectAnchor=1953, 2023.

[97] F. Keeble, *Measurement of the Electron Energy Distribution at AWAKE*, PhD thesis, University College London, 2019.

[98] S. Bohlen *et al.*, Phys. Rev. Accel. Beams **25**, 031301 (2022).

[99] M. Borysova and O. Borysov, *LUXE Technical note: Backscatter Calorimeter*, 2021 (unpublished).

[100] D. Lipka *et al.*, *Dark Current Monitor for the European XFEL.*, 10th European Workshop on Beam Diagnostics and Instrumentation for Particle Accelerators, JACoW, 2011.

[101] Edmund Optics, *Green M34.0 x 0.50 High Performance Machine Vision Filter*, https://www.edmundoptics.com/p/green-m340-x-050-machine-vision-filter/32224/, Accessed 2021.

[102] DESY, *The Distributed Object-Oriented Control System Framework*, https://doocs-web.desy.de/index.html, 2022.

[103] H. Abramowicz *et al.*, *LUXE Technical Note: Common Aspects*, 2021 (unpublished).

[104] Advanced Illumination / Edmund Optics, *100 x 100mm 520nm LED Backlight*, https://www.edmundoptics.de/p/100-x-100mm-520nm-led-backlight/21339/, Accessed 2022.

[105] DESY Radiation Protection Group, https://d3.desy.de/index_eng.html, Accessed 2020.

[106] E. Adli *et al.*, Nature **561**, 363367 (2018).

[107] A. Buckley, *The hepthesis LaTeX class*.

[108] Walter Schmidt, *The Euler Virtual Math Fonts for use with LaTeX*, https://mirror.mwt.me/ctan/fonts/eulervm/doc/latex/eulervm/eulervm.pdf, 2005.

[109] J. P. Ellis, Comput. Phys. Comm. **210**, 103 (2017).